FIELD CHARACTERISTICS OF A MULTIELEMENT ULTRASONIC TRANSDUCER APPLICATOR FOR HYPERTHERMIA THERAPY

BY

HAROLD ROGER UNDERWOOD

B.S., University of Illinois, 1984
B.A., Wheaton College, 1984

THESIS

Submitted in partial fulfillment of the requirements
for the degree of Master of Science in Electrical Engineering
in the Graduate College of the
University of Illinois at Urbana-Champaign, 1986

Urbana, Illinois

ACKNOWLEDGEMENTS

I am deeply grateful to the many people who helped make this project a success. First, I give credit to Clif Burdette, whose theoretical insights and ideas provided direction for this work. Steve Goss provided practical insight on the acoustics and helped prepare the experimental apparatus. Steve Foster offered valuable assistance on the electronic hardware. I am thankful for Richard Magin, who kept track of my progress, protected my academic interests and sanity, and secured my financial support. I also thank Clif and Richard for their advice in the preparation and wording of the thesis. Thanks to Wanda Elliott, who spent many hours tediously typing the text.

I also want to thank the following graduate research assistants and Bioacoustics Research Laboratory personnel for their assistance: Paul Benkeser, Tim Benson, Bob Cargoni, Aaron Field, Panos Hadjimitsos, Ken Ocheltree, Dave Padgitt, Joe Cobb, and Billy McNeill; also Paul Neubauer, Scott Walter, and any others I have forgotten to mention.

Finally, I would like to give special thanks to some friends who supplied inspirational support: Tim Davis, Loren Fishback, Dave German, Dave Jones, Todd Okamoto, Ken Saiki, and Becky Janis, who helped me keep a positive attidude. I thank my whole family for their understanding, encouragement, and love.

TABLE OF CONTENTS

CHAPTER		PAGE
1	INTRODUCTION.	1
2	AN ULTRASONIC HYPERTHERMIA THERAPY SYSTEM	6
3	MATHEMATICAL MODELING AND COMPUTER SIMULATION OF THE NEAR FIELD PRODUCED BY AN ARRAY OF TRANSDUCERS	12
4	EXPERIMENTAL APPARATUS AND TECHNIQUES	22
5	EXPERIMENTAL RESULTS OF SCANNING THE ACOUSTIC FIELDS FROM TWO MULTIELEMENT SQUARE ARRAY APPLICATORS	37
6	DISCUSSION AND INTERPRETATION OF RESULTS.	45
7	CONCLUSIONS AND SUGGESTIONS FOR FURTHER STUDY . .	57
APPENDIX A--SIMULATED RESULTS.		60
APPENDIX B--EXPERIMENTAL RESULTS		100
APPENDIX C--SIMULATIONS WITH AN IMPROVED MODEL		131
APPENDIX D--COMPUTER PROGRAMS.		144
REFERENCES		152

CHAPTER 1

INTRODUCTION

1.1. Hyperthermia Therapy

For centuries man has associated elevated body temperatures with the healing process. Even today, however, the exact connection between fever temperatures greater than 40°C and their healing effects remains largely unclear. An established fact is that high fevers (in the whole body) allowed to reach excessive temperatures can have dangerous consequences, including convulsions, permanent brain damage, and even death. On the other hand, as early as the last century, investigation began on the positive effects of controlled hyperthermia below these danger levels. Medical practitioners found improved results in treatment of cancer tumors by hyperthermia therapy [Hahn, 1984].

Several physiological conditions contribute to the effectiveness of hyperthermia as a means of preferential killing of malignant cells. Cancer cells become heat sensitive due to nutritional deprivation, low pH and chronic hypoxia. Tissue conditions and blood flow in the physical environment of solid tumors affect uniformity of heating [Song et al., 1984]. Variable blood flow, differential energy absorption, and reflection of various tissue structures can produce nonuniform heating patterns which may have adverse results on the hyperthermia therapy in that region. But within the right tissue environment, hyperthermia by itself can effectively kill malignant cells.

Although hyperthermia is effective at preferential cancerous cell killing, it also increases the effectiveness of other cancer therapy modalities. Great potential lies in the use of hyperthermia in conjunction with chemotherapy and radiation therapy [Hahn, 1982]. Heat increases the cell killing ability of many drugs. A clearly demonstrated synergism also exists between heat and X-rays. Exposure to elevated temperatures before or after radiation increases the cytotoxicity of X-rays [Overgaard, 1976], reducing the effective dose requirement and improving the cure rate. Though hypoxic cells present in malignant tumors are highly resistant to X-radiation, heat kills these cells at least as well as normally oxygenated ones. Therefore, optimum benefits of hyperthermia therapy are realized when adverse effects to malignant tissue are maximized while normal tissue remains unharmed. This happens when heating occurs preferentially at the tumor site.

1.2. Localized Hyperthermia Techniques

Engineers meet the challenge of selective tumor heating by designing systems to produce localized hyperthermia. Several techniques exist today. Some researchers experiment with magnetic induction [Oleson, 1984] and ferromagnetic implants [Stauffer et al., 1984]. More widely used techniques employ microwave (electromagnetic) energy to accomplish direct tissue heating. For this method, ridged waveguide applicators [Paglione et al., 1981], interstitial antenna arrays [Lyons et al., 1984], and phased arrays [Benson, 1985] are used.

Microwave techniques have the advantage of penetrating tumor sites in tissue where bone and air-filled cavities are present, such as lung tissue. However, microwaves have a shallow penetration depth and are largely limited to treatment of superficial tumors. For example, at 2450 MHz, the penetration depth is only 1.7 cm. Lower frequencies penetrate deeper in the lossy tissue but aperture dimensions of the applicator become small compared to a wavelength creating a divergent energy beam.

Ultrasonic (acoustic) energy represents an appealing alternative to microwave energy for inducing hyperthermia at specific treatment sites in the body. Although reflection of ultrasound from tissue interfaces such as bone and air-filled cavities rules out certain treatment regions more easily handled by microwaves (for example up to 30% of the incident acoustic energy is reflected at a muscle-bone interface), at treatment sites in relatively homogeneous tissue, ultrasound has a deeper penetration depth than microwaves. With a 1 MHz operating frequency, ultrasound penetrates up to 7 cm deep compared to a typical penetration of 2 - 3 cm for 915 MHz microwaves. Thus, ultrasound can reach more deeply seated tumors at certain sites. Other advantages of ultrasound techniques include lower frequency electronics and amplifiers. These are lower cost than their microwave counter parts. While mircowave systems require optical or other EM transparent probes, ultrasonic heating can be monitored by using properly coated thermocouple temperature probes. These probes can provide accurate temperature data if properly compensated for viscous heating artifacts. These occur at the thermocouple tip when present in the ultrasound field.

Ultrasonic hyperthermia systems must meet the need for controlled local tissue heating. Effective control requires the knowledge of what tissues are heated at what temperature and how uniformly. An ideal transducer applicator could rapidly effect changes in these parameters. Ultrasonic applicators used for this purpose range from single, unfocused transducers to multielement arrays and, ultimately, to phased and tapered arrays. Currently, the sophisticated techniques of phased and tapered arrays bring precise control within the realm of possibility. However, a multielement applicator is a relatively simple alternative which provides a high degree of control over temperature distribution in tissue, with a greater precision than a single, unfocused transducer. These techniques insure that advances in ultrasound technology will increase the role of hyperthermia in cancer therapy.

1.3. A Multielement Ultrasonic Applicator

The purpose of this thesis is to characterize the field patterns of a multielement ultrasonic square array transducer applicator for use in hyperthermia therapy. The intention is to present results which show the advantages of a multielement transducer compared to a single, unfocused one and identify features useful in hyperthermia therapy. Limitations of the multielement transducer are also revealed. The data includes theoretical field patterns generated by computer simulation as well as experimentally measured field patterns from multielement square array applicators. The development begins by dealing with characteristics of single element field patterns and then moves

to adjacent double element patterns, followed by other selected multiple element patterns. Of specific interest are the effects of amplitude and phase variations on the field patterns from adjacent double elements. Several techniques of obtaining a field pattern which produces uniform temperature distribution in tissue are identified. The results of these investigations show the value of a multielement square array applicator relative to a single unfocused applicator in hyperthermia therapy.

The remainder of this thesis is divided into six chapters. The characteristics of a computer-controlled multielement ultrasound hyperthermia system are described in Chapter 2. A mathematical model is developed and computer simulated results are presented in Chapter 3. Apparatus and techniques used to make experimental measurements are described in Chapter 4. Results of experimental measurements are represented in Chapter 5. Similarities and differences between the simulated and experimental results are discussed in Chapter 6. Interpretations are made and a hypothesis is offered to account for the discrepancies. Features desirable for hyperthermia therapy are also identified in Chapter 6. Finally, some conclusions are drawn and some suggestions for further study are made in Chapter 7.

CHAPTER 2

AN ULTRASONIC HYPERTHERMIA THERAPY SYSTEM

2.1. A Description of the SONOTHERM 1000 System

A hyperthermia system incorporating many characteristics needed for improved control of therapy has recently been developed. The SONOTHERM 1000 is designed to deliver controlled hyperthermia in the range of 42 - 45°C (108 - 113°F) above the normal body temperature 37°C (98.6°F). This system utilizes four independently programmable, computerized sub-systems. These four functionally distinct sub-systems include: (1) a multielement ultrasonic transducer applicator which directs heat-generating acoustic energy into the tumor, (2) a multichannel thermocouple thermometry system which measures the temperature throughout the tumor during treatment, (3) a generator consisting of a high voltage power supply and radio frequency amplifiers which provides electrical energy to drive the transducer applicator, and (4) a computer to coordinate and control the various processes (i.e., applicator, thermometry, and generator).

The block diagram in Fig. 2.1 shows the interrelationship of the various sub-systems. A PDP 11-23 microcomputer (Digital Equipment Corp.) controls the system. The computer displays realtime video graphics information concerning tumor size, position of thermocouple probes in normal and cancerous tissue, temperature levels, and the time course of therapy. It simultaneously communicates with the ultrasonic driver to control its operation by receiving temperature feedback information from the multichannel thermometry system which updates the system's

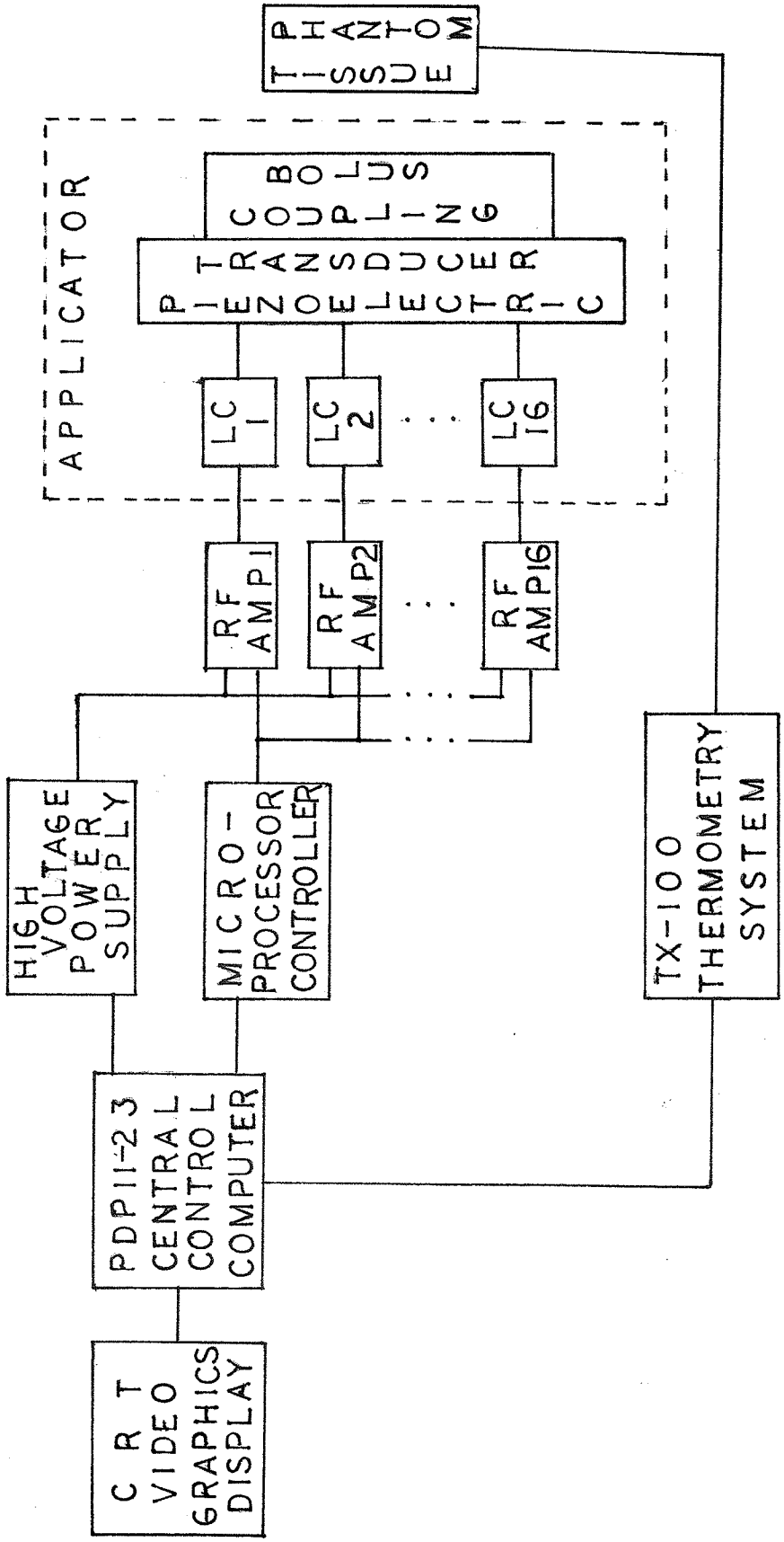

Figure 2.1. The SONOTHERM 1000 system for delivering precisely controlled ultrasound induced hyperthermia therapy.

current heating strategy. Such a "feedback loop" optimizes effectiveness of the hyperthermia therapy treatment by precisely measuring the temperature inside and outside the tumor. This information determines the frequency, intensity, and direction of power output most suitable for optimum therapeutic heating under changing tumor conditions. Computerization of these processes lessens the potential for error, thereby increasing the safety of the system and reducing the need for highly trained personnel to operate the system. However, during the therapy, a clinical technician or physician monitoring the system may interact with it as desired and intervene if problems arise.

2.2. The Open-loop Ultrasonic Transducer Applicator Sub-system

The main open-loop sub-system consists of the central computer, ultrasonic driver (Intel 8031 microprocessor and high voltage power supply), radiofrequency (RF) amplifiers, electrical matching network, piezoelectric transducer, and a water coupling bolus. This sub-system creates the ultrasonic field intensity patterns required to achieve specified temperature distributions. Power delivered per element may be adjusted two ways. The programmable power supply permits adjustment of the common high voltage supplied to the RF amplifiers. Additionally, the microprocessor controller adjusts the duty cycle (RF-ON period/RF-OFF period ratio) of each amplifier, based on commands from the control computer. These two methods provide enough versatility to suit a wide range of field intensity requirements.

Although each RF amplifier receives a common high voltage level, the duty cycle of each individual RF amplifier (and

therefore, transducer element) may be adjusted as necessary. Optional operating frequencies of 1 MHz or 3 MHz provide additional versatility for adjusting depths of treatment. The RF amplifiers maintain strict stability requirements so that the transducer elements operate at resonance with efficient power transfer. Individual LC (inductor/capacitor) matching networks provide the right load impedance for the amplifiers so that maximum power transfer occurs to the transducers.

2.3. The Multielement Square Array Transducer Applicator

Considerations that affect the choice and design of the piezoelectric transducer material and supporting structure for the square array transducer applicator include mounting, backing, surface area, efficiency, power handling capability, and thickness (related to the operating frequency). The 16-element applicator has a ground plane at the clamped edges, individually plated electrode contacts for each element and a 232 cm^2 total surface area. Air circulation through the applicator box helps to handle heat dissipation and increases power handling capability. The primary operating frequency dictates the choice of a piezoelectric material with thickness a half-wavelength for resonance. At 1 MHz this thickness is 0.203 cm (0.080 in) for Channel 5800 ceramic (PZT-8) manufactured by Channel Industries, Santa Barbara, CA.

A degassed water coupling bolus attached to the face of the transducer applicator improves acoustic power transfer from applicator to patient. Length of this coupler determines the limits of the near-field ultrasound treatment range received by

the patient. Degassed water circulates within the coupler to minimize both power loss from reflections and possible cavitation caused by small bubbles. The water also provides some cooling capacity for both the transducer crystal and the patient's skin. A thin membrane provides close patient contact and has acoustic window properties.

This thesis concentrates on characterization of the 16-element square array transducer applicator and a smaller 4-element square array with similar physical and acoustic properties. For each applicator, the square elements are numbered from left to right by rows from top to bottom (facing the external surface of the transducer). Figure 2.2 shows the dimensions and element numbering scheme for each applicator. Actual dimensions are slightly smaller due to machining considerations.

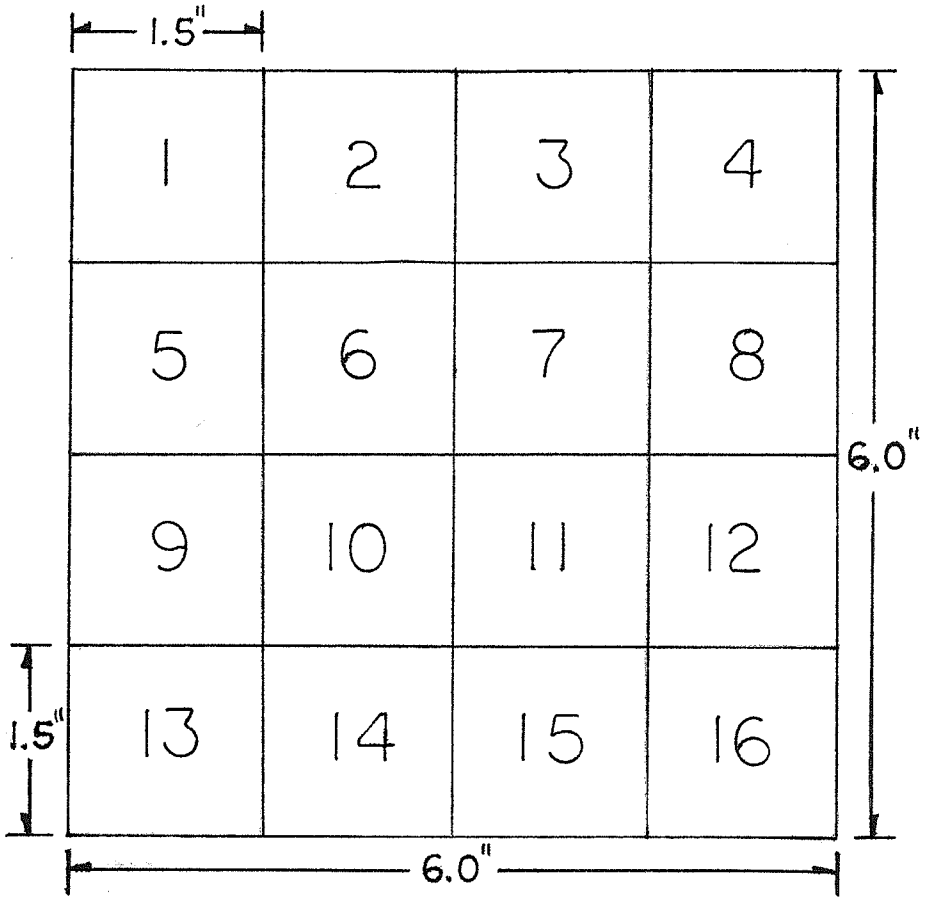

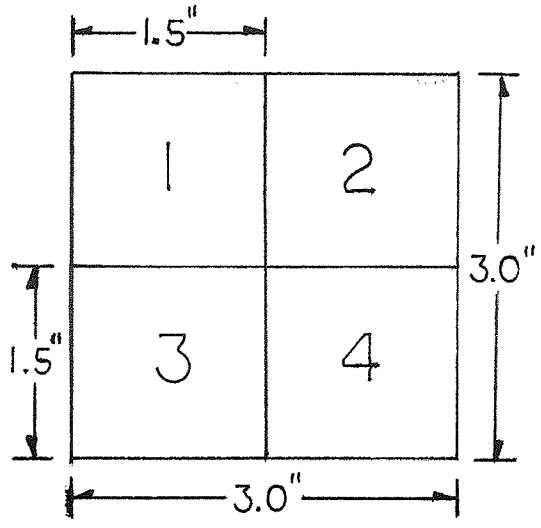

Figure 2.2. Numbering schemes on 4- and 16-element square array transducer applicators.

CHAPTER 3

MATHEMATICAL MODELING AND COMPUTER SIMULATION OF THE NEAR FIELD PRODUCED BY AN ARRAY OF TRANSDUCERS

3.1. Fundamental Acoustic Theory

Acoustic field theory establishes the mathematical foundation that can predict the behavior of pressure fields from an arbitrary acoustic source using physical parameters of the system. Such a mathematical model with appropriate simplifying assumptions and numerical approximation techniques provides a basis for computer simulation studies to complement the results of experimentally measured near fields produced by an array of acoustic transducers. Although the model used for computer simulations here to predict the field patterns from the square array only approximates the physical situation of the transducer, it does provide meaningful comparisons with the experimental results. It also becomes a convenient way of testing the effect of various controlled parameters on the expected field patterns.

Finding the pressure field from a square array source involves solving the general equation for the pressure field from an arbitrary source in an infinite rigid baffle over the appropriate limits. Equation (3.1) relates the contribution of an infinitesimal element of area ds on the source to an element of pressure dp in the field [Kinsler et al., 1982].

$$dp = \frac{j\rho ck}{2\pi r} (u \cdot ds) e^{j(\omega t - kr)} \qquad (3.1)$$

The parameter ρ represents the density of the medium, c represents the speed of sound in the medium, $k = 2\pi/\lambda$ denotes the wavenumber (inversely proportional to the wave length), r represents the distance from the source element ds to the pressure element dp in the field, u represents the complex particle velocity distribution of the surface s, and ω denotes the frequency ($\omega = 2\pi f$). To account for losses in the medium we can introduce an attenuation constant α. Equation (3.2) represents this situation by including an exponential decay factor.

$$dp = \frac{j\rho ck}{2\pi r} (u \cdot ds)\ e^{-\alpha r}\ e^{j(\omega t - kr)} \tag{3.2}$$

Figure 3.1 shows the coordinate system used for a square array transducer to calculate the pressure at a point p(x,y,z) from the contributing source element ds at (x_o,y_o) in the z = 0 plane. Integrating both sides of Eq. (3.2) yields the total pressure field

$$p = \frac{j\rho ck}{2\beta} \int_s u(x_o,y_o) \frac{e^{-(\alpha+jk)r}}{r} ds \tag{3.3}$$

where $u(x_o,y_o) = u_o(x_o,y_o)\ \exp(j\beta(x_o,y_o))$. Functions $u_o(x_o,y_o)$ and $\beta(x_o,y_o)$ are the magnitude and phase, respectively, of the particle velocity of the element ds at (x_o,y_o). The time dependence is supressed for simplicity.

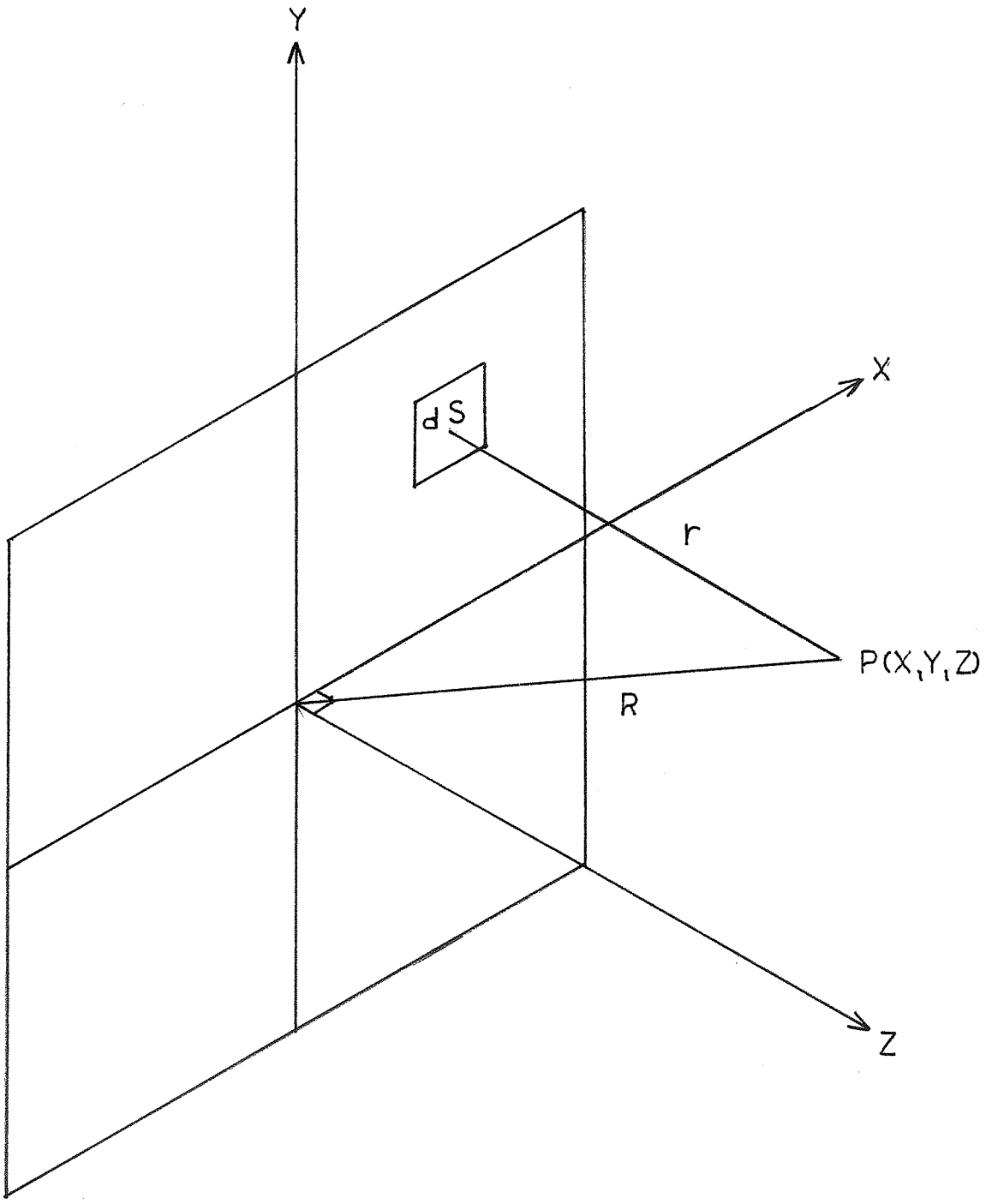

Figure 3.1. Coordinate system for computation of the pressure field from a square array.

3.2. Numerical Approximations

Several different numerical methods exist to approximate Eq. (3.3). The Fourier transform method can be applied using the Fresnel or the Fraunhofer approximation with the help of a Fast Fourier Transform (FFT) algorithm. However, errors in r for both the Fresnel and Fraunhofer approximations become unacceptably large for field points in the treatment region ($r > 20\lambda$) with large x and y displacements [Ocheltree, 1984]. The Method of Equidistant Areas considers the pressure as the summation of the pressures produced by individual elements [Freedman, 1959]. Elemental pressures are calculated by dividing the surface into incremental areas, each contributing an incremental pressure of constant phase at the field point. Best suited for source geometries with large equidistant areas, the Method of Equidistant Areas could conceivably handle the large planar transducers under study here.

More straightforward ways to calculate the field are the Point Radiation Method and the Rectangular Radiator Method [Ocheltree, 1984]. The Point Radiator Method calculates the field by representing the source with a large number of point generators. This method works well for near field calculations. It is most advantageous, however, when the field is evaluated as a function of z, and for examining an array having large spacings between elements. The Rectangular Radiator Method, on the other hand, represents the source by a number of source elements too large to be represented as point sources. The largest sub-element size that maintains the desired accuracy will

minimize the calculation time. This method is well suited for a wide range of field point locations and element sizes.

Since the goal of an ultrasonic hyperthermia array is to localize heating, an equation relating heat generation as a function of spatial intensity or pressure becomes desirable. Equation (3.4) relates the heat generation per unit volume with the square of the acoustic pressure p_o [Nyborg, 1981]:

$$< g_v > = \alpha p_o^2 / \rho c \qquad (3.4)$$

where α, ρ, and c are attenuation, density, and sound velocity, respectively, of the medium. This equation allows the heating rate at any location in the field to be calculated from the knowledge of the pressure amplitude at that position.

3.3. Computer Simulated Field Patterns

A program to calculate an array of points for making a contour plot representing the pressure field from a planar nonphased array appears in Appendix D. This program uses the Rectangular Radiator Method to approximate the pressure fields [Ocheltree, 1984]. All simulations are carried out at a frequency of 1000 kHz with an attenuation of 0.00022 Np/cm for water or 0.0806 Np/cm in tissue. The neper (Np) is a dimensionless unit of attenuation for waves decaying exponentially with distance. The sources are square transducer elements of dimension 3.6 cm x3.6 cm (1.42 in x 1.42 in). Simulations from this program (Figs. A.1-39) produce the estimated field patterns in both the axial and transverse directions from a given set of source elements and conditions.

Objectives for the collection of simulated near field patterns include (1) an attempt to generate field intensity patterns which accurately predict the field characteristics observed from square array transducers under experimental conditions, (2) an effort to illustrate the shape of a two dimensional region of the field in a plane perpendicular to the transducer by generating contour plots from the theoretical model, and (3) a simulated testing of several system parameters to predict their effects on the shape of the field intensity pattern. During this process, methods are identified for creating patterns useful in hyperthermia therapy.

Plots of intensity in decibels ($dB = 10 \log (I/I_o) = 20 \log (p/p_o)$) versus position that characterize the field include transverse scans, axial scans, and contours. A transverse scan represents the relative intensity at a constant distance from (along a path parallel to) the face of the transducer. Each transverse scan path length is greater than the length of a side of a transducer element. Transverse scans are taken at two distances: $z = 7.0$ cm and $z = 13.0$ cm from the transducer face. These distances fall within the treatment range of interest $5.0 \leq z \leq 20$ cm (2 to 8 inches) determined by the length of the coupling bolus and the penetration depth of ultrasound at 1 MHz in tissue. Characteristics of the transverse scan include qualitative shape, maximum ripple amplitude, and 3 dB width. Different shapes of the intensity profile produce varying temperature distribution patterns in tissue. The 3 dB width gives an estimate of the beamwidth which will deposit at least

half the total acoustic power. Ripple amplitude specifies the intensity variations of an acoustic beam within the 3 dB width.

Contour plots represent a two dimensional picture of the constant dB intensity lines for a plane perpendicular to the transducer face through its geometric center including the treatment region. It shows the relative intensity patterns in both the transverse and axial directions simultaneously. The contour plot also indicates the position of predicted maximum and minimum acoustic intensity in the field. The 3 dB contours identify the region of the beam that deposits half the total acoustic power in tissue.

Variations of several medium and system parameters such as the attenuation of tissue versus water, amplitude and phase of adjacent elements and the velocity amplitude profile across the transducer face affect the near field patterns. The predicted effects of adjusting these parameters are illustrated by the results of several simulations. These simulations show the adequacy of the theoretical model in predicting experimentally observed patterns, and suggest possible improvements in the model. Possible methods of producing patterns useful in hyperthermia therapy can also be simulated. The adjustments of amplitude and phase on adjacent elements are efforts to meet the goals of hyperthermia treatment: minimization of hot spots and the production of a uniform temperature distribution in the treatment region of the tissue.

The first set of simulations (Figs. A.1-6) predicts the near field intensity patterns from a single square element of dimension 3.6 cm x 3.6 cm (1.42 in x 1.42 in) at 1 MHz for a

water load. The contour plot (Fig. A.1) shows the 3 dB contours of the intensity extending from the face of the transducer to a depth of 10 cm. This is a prediction of what the field intensity looks like within the coupling bolus $0 \leq z \leq 5.0$ cm (0 - 2 inches). Figure A.2 shows the 1 dB contours of intensity in the range $5.0 \leq z \leq 20$ cm (2 - 8 inches). Comparing Fig. A.23 with Fig. A.24, the effects of tissue attenuation versus water become apparent from the contour plots of near field intensity in the range 5.0 - 15 cm from a single square element.

The simulated transverse scans at $z = 7.0$ cm (Fig. A.3) and at $z = 13.0$ cm (Fig. A.4) have 3 dB widths of 2.7 and 2.6 cm, respectively. The axial scan for the range $0.1 \leq z \leq 10$ cm from the transducer face (Fig. A.5) predicts the near field axial intensity pattern including the water coupling bolus. The axial scan that covers the distance $5.0 \leq z \leq 10$ cm transducer face (Fig. A.6) includes the entire treatment range of interest.

Adjacent double element patterns (Figs A.7-19 and A.24-35) represent predicted near field intensity patterns from a pair of adjacent square elements, each with the same dimensions as the single element at 1 MHz in water. Contour plots (Figs. A.7 and A.8) represent double element intensity patterns $5.0 \leq z \leq 15$ cm from the transducer in the axial direction and $-5.0 \leq x \leq 5.0$ cm in the transverse direction, with the origin at the geometric center between the two elements. A comparison of Fig. A.7 for the pattern from two adjacent elements driven at equal amplitude with Fig. A.8 shows the altered pattern when one of the adjacent elements is driven at half the amplitude of the other.

Transverse plots (Figs. A.9-13) show the amplitude variation effects at two depths in the field. Figure A.9 predicts a 3 dB width of 6.4 cm at z = 7.0 cm and Fig. A.13 predicts a 3 dB width of 2.7 cm z = 13 cm.

Axial plots in Figs. A.14-19 show amplitude variation effects on and off axis from the geometric center between the two elements. Each axial plot covers the range from $5.0 \leq z \leq 20$ cm from the transducer. Figure A.14 predicts the axial pattern at the geometric center for a pair of adjacent elements driven at equal amplitude. For one adjacent element at 1/4 power, Fig. A.15 predicts the adjustment to the axial pattern at the geometric center; Fig. A.16 and Fig. A.17 predict the axial pattern slightly displaced along the x-axis from the geometric center. Figure A.16 shows the axial pattern displaced to the left of the geometric center (x = -5 mm) in front of the element driven at full power. Figure A.17 shows the axial pattern displaced to the right (x = +5 mm) in front of the element driven at half power.

Transverse plots in Figs. A.24 and A.25 show the effect of driving an element at 75% amplitude (half power) relative to its adjacent element. The 3 dB widths become 6.1 cm (at z = 7.0 cm) and 5.7 cm (at z = 13.0 cm). Axial plots in Figs. A.26-28 show the axial patterns on and off geometric center for this situation. Contour plot Fig. A.29 contains all the information shown in Figs. A.24-28 in two dimensional form summarizing the results of this amplitude variation.

Figures A.30-35 predict the effects of a 90 degree phase difference between neighboring elements driven at equal

amplitude. Transverse plots (Figs. A.30 and A.31) show the 3 dB width at z = 7.0 cm (6.3 cm wide) and z = 13.0 cm (5.9 cm wide) in the field of this double element pattern. Axial plots (Figs. A.32-34) show the axial patterns on and off geometric center. The contour plot shown in Fig. A.35 pictorially summarizes the results of this phase difference simulation in two dimensions.

CHAPTER 4

EXPERIMENTAL APPARATUS AND TECHNIQUES

4.1. An Ultrasonic Transducer Scanner System

Characterization of the three dimensional spatial field patterns produced by an ultrasonic applicator requires a versatile, automated system designed to gather sets of data along specified lines or planes in the field. A semiautomated computer controlled system designed for ultrasonic field scanning [Padgitt, 1984] fulfills these requirements. This three-axis computer-controlled acoustic field measurement system, hereafter termed "Scanner System," was used to characterize both the 16-element and the 4-element square array transducer applicators examined in this study. The Scanner System collects data along scan paths in the axial and transverse directions, under software control, using user specified scan limits and sample increments. For a more complete picture, the system automatically collects data along multiple scan paths in a plane parallel to the transducer. All data acquired may be stored on disk for subsequent plotting with additional software.

The Scanner System (Fig. 4.1) consists of mechanical hardware electronically controlled by an Apple IIe Computer. A rigid mechanical arm holds the ultrasonic receiver probe inside the water tank within the ultrasound field of the transducer applicator. An axis positioning system moves the arm in the x, y, or z direction by means of a stepper motor dedicated to each axis. Figure 4.2 shows the tank coordinate conventions. The stepper motors follow the commands of the stepper driver linked

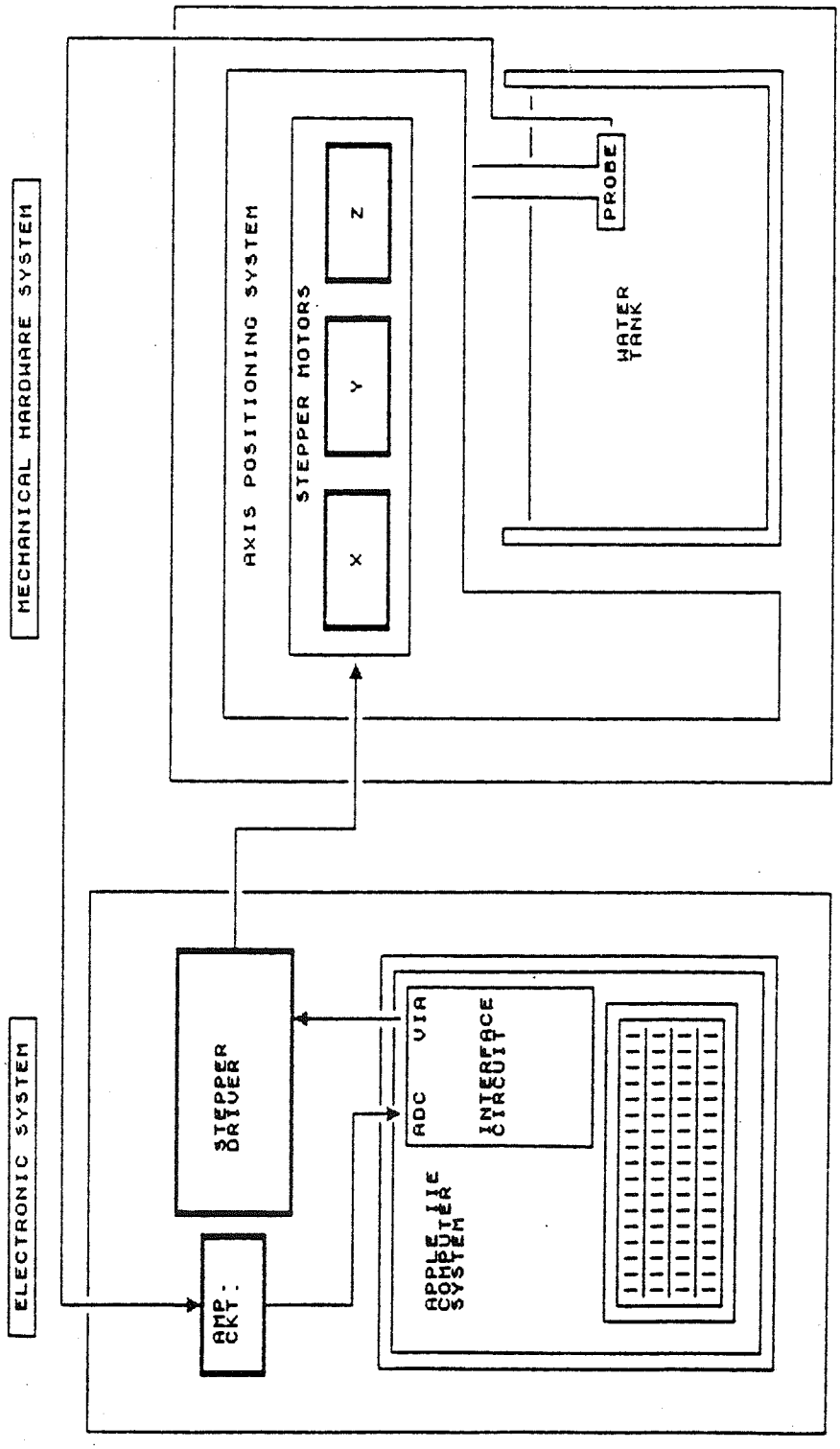

Figure 4.1. Scanner system diagram.

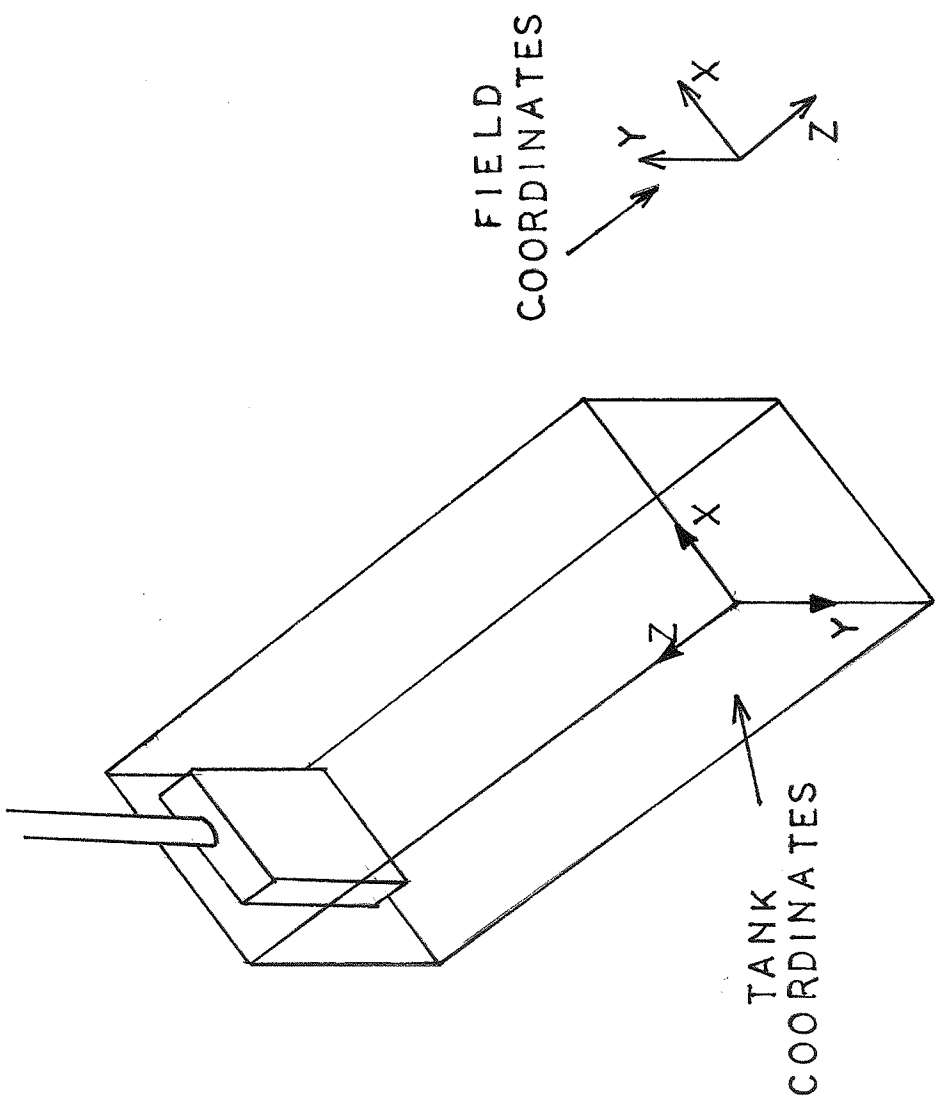

Figure 4.2. Tank and field coordinate conventions.

to the Apple IIe computer system. The other link to the Apple IIe computer handles input data acquired from the ultrasonic receiver probe.

The 1 MHz RF signal from the receiver probe is isolated by an amplifier circuit (Fig. 4.3) which converts it to a DC signal and amplifies the signal to a 0 - 10 volt range before analog-to-digital conversion (AD572) on the interface circuit board. Due to the high Q matching transformer and characteristic gain of the amplifiers, the system operates optimally for continuous wave (CW) signals at a frequency of 1 MHz.

Several constraints of the experimental procedure and apparatus necessitate modifications to the scanner system as originally designed. For precise measurements of acoustic pressure as a function of position, vibrations in the mechanical support arm holding the receiver must be minimized. Thus, the support arm must have both stiffness and damping properties to have sufficient stability, while conforming to size constraints imposed by the watertank. To minimize stress at the joint of the arm bracket, a small mass is desired. A mechanical arm that satisfies these constraints was developed. It consists of two thick alumimum angle brackets bolted together to form a "T" and welded to an aluminum block. A mounting structure hangs vertically on the end of this arm to hold the receiver probe.

Walls of an enclosed water tank pose a problem for acoustic measurements due to standing wave interference patterns produced by reflections at the water-wall interface. Since reflections occur at the tank wall to the impedance mismatch, one

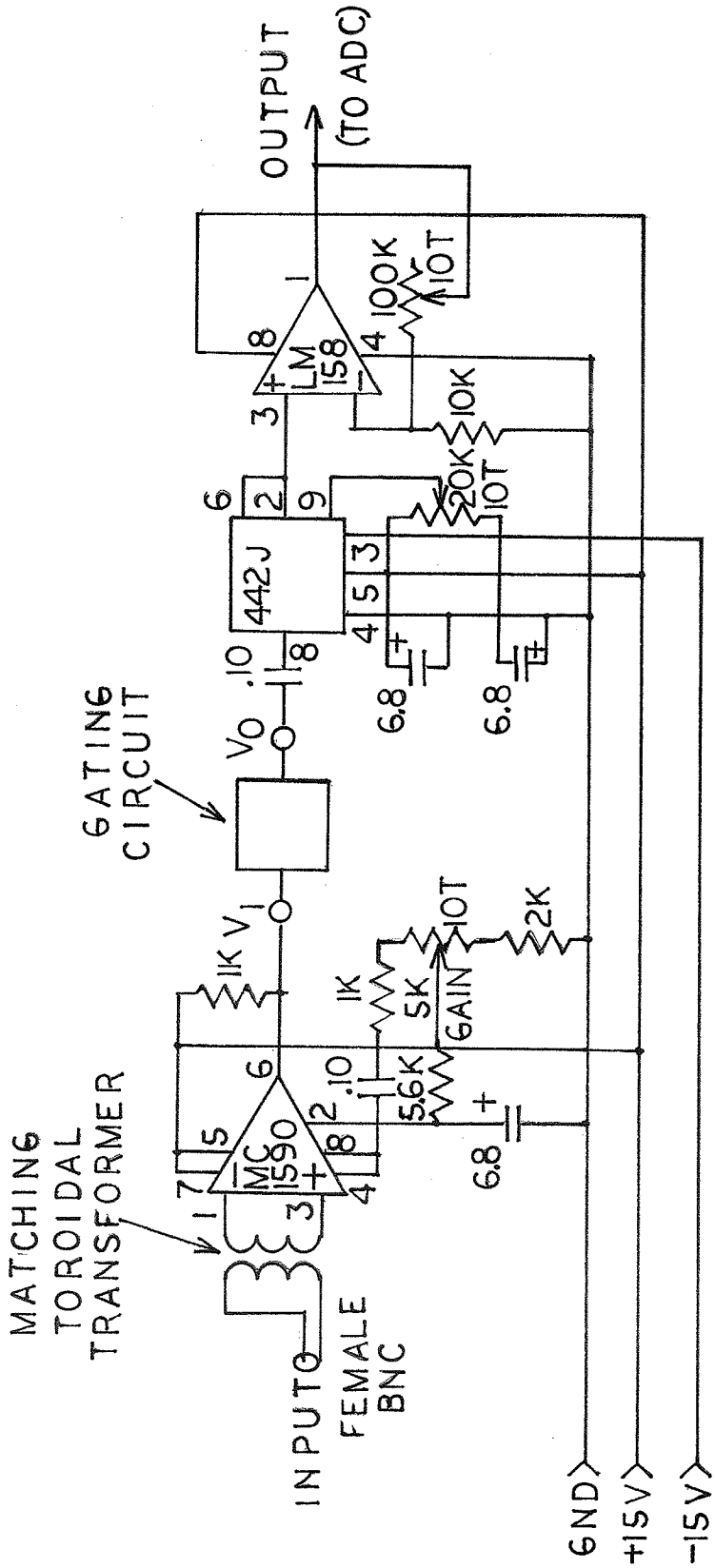

Figure 4.3. Amplifier circuit scehmatic.

solution involves lining the tank with an absorbing material sufficient to eliminate any reflected sound power. This turns out to be an effective approach, but is costly to implement.

Alternatively, an electronic approach using pulsed signals solves the standing wave interference problem. Gating the 1 MHz sine wave signal to the transducer elements with a short pulse produces a burst of RF with a corresponding burst of acoustic pressure propagating through the water. With the help of an electronic range gate at the receiver, extraneous echos can be eliminated so that the receiver sees only the directly incident RF burst. The range delayed gate pulse eliminates echoes or reflections of the RF burst under the assumption that the directly incident burst travels along the miminum path length from transducer to receiver, whereas reflected bursts travel a greater distance.

Reflected bursts or echos have a greater time delay than the directly incident ones. Echoes arriving at the receiver at a time delay coherent with the pulse frequency, however, could conceivably cause interference, resulting in erroneous data. Fortunately, transverse scans of a single element performed at two different pulse frequencies showed little difference, suggesting that "coherent" interference is minimal (Figs. B.2 and B.3).

Implementation of the pulsed system to minimize standing wave interference requires an extra signal source and additional circuitry. The circuit components required to realize an adjustable range gate appear on the schematic shown in Fig. 4.4 as modifications to the interface board of the Scanner System.

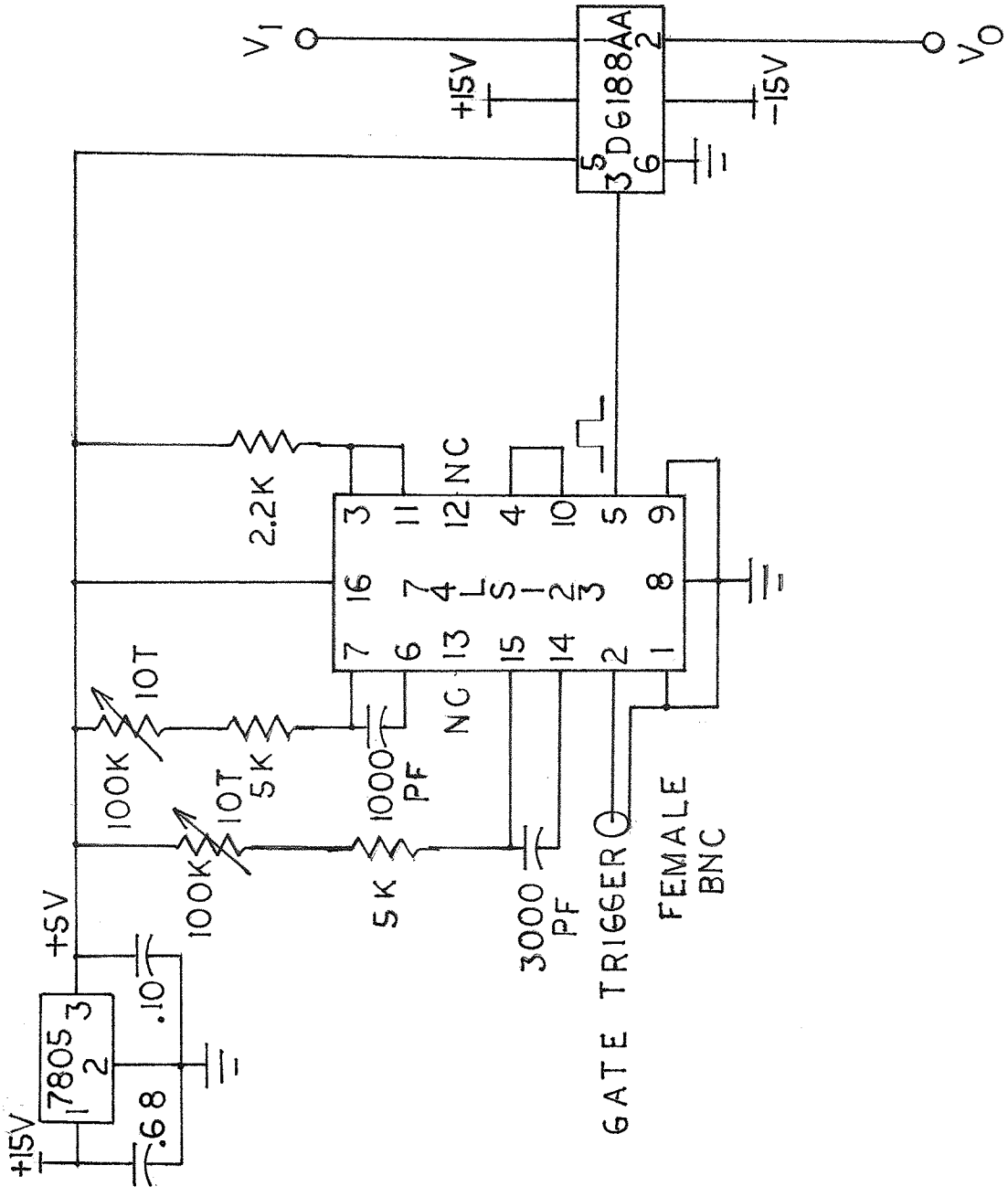

Figure 4.4. Gating circuit schematic.

Two 74LS123 monostable multivibraters (one-shots) are added to achieve the delayed gate signal which activates the Field Effect Transistor (FET) switch connecting the output of the MC1590 input amplifier to the 442J RMS to DC converter. The first one-shot produces a range delay in response to the trigger signal. The second one-shot creates a gate signal in response to the falling edge of a pulse from the first one-shot. The range delay and gate width are each adjusted independently by a 10 turn control potentiometer. The range delay operates from a minimum of 5 μs to 120 μs allowing a possible range of 0.75 cm to 18 cm of distance in water between the transducer and receiver. Gate width ranges from a minimum of 16 μs to a maximum of 40 μs. These limits provide enough flexibility to make measurements within the treatment range of interest.

A Wavetek signal generator provides a 1 MHz 30 volt peak-to-peak sinusoidal signal to drive the transducer elements of the ultrasonic applicator at low power. Gating the 1 MHz signal source is an HP 8111A Pulse/Function generator which generates a short pulse for both the Wavetek and the interface board. The rising edge of the gate pulse triggers the range gate on the interface board. This synchronizes the RF burst at the transducer with the range gate isolating the burst at the receiver. The HP generator outputs the gate pulse at a 5 kHz repetition rate (T_R = 200 μs) with a pulse width t_w = 5.6 μs. Approximately five cycles of the 1 MHz signal are contained within this gate pulse to drive the transducer.

Original design of the Scanning System assumed operation with CW signals only. Consequently, conversion to a pulsed

system required additional modifications. A pulsed RF input at a given amplitude to the 442J RMS to DC converter lowers the DC output to a fraction of the level normally seen by the CW RF input signal at the same amplitude. Definition of root-mean-square (RMS) predicts reduction by a factor equal to the square root of ratio of the pulse width to the pulse repetition period ($K = t_w/T_R = 0.167$). To utilize the full 0 - 10 volt input range of the AD572, gain from the LM158 op-amp performing the amplification must be compensated by a factor of $1/K = 6$. A simple way to boost the gain of this inverting amplifier is to reduce the input resistance R_i by the same factor (since the gain $G = -R_f/R_i$), although this also increases the noise level at the output. A 10 kilohm potentiometer added in parallel with the original 10 kilohm input resistor accomplishes this task with a degree of control for adjustment purposes.

4.2. Calibration of the Ultrasound Receiver

Measurement of acoustic pressure and intensity in the field of an ultrasound source requires a small detector that produces minimum interference in the field, provides adequate lateral resolution, and performs linearly with enough sensitivity over a low intensity range. A type of ultrasound receiver used for this purpose is called a hydrophone probe. The Dapco NP-10 Model 40735 (Ridgefield, CT.) hydrophone consists of a thin cylindrical transducer inserted in a syringe needle housing that detects ultrasound by producing a voltage proportional to the received pressure. Since intensity is proportional to the square of

acoustic pressure, the hydrophone received intensity is proportional to the square of the output voltage.

Calibration tests performed on the Dapco hydrophone showed that it meets the prescribed specifications. A focused 1 MHz source transducer precalibrated by thermoelectric techniques serves as the standard for these tests. Figure 4.5 shows a plot of output voltage squared (V^2) versus intensity. The data are linear in the intensity range of 0 - 5 W/cm^2 with a sensitivity constant K = 19.4 $W/cm^2/(V^2)$ for RMS volts. A transverse profile across the focused beam performed by the Dapco hydrophone receiver shows a 0.40 cm (3 dB) beamwidth. However, the same profile performed by thermoelectric techniques gives a 0.50 cm beamwidth (Fig. 4.6). Thus, the Dapco hydrophone appears to have a slightly reduced sensitivity near its edges. However, for the purposes of this study, the Dapco hydrophone provides adequate resolution and linearity for characterizing the ultrasound field produced by planar square elements.

4.3. Scan Data Acquisition and Plotting Procedures

The procedure for collecting data on single and multiple element transducer patterns from the square array applicators involves the systematic use of software routines developed for the Scanner System. Initially, the hydrophone is manually positioned at the origin, such as the geometric center of a single or pair of square elements, and as close as safely possible to the transducer face. Once this is accomplished, the controller "homes" the hydrophone to establish the range of each coordinate axis relative to the chosen origin. When a new z-axis

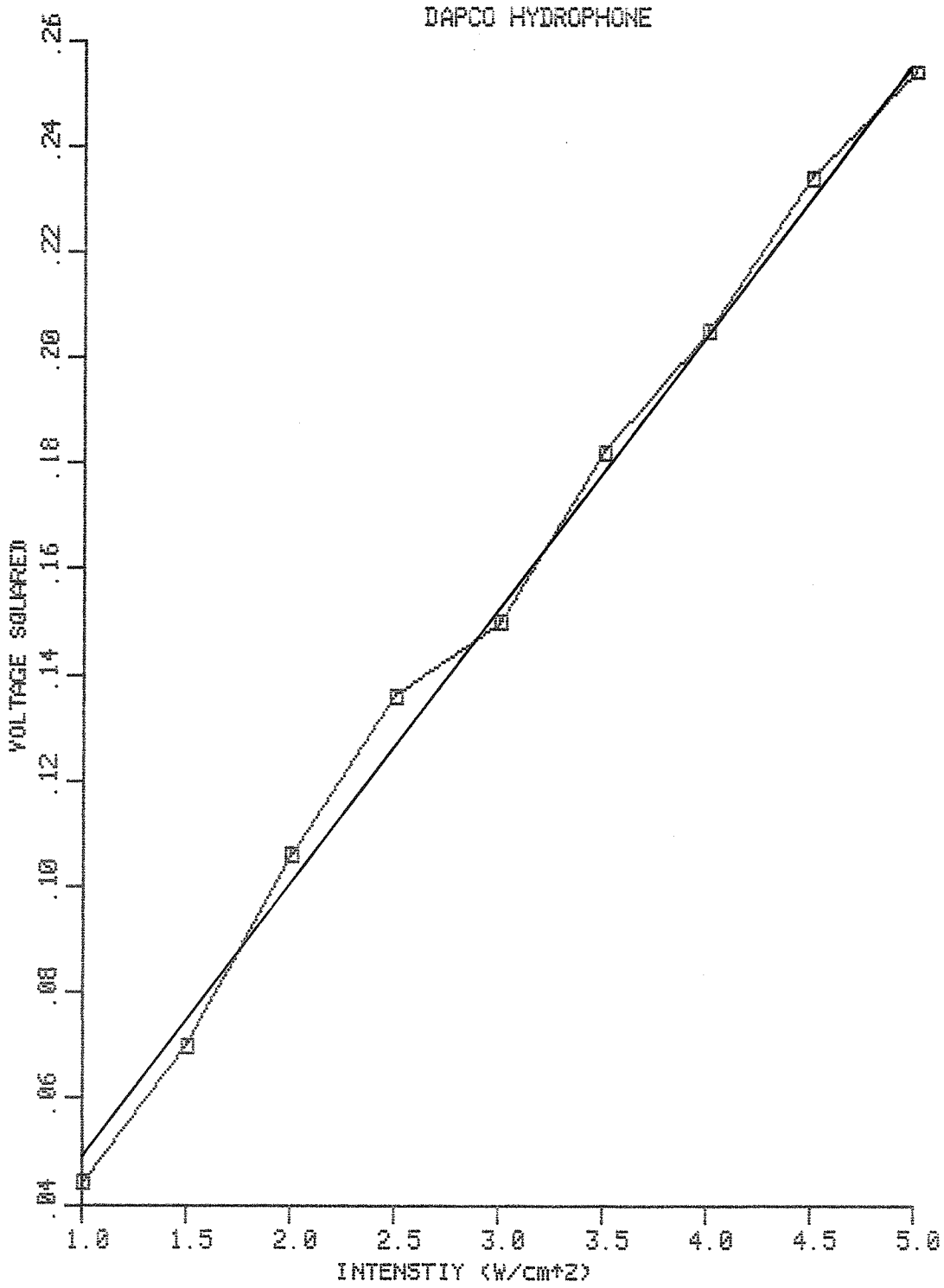

Figure 4.5. Sensitivity calibration curve for the Dapco hydrophone receiver.

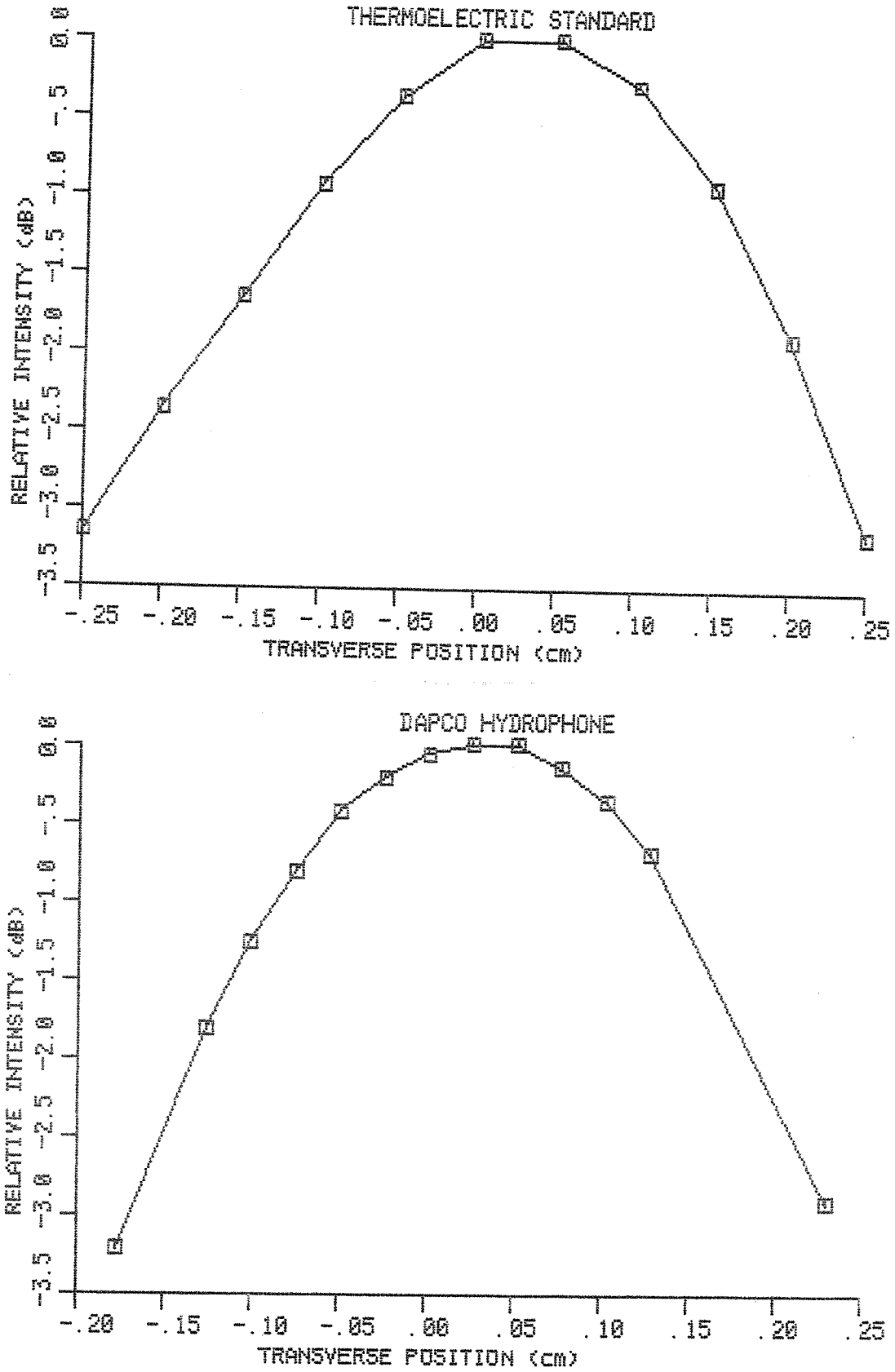

Figure 4.6. Intensity profiles from a focused transducer at 996 MHz, 37°C, for calibration of the Dopco hydrophone with a thermoelectric standard.

position is selected, the controller takes the hydrophone to the new position at a distance d = z from the transducer. Software routines carry out these procedures before each transverse or longitudinal (axial) scan.

In order to prepare for either a transverse or longitudinal scan, the range delay, gate width, and amplifier gain must all be adjusted. This procedure minimizes interference and puts all data points (voltages) within the proper range to maximize resolution. The highest peak encountered in the range of interest may be identified by manual or automatic peak detection. These options are available in the software menu. Once the highest peak is located, range delay and gate width adjustment isolates the primary RF burst. Gain compensation keeps the LM158 output voltage near the top of the input range of the AD572 (for maximum resolution) and just below the saturation level. The scan and immediate data display software option tests the adequacy of these adjustments over the range of interest by displaying points graphically on the CRT screen.

An automatic transverse scan samples voltages (proportional to acoustic pressure) across an x-range and y-range at a sampling rate determined by the x-increment and y-increment. The operator specifies a zero y-range for a single scan across an x-range distance through the origin (geometric center) at sampling intervals of the x-increment. However, if the operator specifies a nonzero y-range, multiple transverse scan paths are carried out in the x-direction over intervals of the y-increment in the y-direction. After the system performs transverse scan according to these specifications, it stores the collected data in binary

form on a separate disk. The operator names the data file appropriately.

Longitudinal (axial) scans become more difficult to perform with the pulsed range-gated system. Longitudinal scans are limited to short ranges in the z-direction so that the range delay can manually follow the increasing delay of the primary burst received at the hydrophones as it moves away from the transducer. Longitudinal scan data are also stored on a separate disk.

Plots of scan data acquired by the scanner system are drawn by an HP-7074A pen plotter on the instructions of a BASIC program executed by the Apple IIe computer. Three programs for plotting microwave antenna measurement data [Benson, 1985] were modified to create plots of acoustic intensity (dB) versus position (cm). Listings of these programs appear in the Appendix D.

Program TRANSVERSE.PLOT creates a three dimensional illustration of the relative intensity (dB) versus position in the x - y plane based on multiple transverse scans. This creates a valuable picture for qualitative evaluation of the beam, but quantitative evaluations are difficult due to multiple lines, the angular perspective and an unreferenced peak. For this reason, two dimensional plots offer more reliability for quantitative results and comparisons.

Program XPLANE.PLOT prints a title, descriptive information heading identifying important test parameters and the 3 dB bandwidth for a transverse scan. XPLANE.PLOT plots only a single transverse scan in the x-direction showing intensity versus x-axis position. The y-axis position is assumed zero. This

represents an x-axis profile of the beam through the geometric center.

Program AXIAL.PLOT makes plots of longitudinal (axial) scans like XPLANE.PLOT with the following exceptions. AXIAL.PLOT excludes the 3 dB bandwidth measurement and plots intensity versus distance from transducer face (z-axis position) with an unreferenced peak.

CHAPTER 5

EXPERIMENTAL RESULTS OF SCANNING THE ACOUSTIC FIELDS FROM TWO MULTIELEMENT SQUARE ARRAY APPLICATORS

5.1. Single Element Patterns

The experimental apparatus and procedures described in Chapter 4 provide a means to characterize the single element patterns of two ultrasonic transducer applicators: a 4-element and a 16-element square array. Each 3.6 cm x 3.6 cm element is driven at low power (< 1 Watt) in a tank with a water load. Results of experimental measurements are shown in Figs. B.1-30. Patterns are examined at two positions within the treatment range of interest. Objectives for characterization of single element patterns include (i) qualitative evaluation of shape, (ii) quantitative measurement of 3 dB beamwidth and ripple amplitude, (iii) investigation of beam pattern variations as a result of element position in the array. In Chapter 6 these results will be interpreted and compared with the results of single element pattern simulation.

The first set of single element patterns were generated from the 4-element square array using a pulsed 1.0 MHz signal and the ultrasonic transducer scanner system described in Chapter 4. Figure 2.2 shows the element numbering scheme for each applicator. An axial scan (Fig. B.1) through the geometric center of element 1 for the range $4.0 \leq z \leq 7.0$ cm from the transducer face shows a maximum ripple amplitude of 1.7 dB. A transverse scan (Fig. B.2) of element 1 at z = 7 cm from the transducer indicates a 2.3 dB half-power beamwidth. An identical

transverse scan (Fig. B.3) performed on element 1 at a pulse repetition frequency f_R = 1 kHz shows the effect of coherent interference. All other scans are performed at f_R = 5 kHz. A transverse scan of element 1 at a z = 13.0 cm shows a 1.8 cm 3 dB beamwidth.

Results of transverse scans on elements 1 - 4 at z = 7.0 cm (Figs. B.2-7) and z = 13.0 cm (Figs. B.20-24) depths are summarized in Table 5.1. The average 3 dB beamwidth at z = 7.0 cm is 2.3 cm and at z = 13.0 cm is 1.7 cm. The single element pattern (Fig. B.22) for f = 997 kHz shows the effect of a small frequency drift when compared to the single element pattern (Fig. B.21) for f = 1000 kHz.

The second set of single element patterns comes from manual scans of a 16-element square array using a pulsed 1 MHz signal. Voltages were read from an oscilloscope and translated to relative dB intensity. Transverse scans for elements 1 - 16 are summarized on a single graph (Fig. B.28). Table 5.2 contains the results of 3 dB beamwidth and maximum ripple amplitude measurements at z = 7.3 cm. The average 3 dB beamwidth is 2.8 cm.

Single element beam patterns from the 16-element applicator have position dependencies. Edge elements generally produce a pronounced assymetric peak closer to their respective clamped edges (Fig. B.29). Only element 1 and 13 are exceptions to this rule. Middle elements (e.g., Fig. B.30) generally project a triple symmetric peak with 0.5 - 2 dB ripple amplitude. Only element 7 deviates from this rule.

Table 5.1. Experimental Results of Transverse Beam Scans from Single Elements of a 4-Element Square Array

SOURCE (Figure)	ELEMENT IDENTITY	AXIAL DISTANCE x(cm)	HALF-POWER BEAMWIDTH (cm)	MAXIMUM RIPPLE AMPLITUDE (dB)
B.2	1	7.0	2.3	0.6
B.3	1	7.0	2.4	1.3
B.4	2	7.0	2.2	1.5
B.5	3	7.0	2.0	1.0
B.6	3	7.0	2.3	1.1
B.7	4	7.0	2.6	2.3
B.20	1	13.0	1.8	1.3
B.21	2	13.0	1.7	2.5
B.22	3	13.0	1.6	0.4
B.23	3	13.0	1.7	0.2
B.24	4	13.0	1.7	2.9
B.2-7	1-4 (Avg)	7.0	2.3	1.3
B.20-24	1-4 (Avg)	13.0	1.7	1.4

Table 5.2 Experimental Results of Transverse Beam Scans at z = 7.3 cm from Single Elements of a 16-Element Square Array

ELEMENT IDENTITY	HALF-POWER BEAMWIDTH (cm)	MAXIMUM RIPPLE AMPLITUDE (dB)
1	2.84	1.2
2	2.84	0.8
3	2.69	0.8
4	2.49	1.8
5	2.79	1.7
6	2.90	0.7
7	2.69	1.2
8	2.56	1.5
9	2.74	1.5
10	2.90	1.0
11	2.87	1.3
12	2.59	2.2
13	2.69	1.9
14	2.97	1.7
15	2.90	1.4
16	2.67	3.2
1-16	2.76±0.14 (Avg)	1.5±0.6

5.2. Multiple Element Patterns

The next step of investigation involves characterization of adjacent double element patterns from the 4-element and 16-element arrays. In addition, experiments showing the effect of amplitude and frequency variations are presented. Plots illustrate qualitative shape as well as 3 dB beamwidth and ripple amplitude.

First, the set of results from the 4-element square array are presented. A transverse scan of the double element pair 1, 2 driven at equal amplitude (Fig. B.8) shows a pattern having a 6.1 dB beamwidth at a z = 7.0 cm depth. The peaks for the 1, 2 element pair (Fig. B.10) look slightly more symmetric when the input impedance difference between elements is compensated by attenuators.

The transverse scan from the double element pair 3, 4 (Fig. B.12) shows a marked improvement in symmetry and ripple amplitude when compensated for input impedance differences (Fig. B.14). The effect of a 7 kHz off resonance frequency shift is illustrated by the 3, 4 double element pattern at 993 kHz (Fig. B.17) when compared with the 3, 4 pattern at 1000 kHz (Fig. B.14). The frequency shift introduces a 5.5 dB crevice into the transverse profile. At 13.0 cm, the 1, 2 double element transverse scan (Fig. B.18) and the 3, 4 element transverse scan (Fig. B.25) show comparable 3 dB beamwidths (5.7 cm).

The effect of a 50% power variation on adjacent double elements is tested on the 1, 2 double element pattern (Figs. B.9, B.11, B.19) and the 3, 4 double element pattern (Figs. B.13, B.15, B.26). Ripple amplitude increases 1 - 3 dB from the

equal amplitude case. Results of double element patterns from the 4-element square array are presented in Table 5.3.

Results from the 16-element applicator show the value of using superposition to predict multiple element patterns from single element components. A transverse scan from double element pair 6, 7 was compared to the corresponding transverse scan made up of the superposition of the individual transverse scans of elements 6 and 7. The experimentally scanned double element pattern has a 3 dB beamwidth of 6.25 cm whereas the superposition of individual elements predicts a beamwidth of 6.02 cm.

Expanding on the results of double element patterns are the patterns from 4- and 16-element arrangements. Three typical multiple element patterns are characterized here: (1) a linear-4-element pattern, (2) a square block-of-4-element pattern and (3) a square block-of-16-element pattern. The transverse scan from elements 9, 10, 11, and 12, a linear-4-element arrangement, has a 3 dB beamwidth of 13.7 cm. This was manually measured data. The transverse scan of elements 6, 7, 10, and 11, a square block-of-4-element arrangement has a 3 dB beamwidth of 6.6 cm. An axial scan of the same block-of-4 arrangement has an amplitude of 3.5 dB. Finally, an axial scan of the entire 16-element array shows a maximum ripple amplitude of 7 dB. The latter three scans were obtained with cw signals in a tank lined with SoAb rubber to reduce standing wave interference. Results of these multiple element beam scans are summarized in Table 5.4.

Table 5.3. Experimental Results of Transverse Beam Scans from Adjacent Double Elements of a 4-Element Array

SOURCE (Fig.)	ELEMENT IDENTITY	AXIAL DISTANCE z (cm)	RELATIVE POWER (%)	IMPEDANCE COMPENSATION	HALF-POWER BEAMWIDTH (cm)	MAXIMUM RIPPLE AMPLITUDE (dB)
B.8	1,2	7.0	100	NO	6.1	3.2
B.9	1,2	7.0	50	NO	5.7	6.0
B.10	1,2	7.0	100	YES	6.1	3.0
B.11	1,2	7.0	50	YES	5.8	5.2
B.12	3,4	7.0	100	NO	5.7	4.8
B.13	3,4	7.0	50	NO	2.8	6.7
B.14	3,4	7.0	100	YES	5.7	2.2
B.15	3,4	7.0	50	YES	5.9	3.4
B.10,14 (Avg)	1,2&3,4	7.0	100	YES	5.9	2.6
B.11,15 (Avg)	1,2&3,4	7.0	50	YES	5.8	4.3
B.18	1,2	13.0	100	YES	5.7	2.8
B.19	1,2	13.0	50	YES	2.1	5.8
B.25	3,4	13.0	100	YES	5.7	3.3
B.26	3,4	13.0	50	YES	5.3	5.8
B.18,25 (Avg)	1,2&3,4	13.0	100	YES	5.7	3.0
B.19,26 (Avg)	1,2&3,4	13.0	50	YES	3.7	5.8

Table 5.4. Experimental Results of Field Characteristics from Four Element Arrangements of a 16-Element Array

ELEMENT IDENTITY	ELEMENT ARRANGEMENT	AXIAL DISTANCE z (cm)	SCAN TYPE	HALF-POWER BEAMWIDTH (cm)	MAXIMUM RIPPLE AMPLITUDE (dB)
9,10,11,12	row-of-4	7.3	transverse	13.7	2.3
7,8,11,12	block-of-4	11.5-20.0	axial	---	2.8
6,7,10,11	block-of-4	2.5-20.0	axial	---	3.5
6,7,10.11	block-of-4	7.6	transverse	6.6	4
1-16	block-of-16	2.5-20.0	axial	---	7

CHAPTER 6

DISCUSSION AND INTERPRETATION OF RESULTS

6.1. Comparison of Experimental Beam Scans with Computer Simulated Patterns

This section evaluates the extent of agreement between results of experimental beam scans and corresponding computer simulated beam patterns. Single element beam scans from the 4-element and 16-element square array applicators are compared with the simulated field patterns from a single element. Adjacent double element beam scans are compared with the corresponding simulated patterns including the effect of relative amplitude variations. Multiple element patterns receive brief comment. The characteristics used for comparison include qualitative shape, maximum ripple amplitude, and 3 dB beamwidth.

The average 3 dB beamwidth and maximum ripple amplitude for individual elements in the 4-element and 16-element square array applicator at depths of z = 7.0 and z = 13.0 cm in the field taken from Table 5.1 and Table 5.2 are compared in Table 6.1 with the 3 dB beamwidth and maximum ripple amplitude obtained from computer simulation. The 3 dB beamwidth for single elements in the 4-element array measures 4 mm (15%) short of the predicted width at z = 7.0 cm and 9 mm (35%) short of the predicted width at z = 13.0 cm. Also, the beam peaks in experimental scans are smoother with less than half the predicted ripple amplitude. These discrepancies might be explained by inadequacies in the numerical model used for simulation. The effect of assuming a nonuniform velocity amplitude profile across the face of a

Table 6.1. Simulated and Experimental Results of Single Element Transverse Beam Scans

SOURCE (Fig./Table)	AXIAL DISTANCE z (cm)	HALF-POWER (3 dB) BEAMWIDTH (cm)	ERROR (%)	MAXIMUM RIPPLE AMPLITUDE (dB)	ERROR (%)
4ESA (avg.) Table 5.1	7.0	2.3	-15	1.3	-52
Simulation Figure A.3	7.0	2.7		2.7	
4ESA (avg.) Table 5.1	13.0	1.7	-35	1.4	-67
Simulation Figure A.4	13.0	2.6		4.3	
16ESA (avg.) Table 5.2	7.3	2.8	0.0	1.5	---
Simulation Figure A.21	7.3	2.8		---	

transducer to account for mechanical damping is discussed in Section 6.3.

The average 3 dB beamwidth of a single element at a distance z = 7.3 cm from the 16-element array exceeds the predicted beamwidth at z = 7.0 cm by 1 mm (4%). A single element contour plot (Fig. B.22) predicts this result since the 3 dB contour broadens beyond a depth of z = 7.0 cm. The 3 dB beamwidth at z = 7.3 cm measured from the contour plot is 2.8 cm matching the experiment results identically. Ripple amplitude, however, is much smaller than predicted. As previously noted, inadequate modeling of the transducer may account for this discrepancy.

An investigation of positional effects, as noted in Section 5.1, reveals a dependency of the shape of the beam pattern from a single element on the position of that element in the 16-element array. Edge elements mechanically clamped near the end of the scan path frequently show a pronounced assymmetric peak near that edge. Middle elements which have no clamped edge usually project a triple symmetric peak. This effect is most likely explained by reduced mechanical damping of adjacent elements at the outer edge. Electrical grounding of the edge elements relative to middle ones may also be a factor.

To check the reliability of experimental results, tests were carried out to demonstrate repeatability of measurements and the effects of coherent interference at the pulse repetition frequency f_r = 5 kHz. Transverse scans (Figs. B.5 and B.6) performed on the same element show 3 dB beamwidths that differ by 3 mm. Ripple amplitude differs by 0.1 dB. This result suggests some significant random error in the measurements. Transverse

scans (Figs. B.2 and B.3) are performed on the same element at different pulse repetition frequencies to show the effects of any coherent interference. The 3 dB beamwidths differ by 1 mm, which is relatively insignificant. Ripple amplitude differs by only 0.7 dB. This suggests that coherent interference has minimal effect on measurements.

Table 5.3 lists average characteristics of beam patterns from adjacent double elements with the effect of amplitude variation using the 4-element array. Table 6.2 compares these results with simulated adjacent double element patterns with amplitude variation.

At a depth of z = 7.0 cm, the 3 dB acoustic half-power beamwidth measured from a pair of adjacent elements with one driven at half-power (71% amplitude) is 2.4 mm (70%) greater than predicted. Because of irregular peaks, the 3 dB half-power beamwidth becomes an inconclusive characteristic for comparison of this case. Maximum ripple amplitude, however, is closer to the predicted 3.9 dB, exceeding it by only 0.4 dB (10%). The equal amplitude case at z = 7.0 cm shows 3 dB beamwidth and ripple amplitude that fall just below the predicted values. Experimental results at z = 13.0 cm do not agree as well with the simulation, probably due to experimental error. An error such as an undetected frequency shift during the procedure could easily alter the beam pattern to explain these results.

Table 5.4 presents the field characteristics for a particular block-of-4-element arrangement in the axial and transverse directions. While axial pressure amplitude was measured over the range $2.5 \leq z \leq 20$ cm in the experimental case,

Table 6.2. Simulated and Experimental Results of Adjacent Double Element Transverse Beam Scans

SOURCE (Fig./Table)	DEPTH (cm)	RELATIVE ADJACENT ELEMENT POWER (%)	HALF-POWER BEAMWIDTH (cm)	ERROR (%)	MAXIMUM RIPPLE AMPLITUDE dB	ERROR (%)
Simulation Figure A.12	7.0	25	2.9	---	10.0	---
Simulation Figure A.13	13.0	25	2.7	---	10.0	---
4-ESA (avg.) Table 5.3	7.0	50	5.8	+70	4.3	+10
Simulation Figure A.24	7.0	50	3.4		3.9	
4-ESA (avg.) Table 5.3	13.0	50	3.7	-36	5.8	+ 1.8
Simulation Figure A.25	13.0	50	5.8		5.7	
4-ESA (avg.) Table 5.3	7.0	100	5.9	- 7.8	2.6	- 7.1
Simulation Figure A.9	7.0	100	6.4		2.8	
4-ESA (ave.) Table 5.3	13.0	100	5.7	- 8.1	3.0	+ 3.4
Simulation Figure A.10	13.0	100	6.2		2.9	

the simulation covers a shorter range of $5.0 \leq z \leq 15.0$ cm. Thus, caution must be exercised in comparing these results. The experimental scan shows a maximum ripple amplitude of 3.5 dB, whereas the simulated scan predicts at least a 4.5 dB maximum ripple amplitude. This again suggests the hypothesis that the simulation fails to adequately account for mechanical damping realized by the elements in the physical situation. A comparison of the 3 dB beamwidth at 7.6 cm reveals only a small discrepancy between theory and experiment. The measured 6.6 cm beamwidth differs only slightly from the 6.4 cm beamwidth predicted by simulation. However, the maximum ripple amplitude in the transverse direction measures 4 dB compared to the 2.3 dB amplitude predicted in simulations--an unexpected result which cannot be explained by limitations in the model. Table 6.3 summarizes these results.

Since the acoustic field patterns produced from the square array applicators in this investigation are intended for use in hyperthermia applications, the effect of tissue attenuation on patterns predicted by simulation are of interest. Assuming a tissue attenuation factor of 0.0806 Np/cm, a single element contour plot of the field in tissue (Figs. B.21 or B.24) shows the beam pattern compared to the same situation in water (Fig. B.22 or B.23). As might be expected, the transverse symmetry of patterns is retained from the water to the tissue situation. However, the axial patterns in tissue experience a marked drop-off due to increased attenuation. This effectively brings the 3 dB contours closer to the transducer source. A similar

Table 6.3. Simulated and Experimental Results of Field Characteristics from a Block-of-4-Element Arrangement

SOURCE (Fig./Table)	SCAN TYPE	AXIAL DISTANCE z (cm)	HALF-POWER BEAMWIDTH (cm)	ERROR (%)	MAXIMUM RIPPLE AMPLITUDE (dB)	ERROR (%)
16-ESA Table 5.4	7.6	transverse	6.6	+3.1	----	----
Simulation Figure A.40	7.6	transverse	6.4		----	----
16-ESA Table 5.4	2.5 - 20.0	axial	---	----	3.5	-24
Simulation Figure A.39	5.0 - 15.0	axial	---	----	(4.6)	

effect might be expected for any of the patterns investigated in this study.

6.2. Features Useful for Hyperthermia

Several features of the multielement square array applicator make it a useful transducer source in localized hyperthermia therapy. The size, shape, and depth of a given tumor dictate the variable size and shape of the region of tissue which needs to be heated. Thus, a different set of transducer elements might be selected for each situation with a particular relative amplitude (power) level. The 3 dB beamwidths measured in this investigation for relative amplitudes of 50%, 71%, and 100% (1/4 power, 1/2 power, and full power) on adjacent elements provide insight for this purpose. The 3 dB beamwidth or contour of a more complicated arrangement of elements with varying power levels might be predicted by building from the results of two adjacent elements.

Certain intensity distribution patterns turn out to be particularly useful in hyperthermia therapy for heating solid tumors with necrotic cores. A recent paper [Pounds and Britt, 1984] describes a single ultrasonic crystal technique for generating double humped intensity patterns for such a purpose. The method involves producing the double or multiple peaked pattern by driving the crystal slightly off the resonant frequency. Similar double peaked relative dB intensity patterns were obtained in this study (e.g., Fig. B.17) with off resonant frequencies and other techniques.

An alternative way of producing such a double peaked pattern involves the phasing of a pair of adjacent elements. A set of adjacent double element simulations (Figs. A.31-36) show the effect of a 90^{o} phase shift on the field patterns in the range of interest. Though the beam patterns are fairly well collimated from individual elements, enough destructive interference takes place between the beam's two elements to produce a sharp crevice in the pattern achieving the desired double peak.

Finally, a straightforward way exists of producing such double peaked intensity patterns with a multielement array. A set of three elements in a row with the exterior element at full power while the middle element varies in relative power can achieve the desired pattern. Such a method is limited by the size of a single square element.

6.3. An Improved Model for Simulation

Discrepancies between simulated and experimentally measured field patterns from a single square transducer element suggest the possibility of an inadequate theoretical model. On the hypothesis that the square array program used for simulation oversimplifies the physical condition of a transducer element, attempts were made to more accurately model it with a more sophisticated description. Tests of the modified model were then carried by running simulations of the field patterns and looking for improvements in their agreement with experimentally measured patterns.

Individual transducer elements are divided on a single sheet of piezoelectric ceramic by only the electrode plating. Thus,

the mechanical coupling of each transducer element to surrounding elements prohibits it from vibrating independently with a perfectly uniform velocity amplitude profile. Instead, the velocity amplitude profile sags at the edges. Attempts were made to model this profile in each dimension with a cosine function to a fractional power

$$u(x) = [\cos(\pi x/50)]^{1/n} \qquad (6.1)$$

where x is a position with respect to the geometric center over the range -36 mm $< x < +36$ mm, and n is an integer ($2 \leq n \leq 10$). Plots of normalized velocity amplitude u(x) generated by Eq. (6.1) show the shape of this function for n = 2, 4, 5, and 10 (Figs. C.1-4).

The effects of such a modified model were tested by simulating the acoustic field from a single element and comparing the 3 dB half-power beamwidth and maximum ripple amplitude characteristics with the experimentally measured results. Figures C.5-8 illustrate predicted transverse scans for n = 2 and n = 10 (in Eq. (6.1)) at depths of 70 mm and 130 mm in the field. Figures C.9 and C.10 show the axial scan for a single element with n = 2 and n = 10. Figures C.11 and C.12 are the contour plots for these cases. Table 6.4 summarizes the characteristics of these simulated patterns and compares them with the corresponding experimental results. These results show that the nonlinear velocity amplitude profile of the modified model yields improved predictions for the maximum ripple amplitude of both transverse and axial scans. The 3 dB half-power beamwidth predictions are also better than those

Table 6.4. Simulated and Experimental Results of Single Element Field Characteristics with a Modified Model

SOURCE (Fig./Table)	SCAN TYPE	AXIAL DISTANCE z (cm)	HALF-POWER BEAMWIDTH (cm)	ERROR (%)	MAXIMUM RIPPLE AMPLITUDE (dB)	ERROR (%)
4-ESA (avg.) Table 5.1	TV	7.0	2.3		1.3	
Simulation (n=2) Figure C.5	TV	7.0	2.2	+ 4.5	1.0	+ 30
Simulation (n=10) Figure C.6	TV	7.0	2.7	-15	2.0	- 35
4-ESA (avg.) Table 5.1	TV	13.0	1.7		1.4	
Simulation (n=2) Figure C.7	TV	13.0	1.8	- 5.6	0.5	+180
Simulation (n=10) Figure C.8	TV	13.0	2.3	-26	2.9	- 17
16-ESA (#10)	AX	2.5-20.0	---		2.3	
Simulation (n=2) Figure C.9	AX	5.0-15.0	---	---	1.9	+ 21
Simulation (n=10) Figure C.10	AX	5.0-15.0	---	---	5.3	- 57

predicted with a uniform velocity amplitude profile. Maximum ripple amplitude data suggests, that for the nonlinear velocity amplitude profile generated by Eq. (6.1), the best value of n lies between n = 2 and n = 10 to make the best predictions. Thus, the modal including mechanical damping of transducer elements appears to be an improvement over the simplified model which assumes a uniform velocity distribution.

CHAPTER 7

CONCLUSIONS AND SUGGESTIONS FOR FURTHER STUDY

Characterizations of the acoustic fields from an ultrasonic square array applicator carried out in this study show the advantages of a multielement transducer compared to a single unfocused one for use in hyperthermia therapy. Experimentally measured transverse scans at two depths in the treatment region identify the 3 dB half-power beamwidth for single and multiple element transducer patterns. Results show that the 3 dB beamwidth can be altered by adjacent element power variations. Thus, acoustic power deposition from a multielement transducer can be accommodated to the size of the tumor.

A double-humped intensity pattern is useful in hyperthermia therapy for treating cancer tumors with necrotic cores. Of the various possible methods to produce this pattern, a linear multiple element transducer arrangement with power variations appears to be the simplest, although the large separation between the peaks is determined by the width of an element. This method has the flexibility of adjusting the depth of the crevice (intensity minimum between peaks) by directly varying the power to the middle element(s). To produce a double-humped intensity pattern with a narrow crevice (small distance between peaks) a single transducer element can be driven with an off-resonance frequency. The frequency variation method, however, may be difficult to implement. Further investigation of this method is

necessary to determine the frequency dependent effects of ripple amplitude, 3 dB beamwidth, and crevice width.

Phase variation between adjacent elements represents a third alternative to produce the double-humped intensity pattern. Although a 90^{o} phase difference between elements effectively produces a sharp crevice, the average ripple amplitude across the beam also increases. Large ripple amplitude limits the advantage of this method for hyperthermia treatment. Further investigation of the effects of beam parameters as a function of phase difference could give a more complete picture of the profitability of this technique.

The characteristics of axial patterns from the multielement square array transducer need further experimental work. Improvements in the scanner system are necessary in order to make these measurements. Experimental axial scans could show the effects of variables such as relative amplitude, frequency, phase, and power on the ripple amplitude in the treatment region. Control of the axial ripple amplitude in the treatment region is important in order to maintain a uniform temperature distribution during hyperthermia therapy.

For this study, simulations of the intensity patterns from square transducer elements were made using a simplified model. However, results of simulations made with an improved model, taking into account the mechanical damping of transducer elements at the edges, show better agreement with the experimental measurements. Thus, future work should be done using the improved model for simulations.

All the measurements in this study were made at low power (< 1 Watt) levels. Although low power level measurements give a good initial prediction of field characteristics from the multielement transducer applicator, investigations of beam patterns at increased power levels required in actual hyperthermia treatment would reveal any thermally-induced changes or other nonlinear effects. A high power acoustic receiver would be required to handle these measurements. High power level measurements from the multielement transducer applicator represent the most important area for future work to insure accurate predictability of beam patterns and safe delivery of heat for hyperthermia therapy.

APPENDIX A

SIMULATED RESULTS

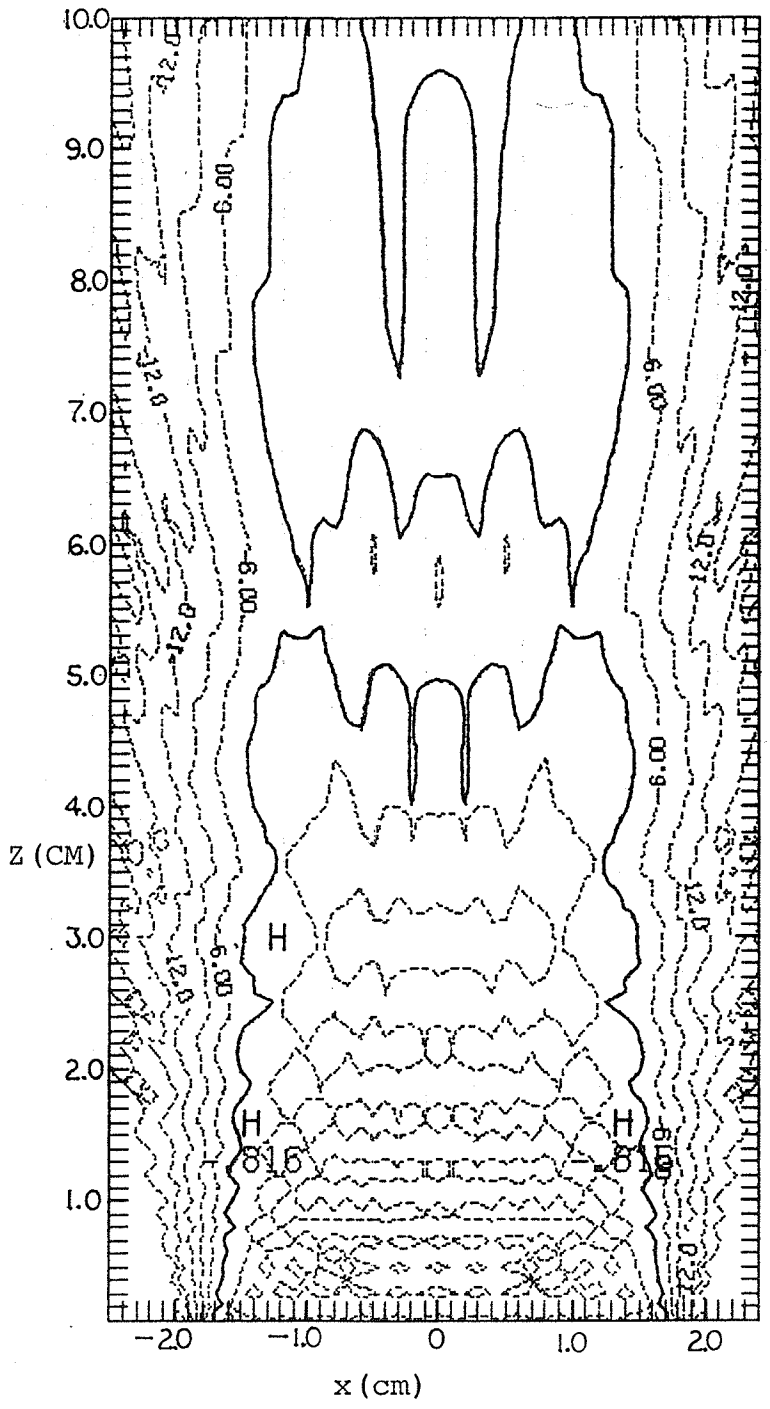

Figure A.1. Simulated 3 dB intensity contours from a single transducer element.

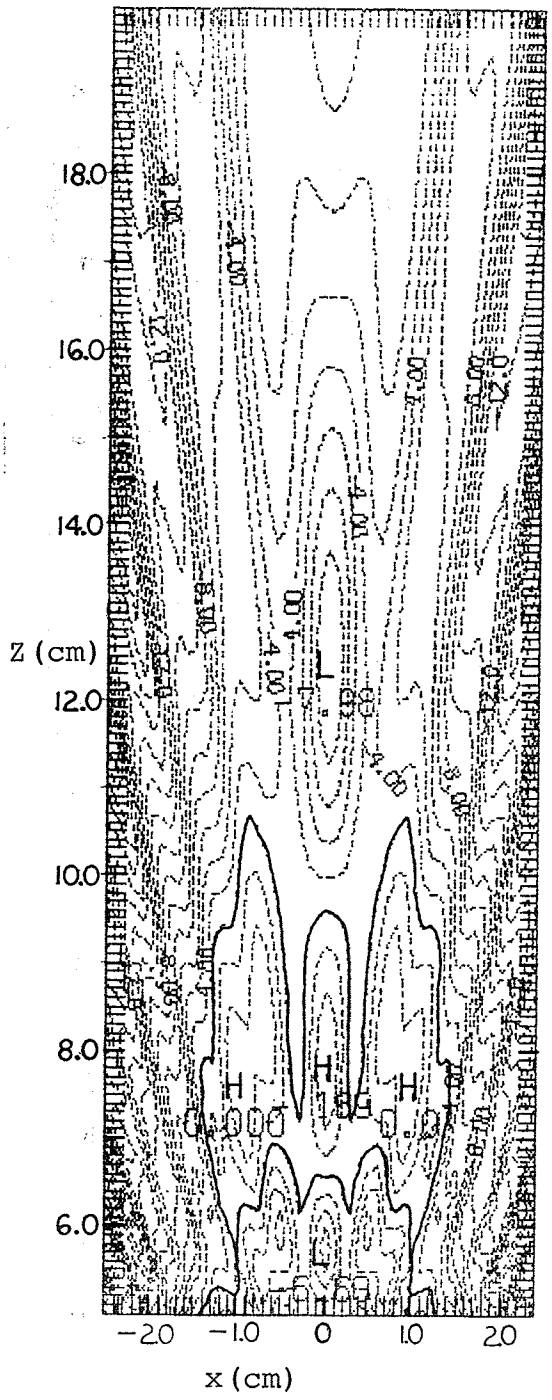

Figure A.2. Simulated 1 dB intensity contours covering the treatment range from a single transducer element.

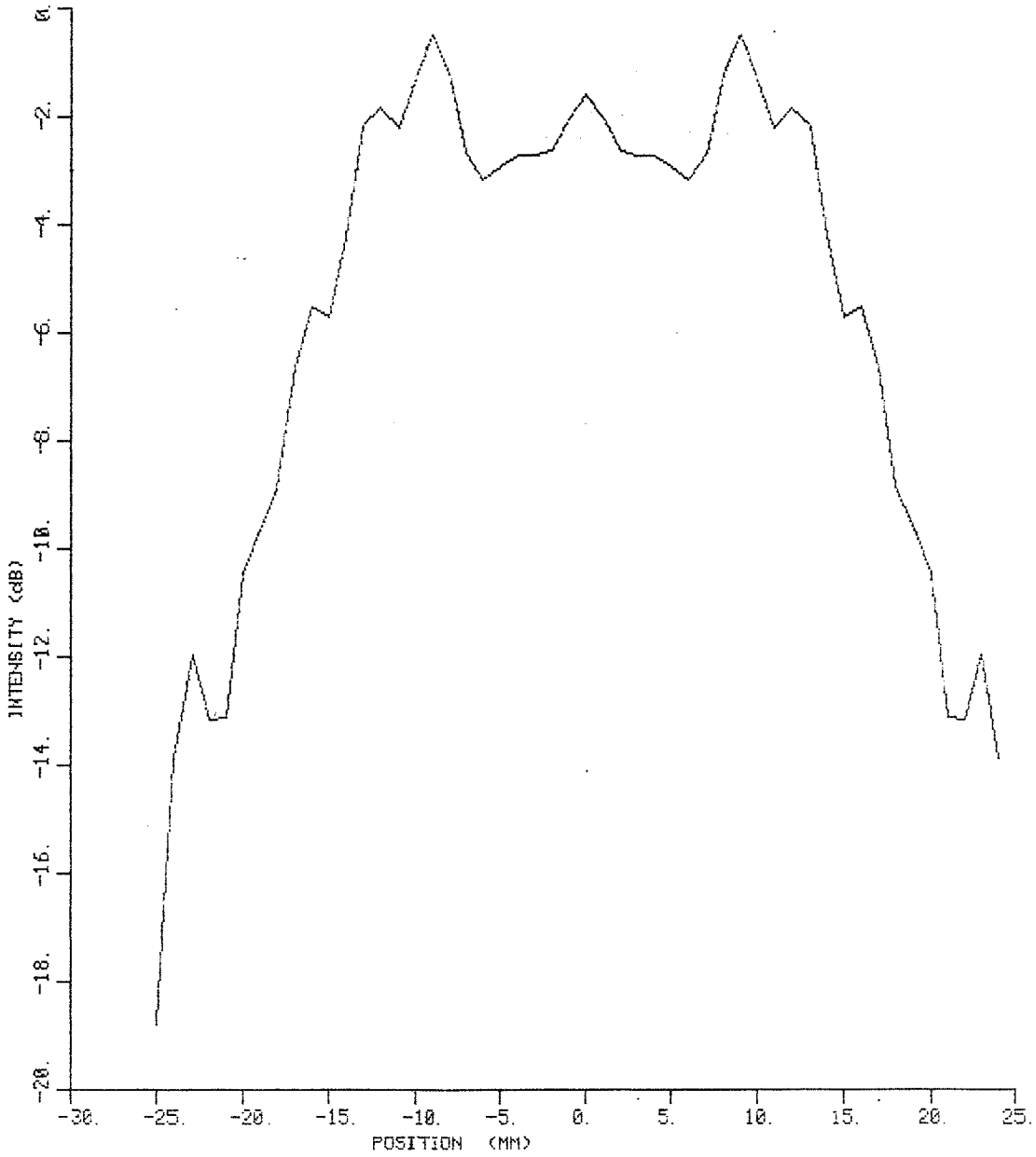

Figure A.3. Simulated transverse relative intensity profile at z = 7.0 cm from a single element.

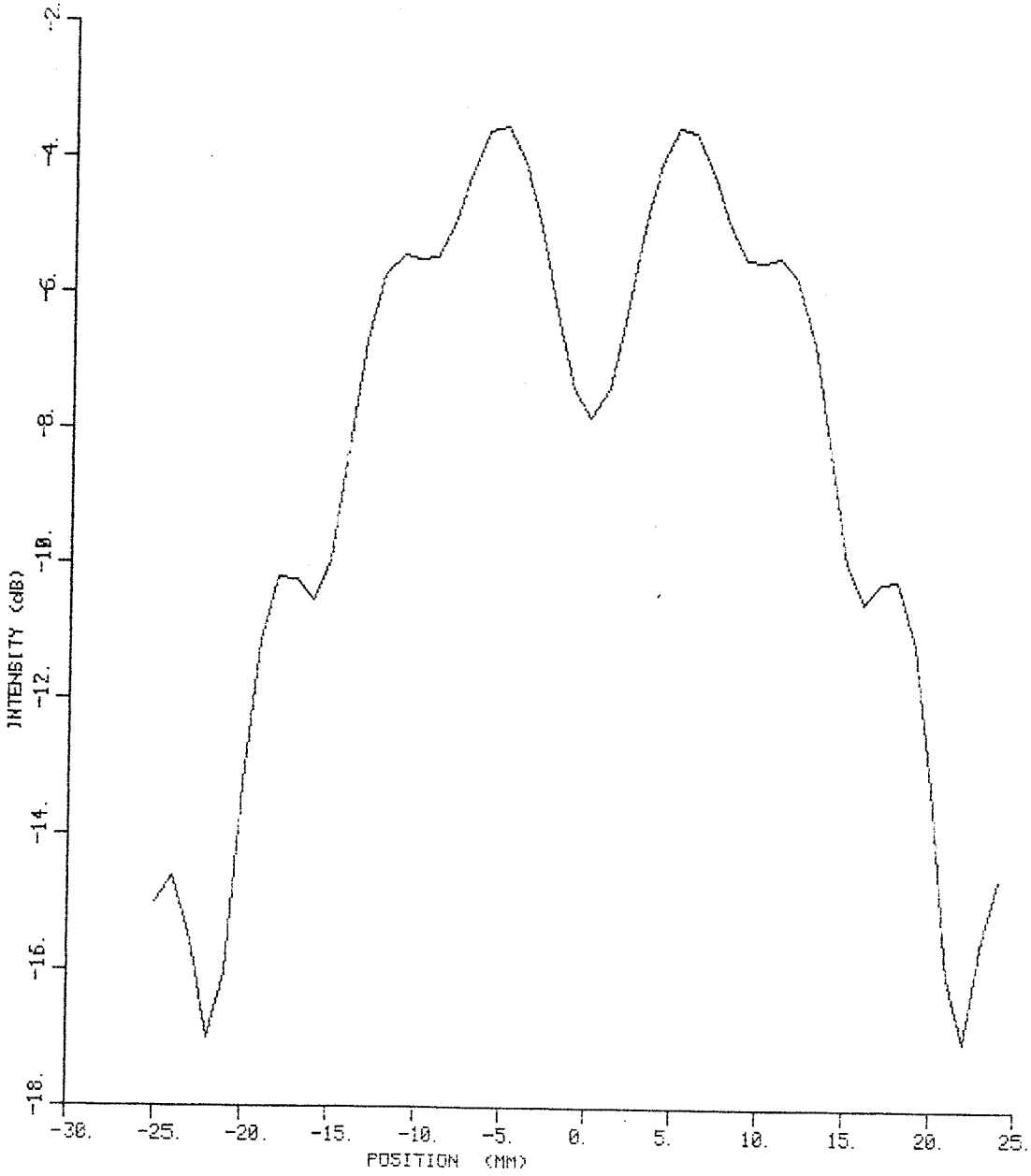

Figure A.4. Simulated transverse relative intensity profile at z = 13.0 cm from a single element.

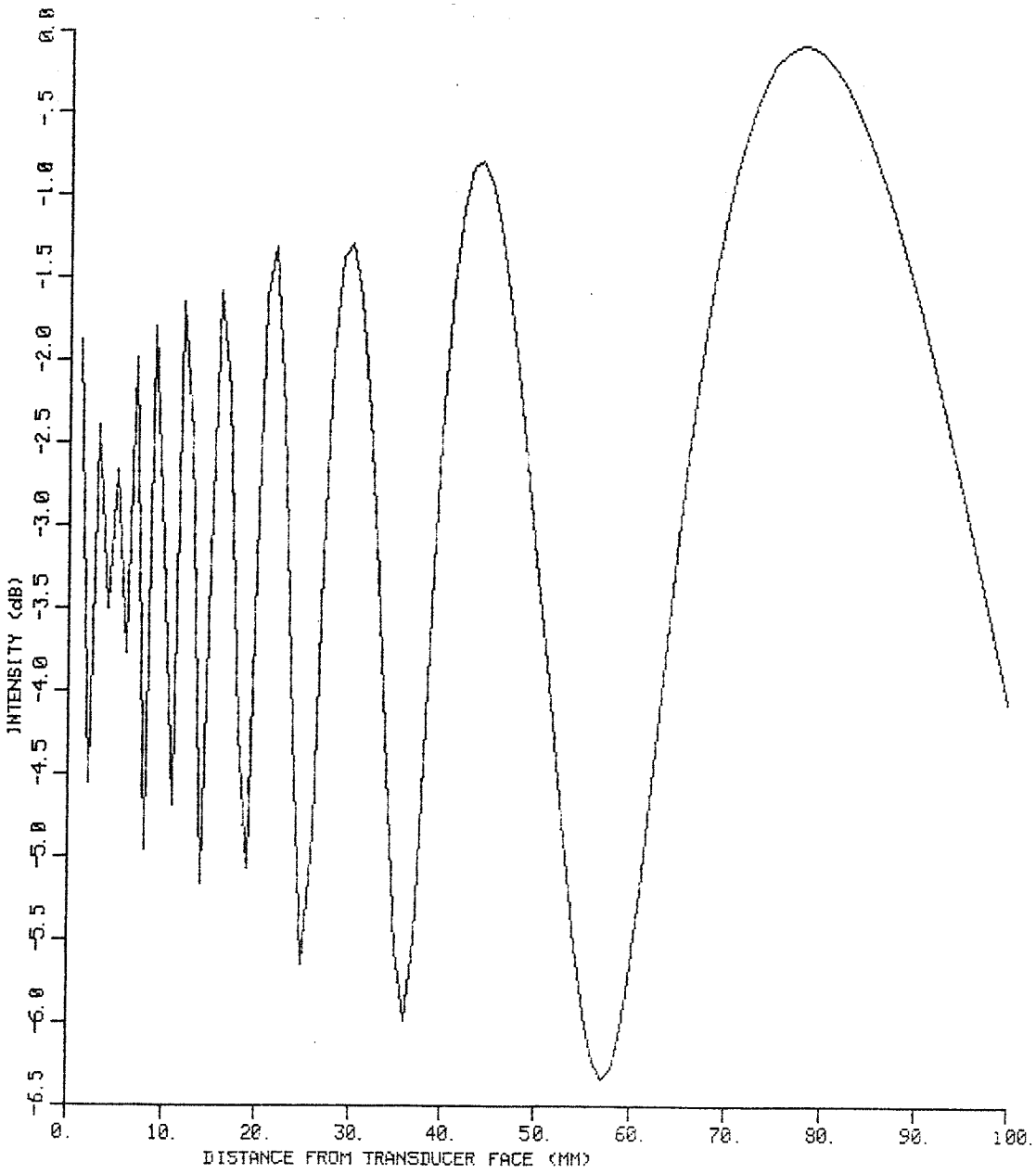

Figure A.5. Simulated axial relative intensity from a single transducer element.

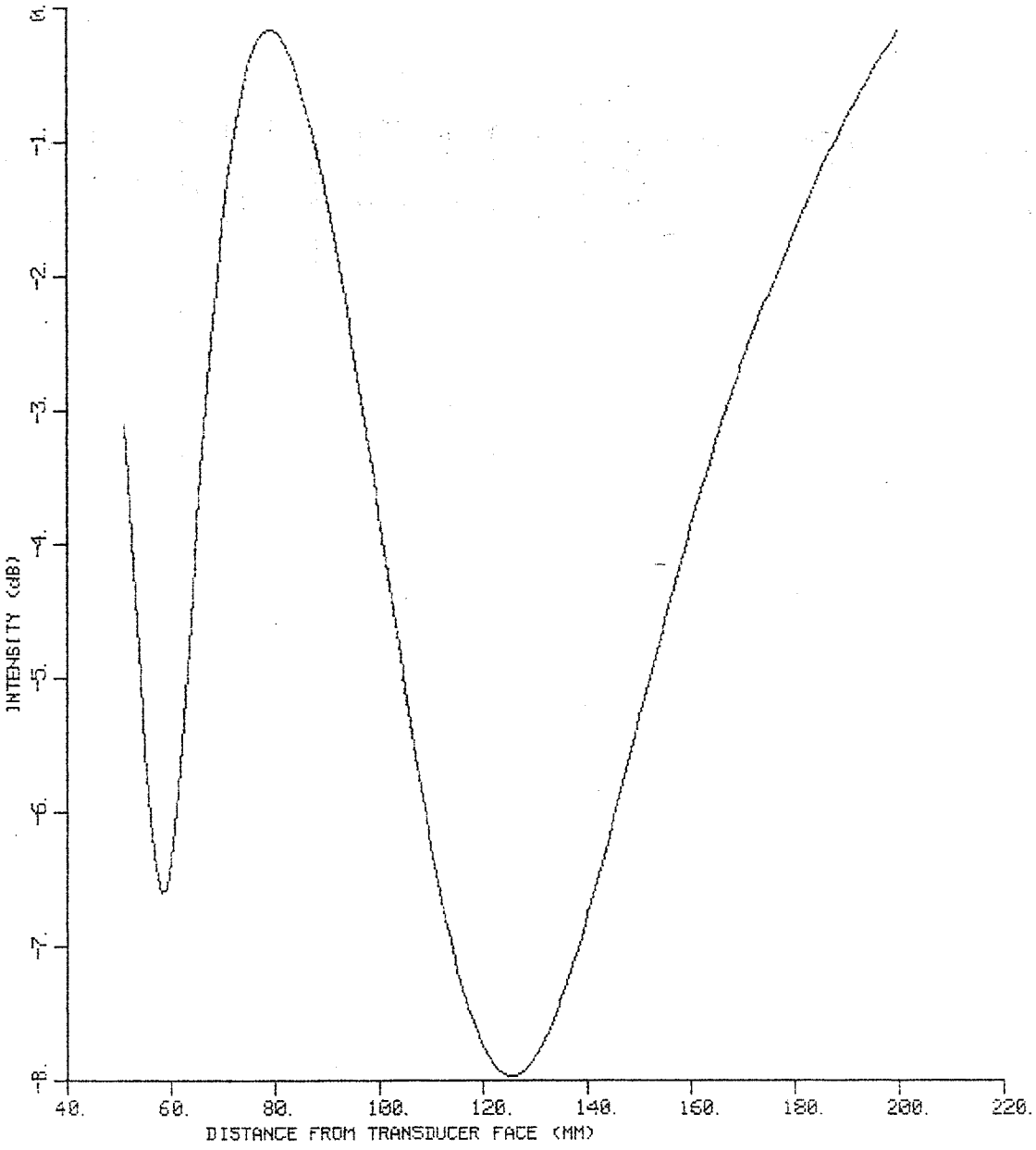

Figure A.6. Simulated axial relative intensity in the treatment range from a single element.

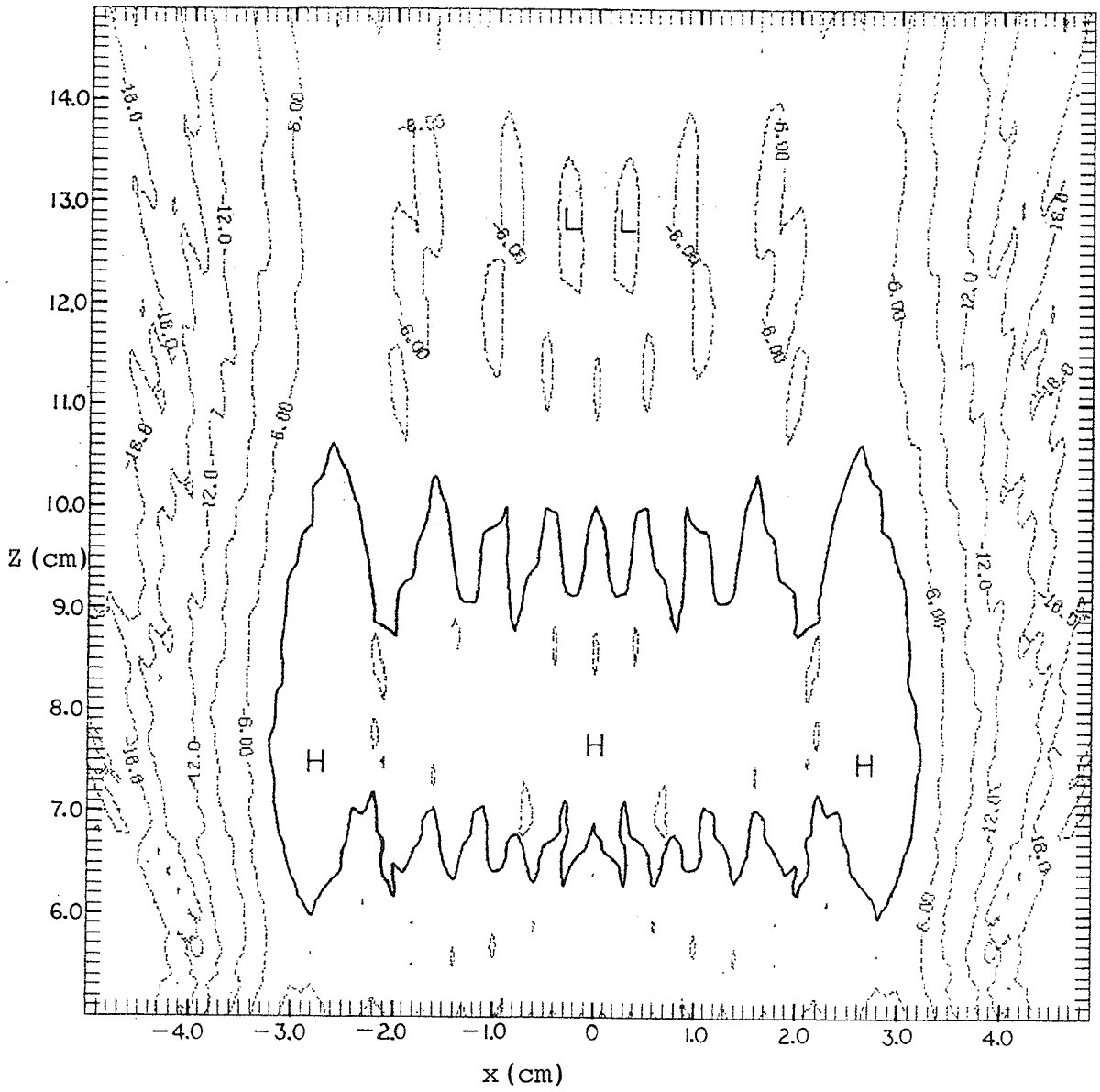

Figure A.7. Simulated 3 dB intensity contours from a pair of adjacent elements at equal power.

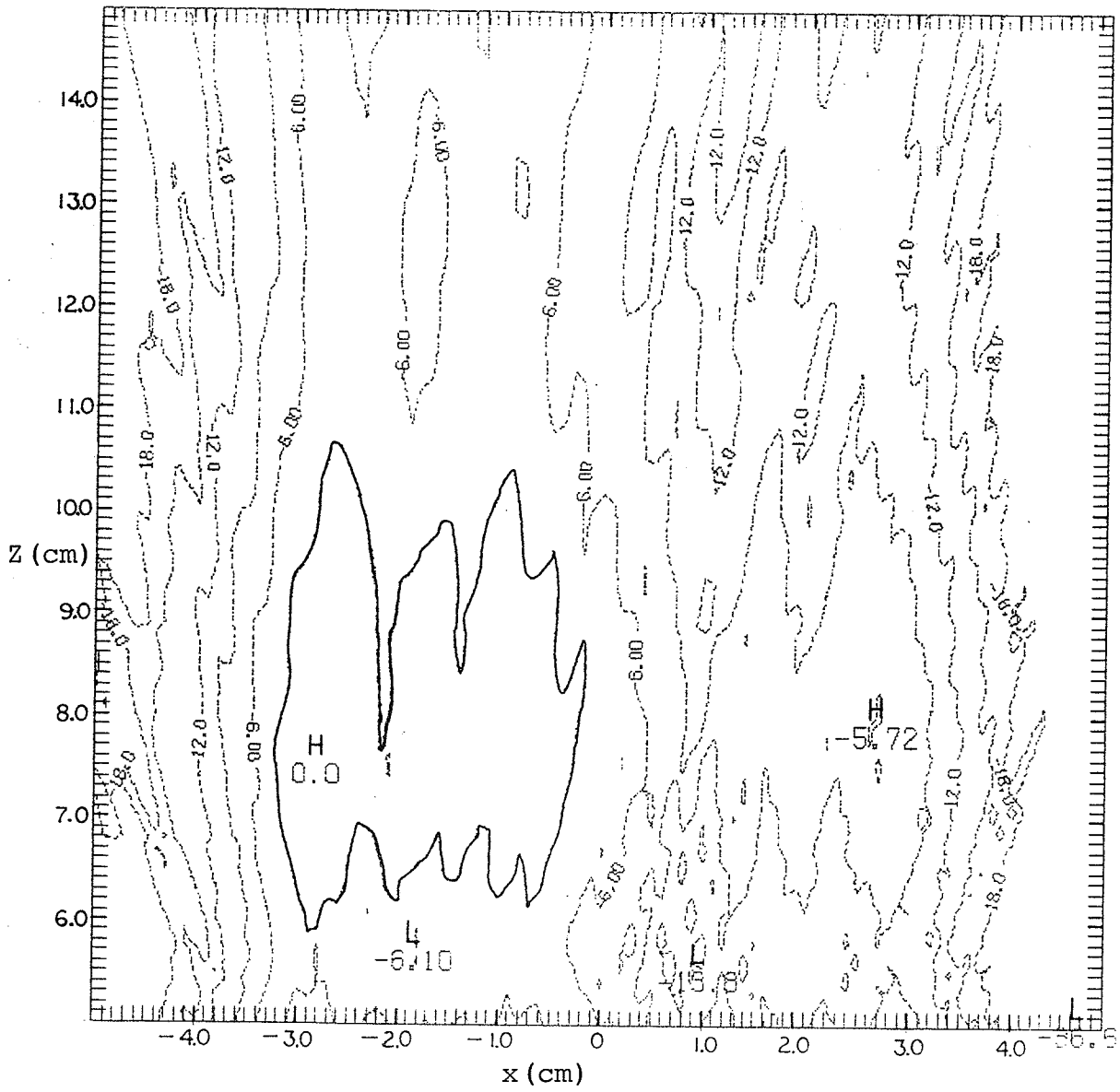

Figure A.8. Simulated 3 dB intensity contours from a pair of adjacent elements with a half power ratio.

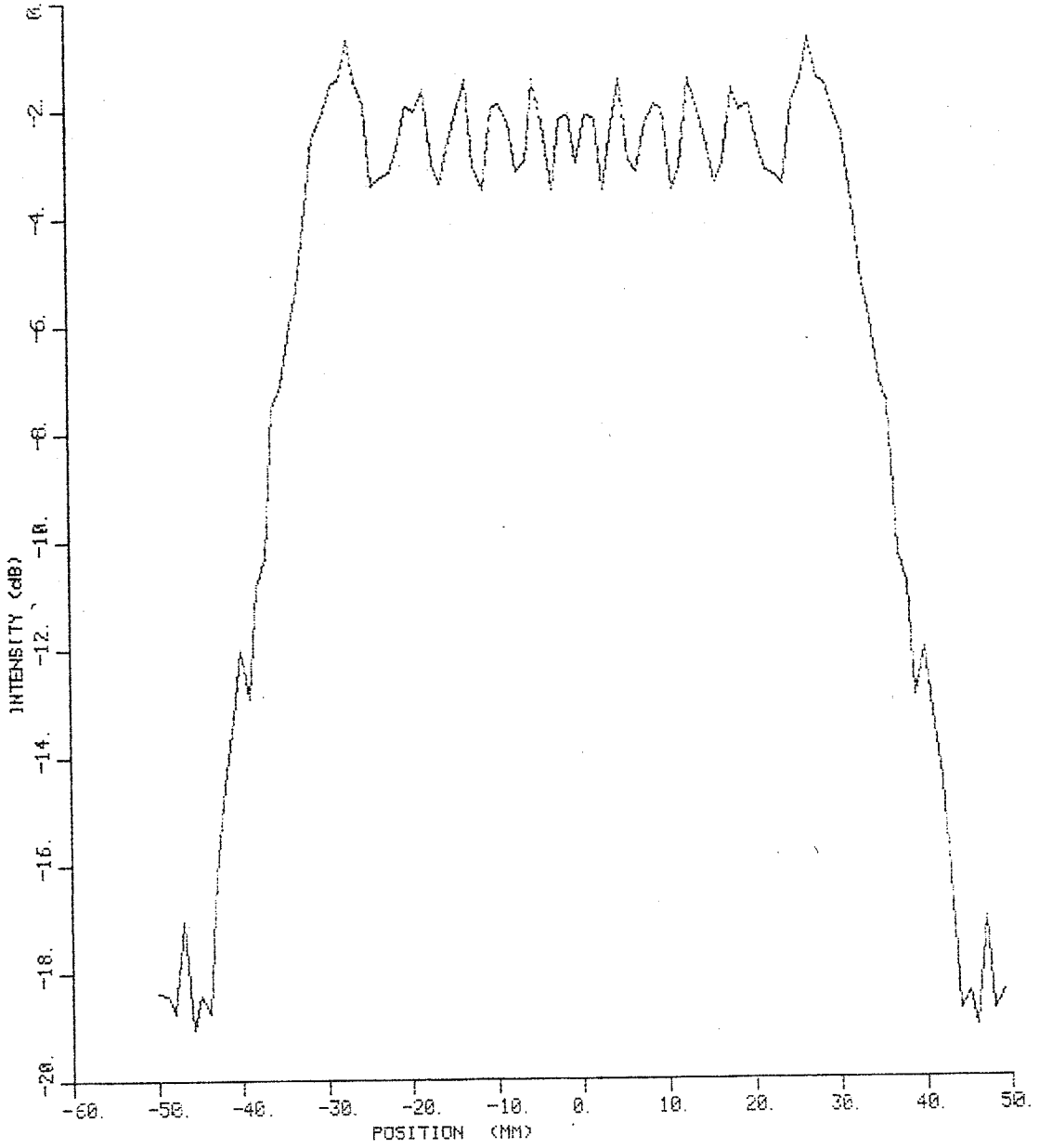

Figure A.9. Simulated transverse relative intensity profile at z = 7.0 cm from a pair of adjacent elements at equal power.

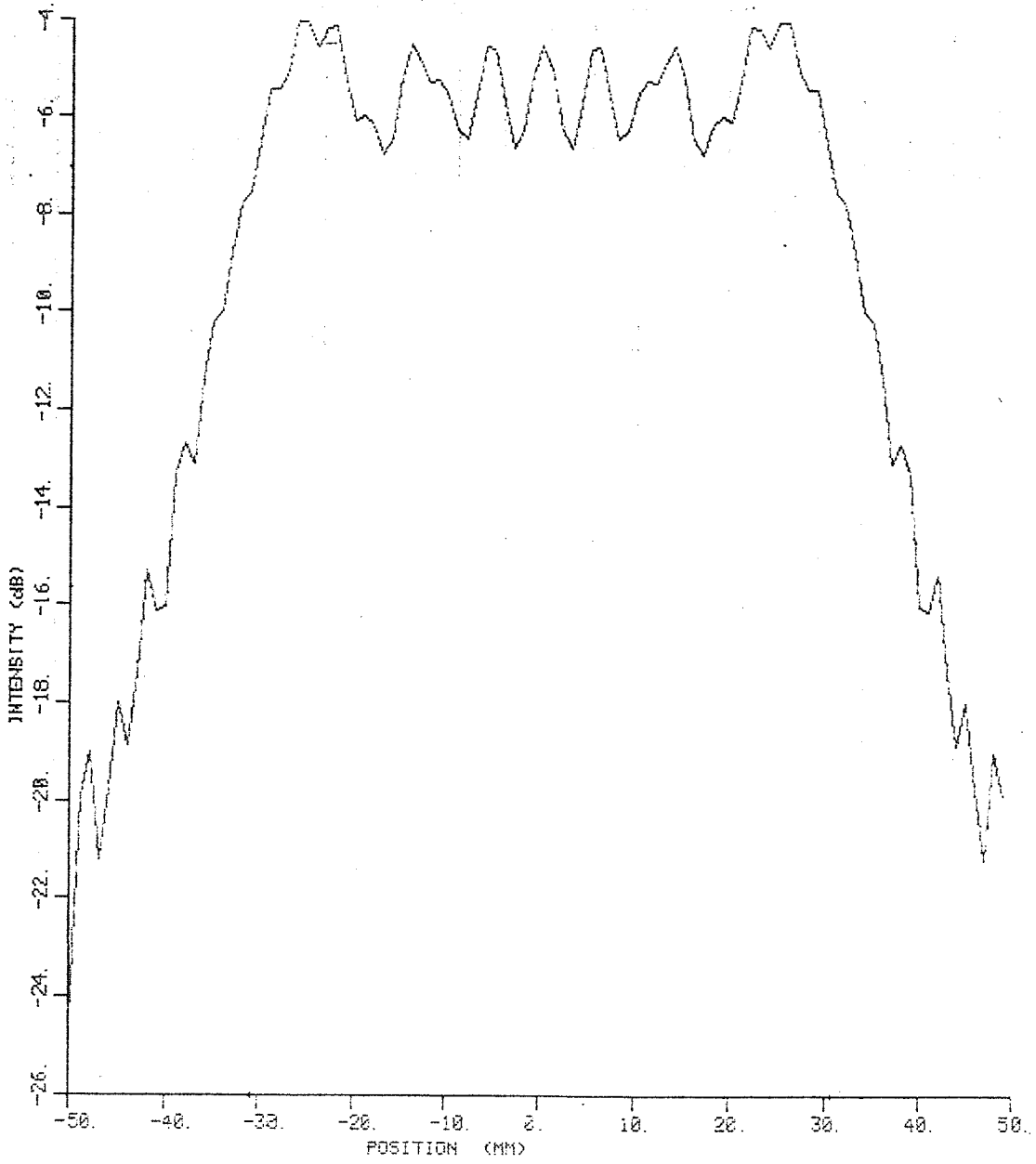

Figure A.10. Simulated transverse relative intensity profile at z = 13.0 cm from a pair of adjacent elements at equal power.

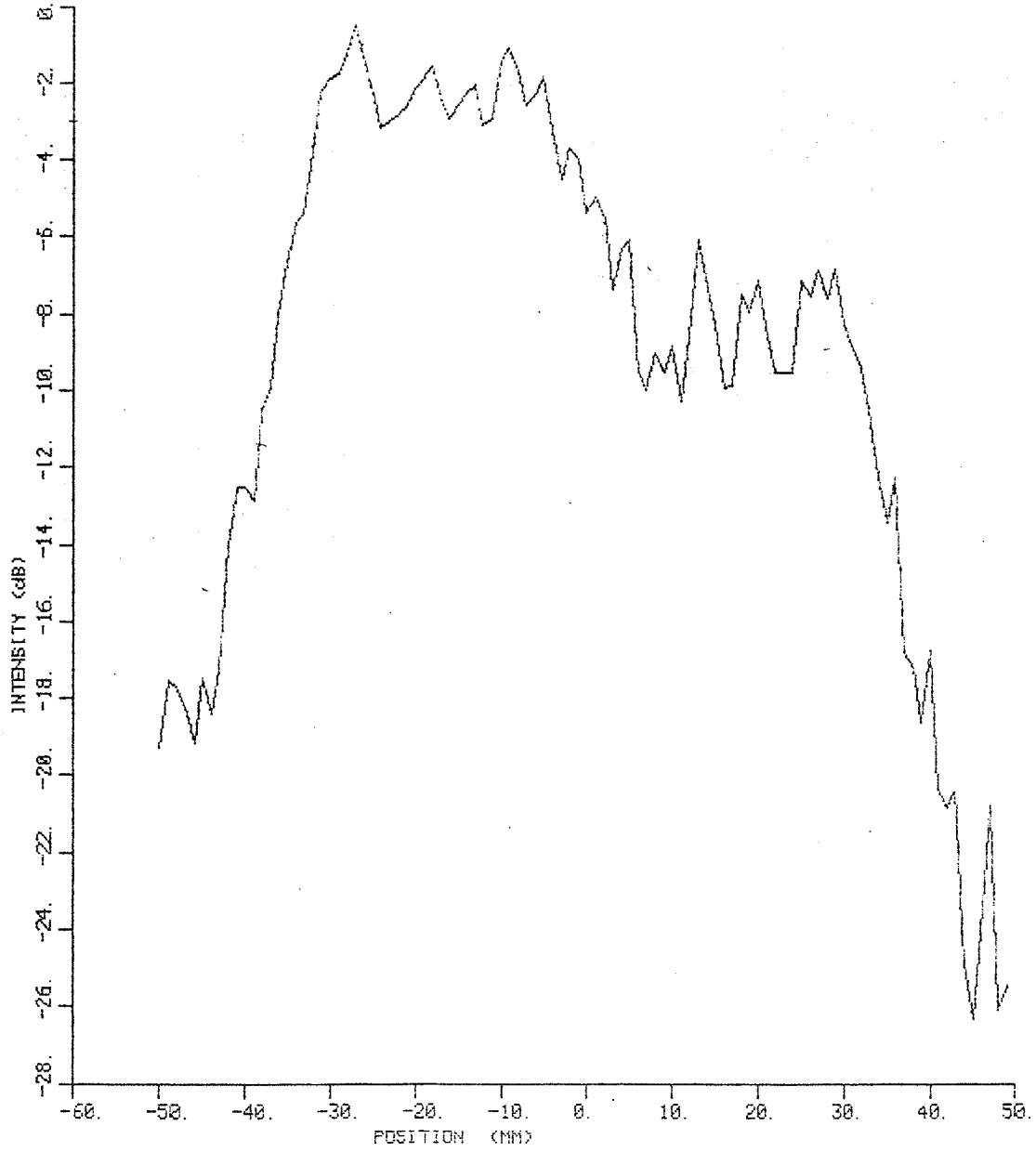

Figure A.11. Simulated transverse relative intensity profile at z = 7.0 cm from a pair of adjacent elements with one element at one-fourth power.

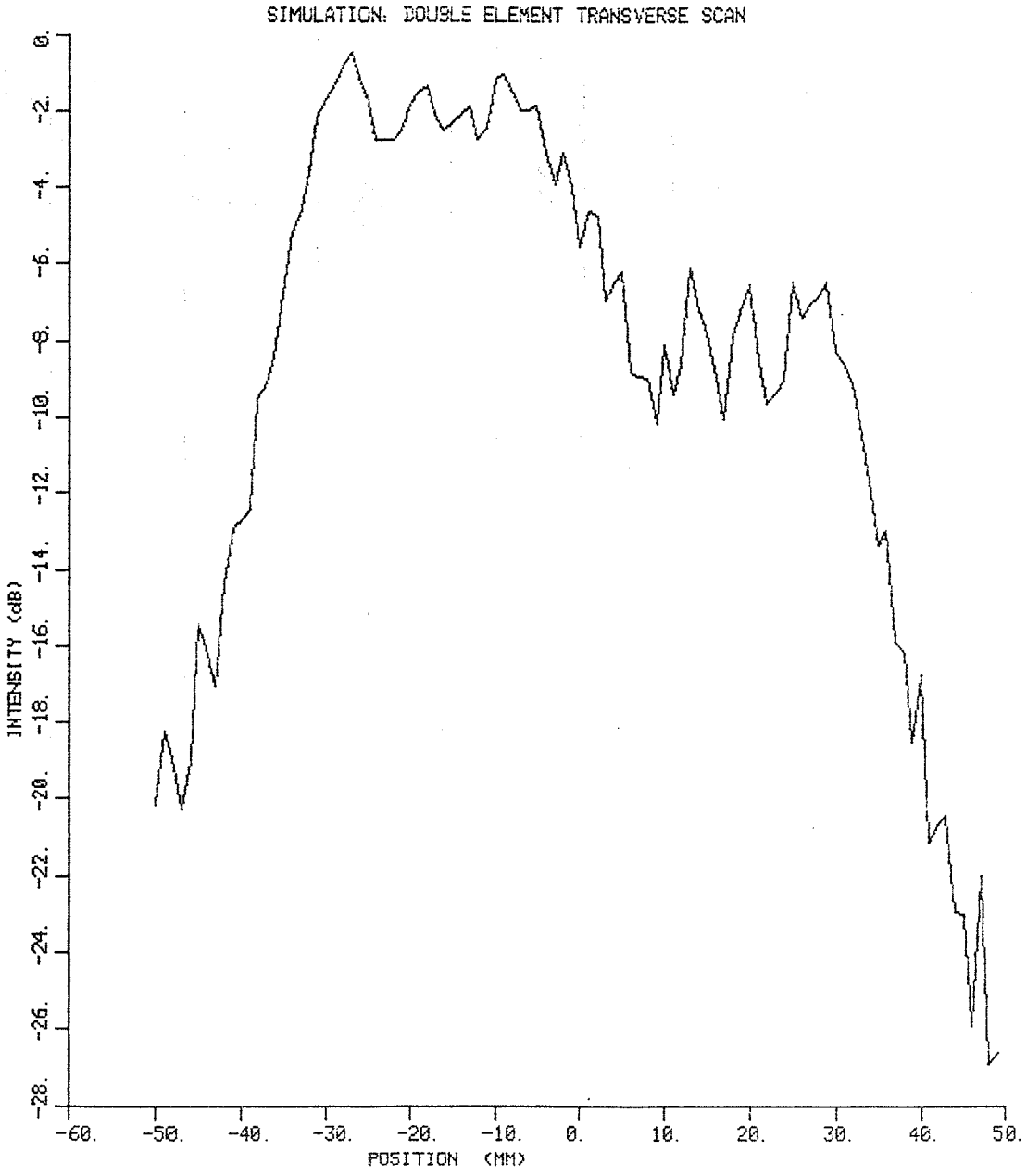

Figure A.12. Simulated transverse relative intensity profile at z = 7.0 cm from a pair of adjacent elements with one element at one-fourth power and an adjusted for field parameter.

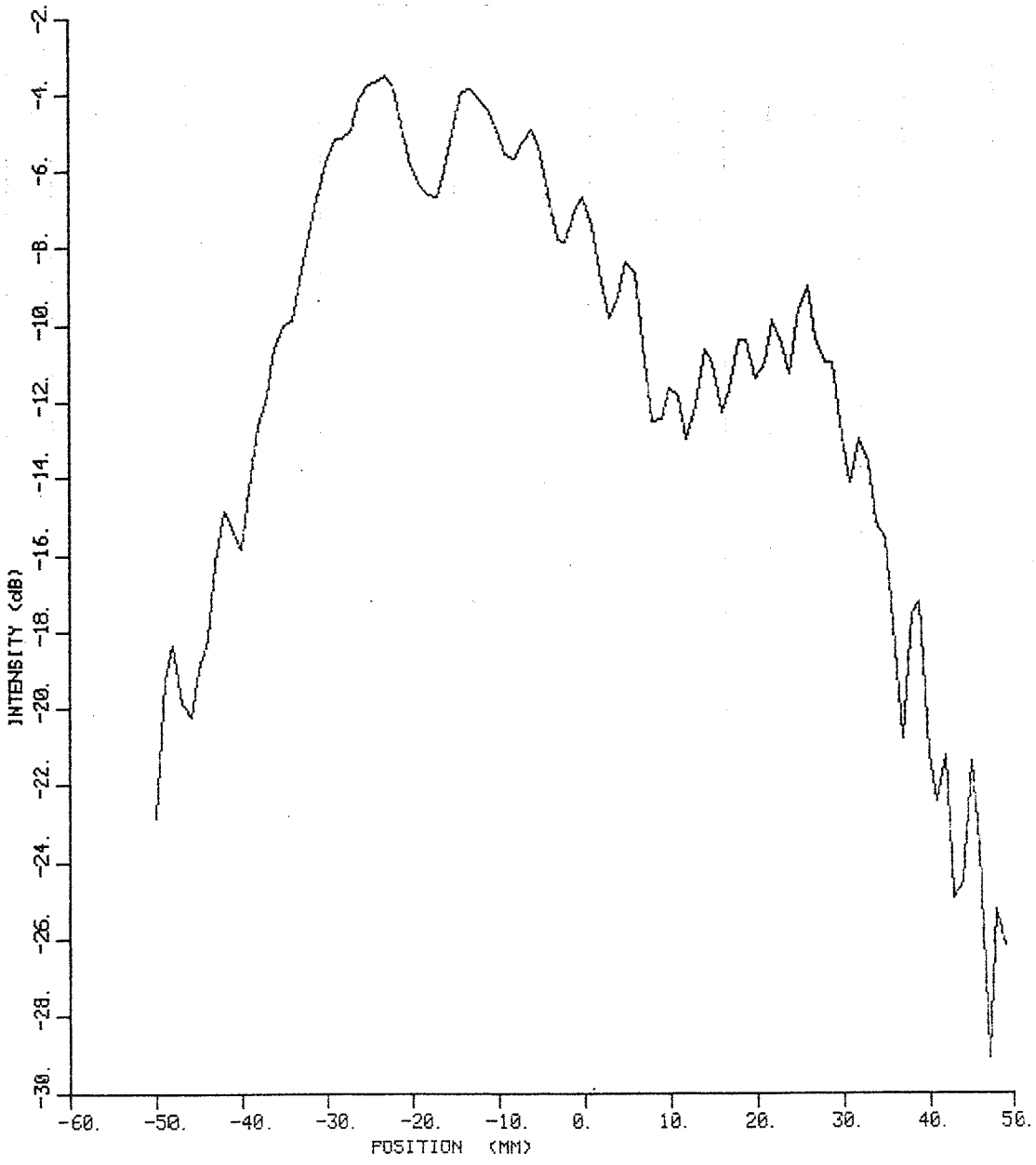

Figure A.13. Simulated transverse relative intensity profile at z = 13.0 cm from a pair of adjacent one element at one-fourth power.

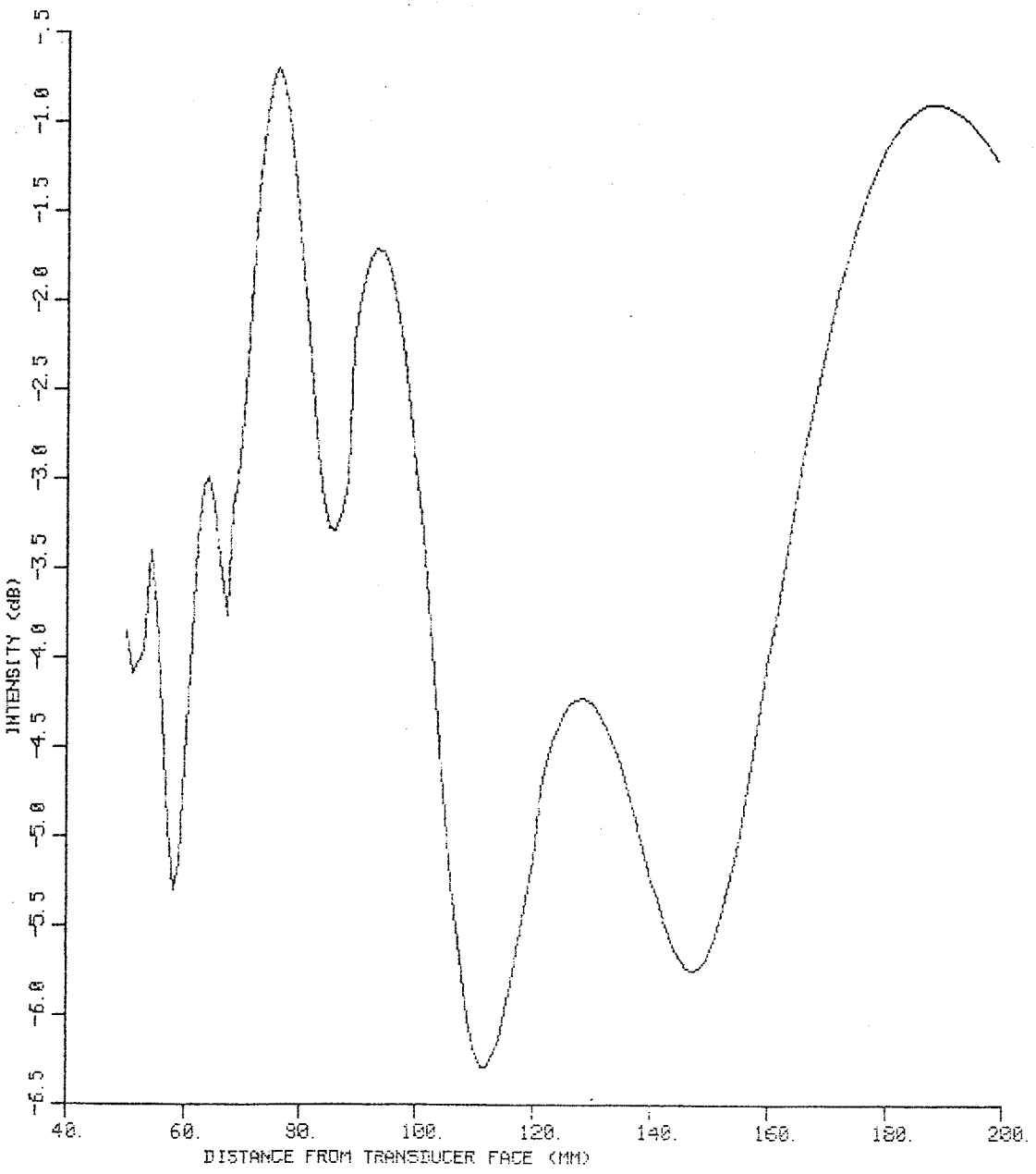

Figure A.14. Simulated axial relative intensity from a pair of adjacent elements at equal power.

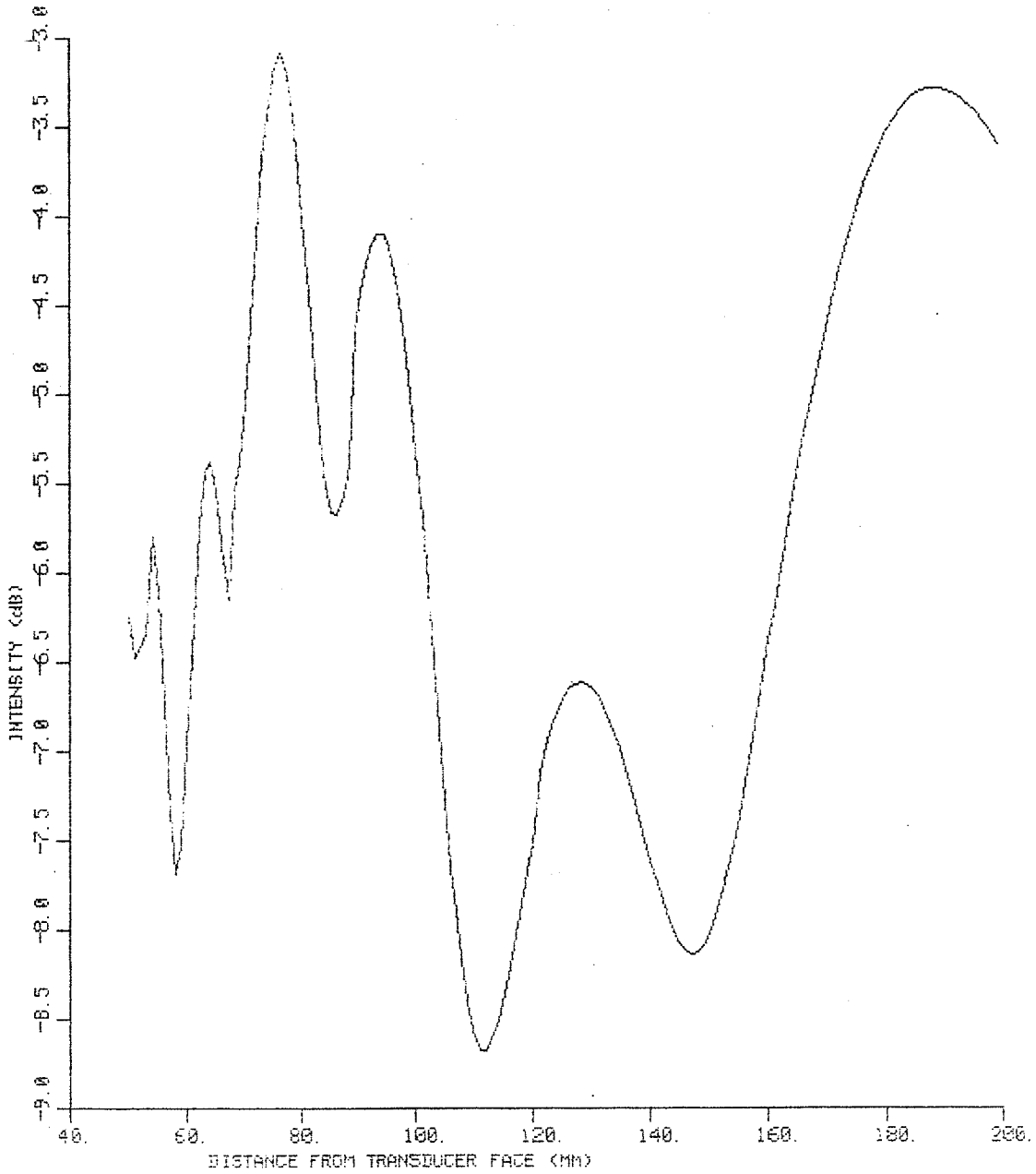

Figure A.15. Simulated axial relative intensity from a pair of adjacent elements with one element at one-fourth power.

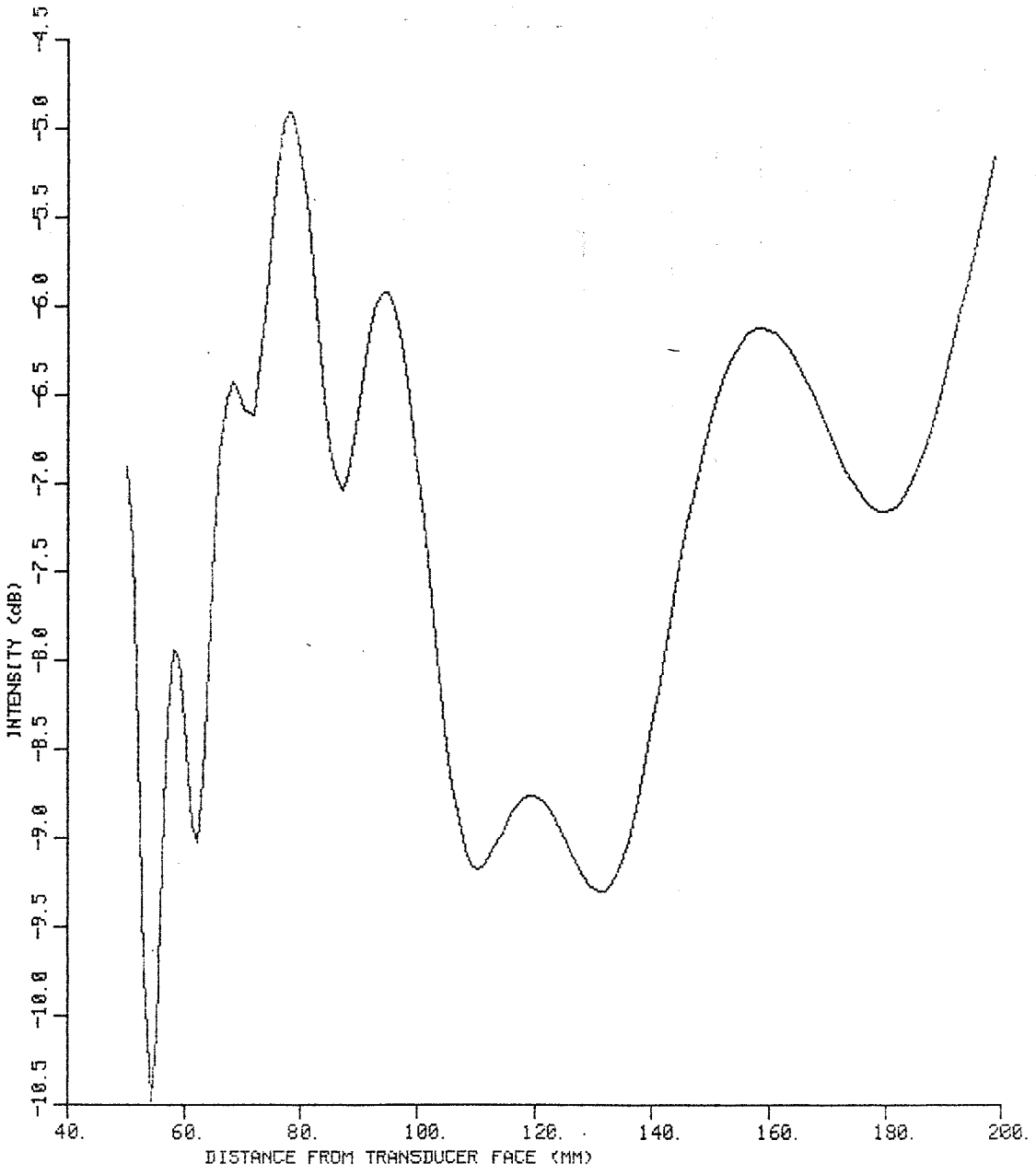

Figure A.16. Simulated offset axial relative intensity from a pair of adjacent elements with one element at one-fourth power.

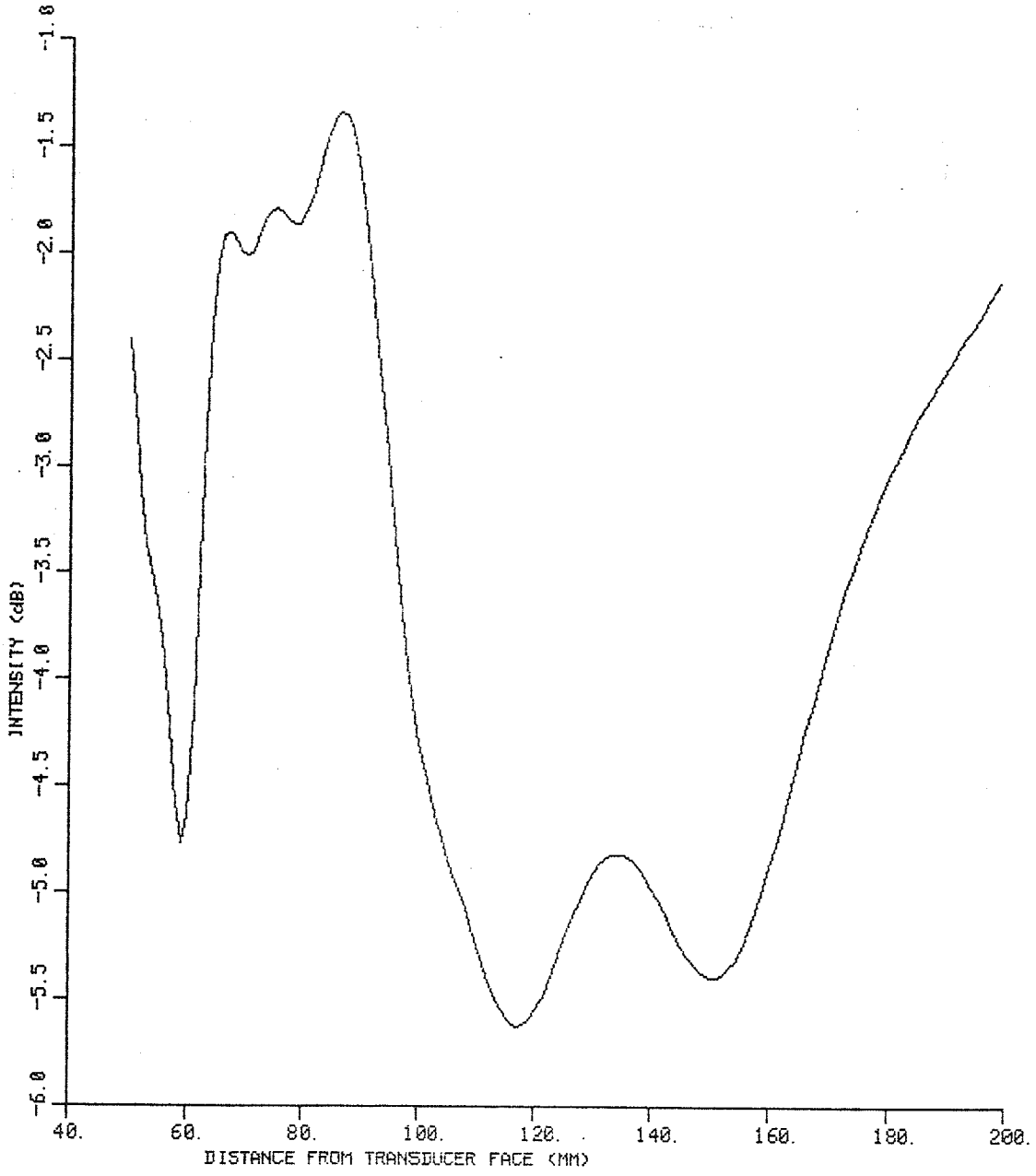

Figure A.17. Simulated offset axial relative intensity from a pair of adjacent elements with one element at one-fourth power.

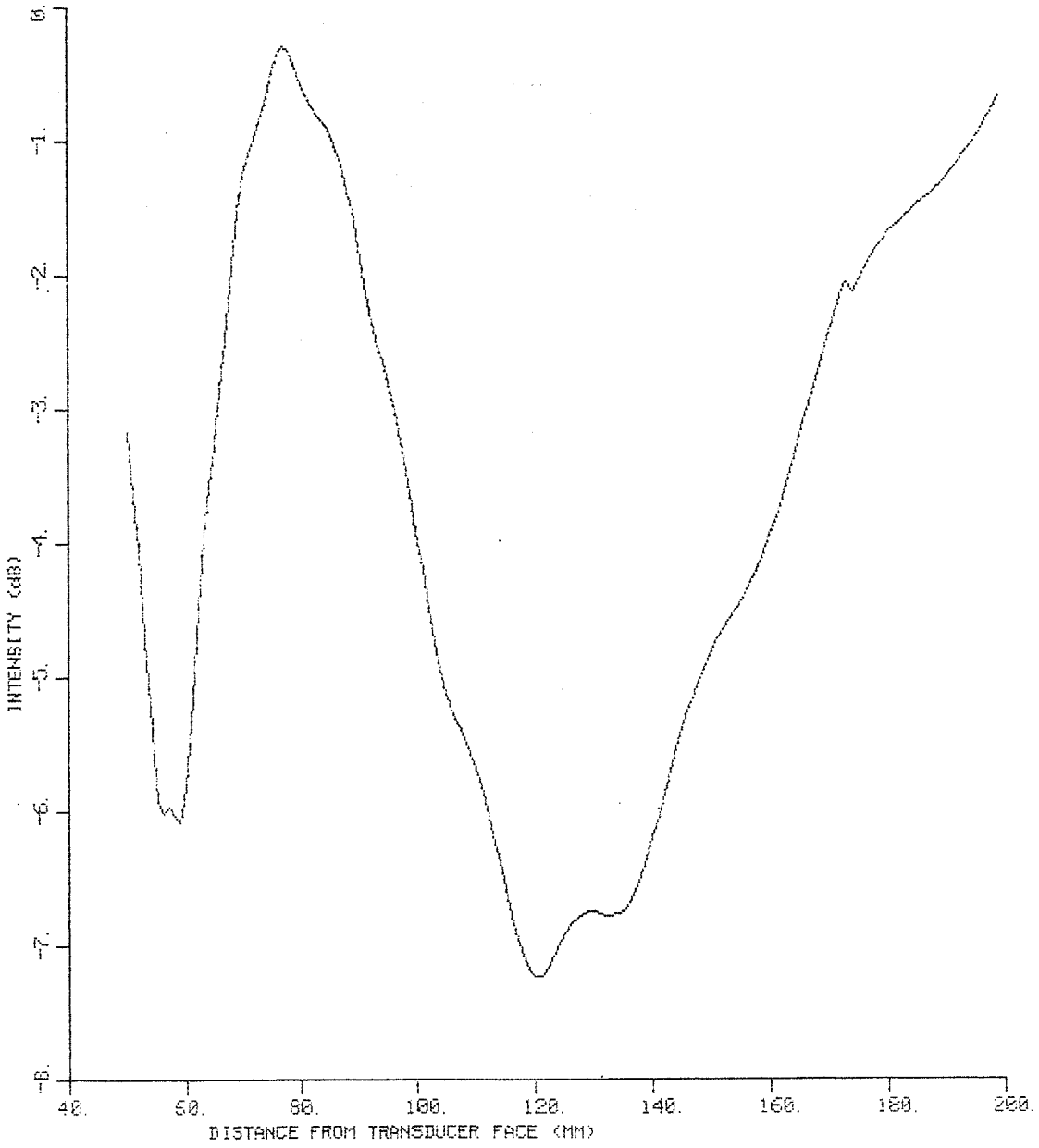

Figure A.18. Simulated offset axial relative intensity from a pair of adjacent elements with one element at one-fourth power.

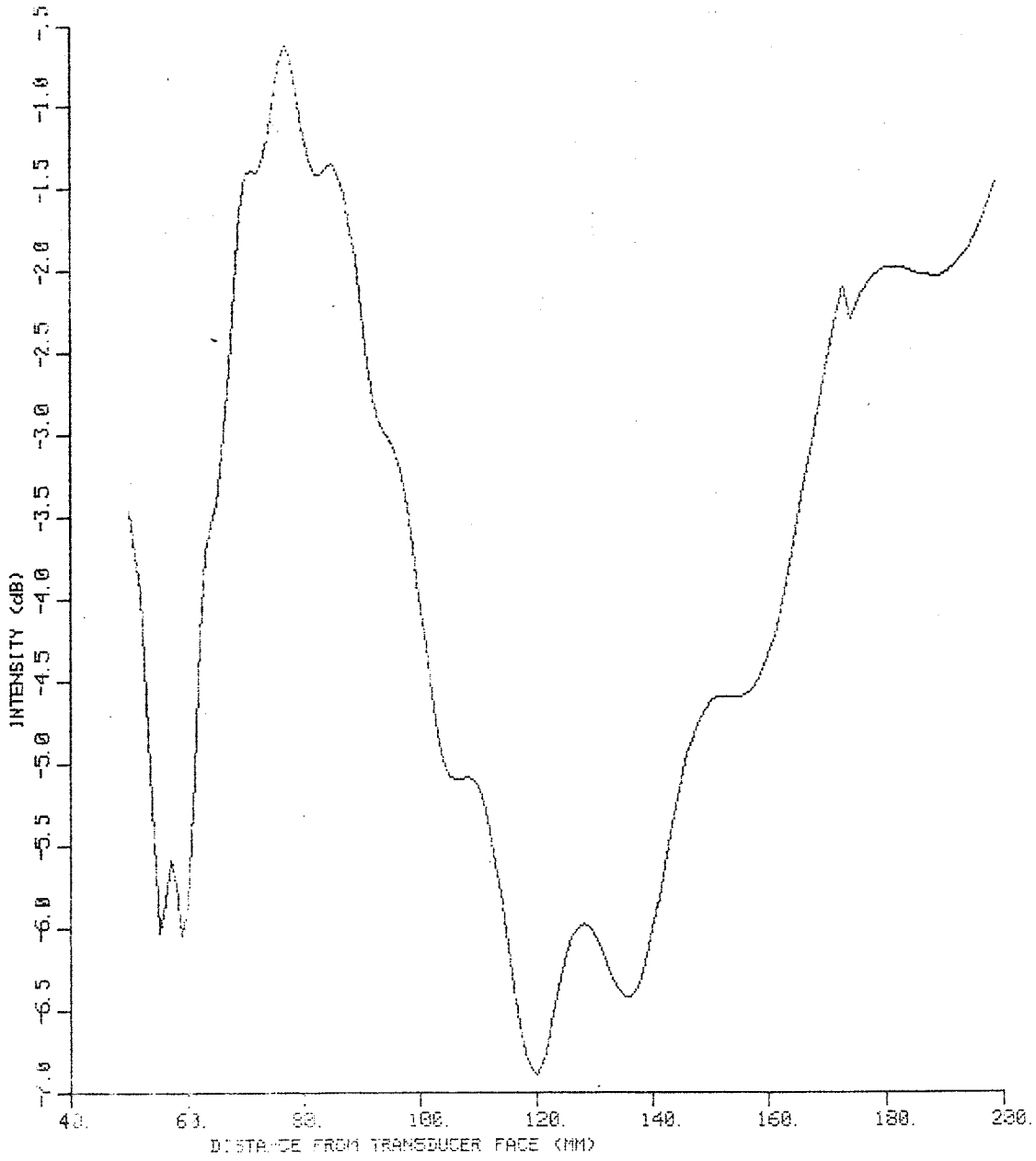

Figure A.19. Simulated offset axial relative intensity from a pair of adjacent elements with one element at one-fourth power.

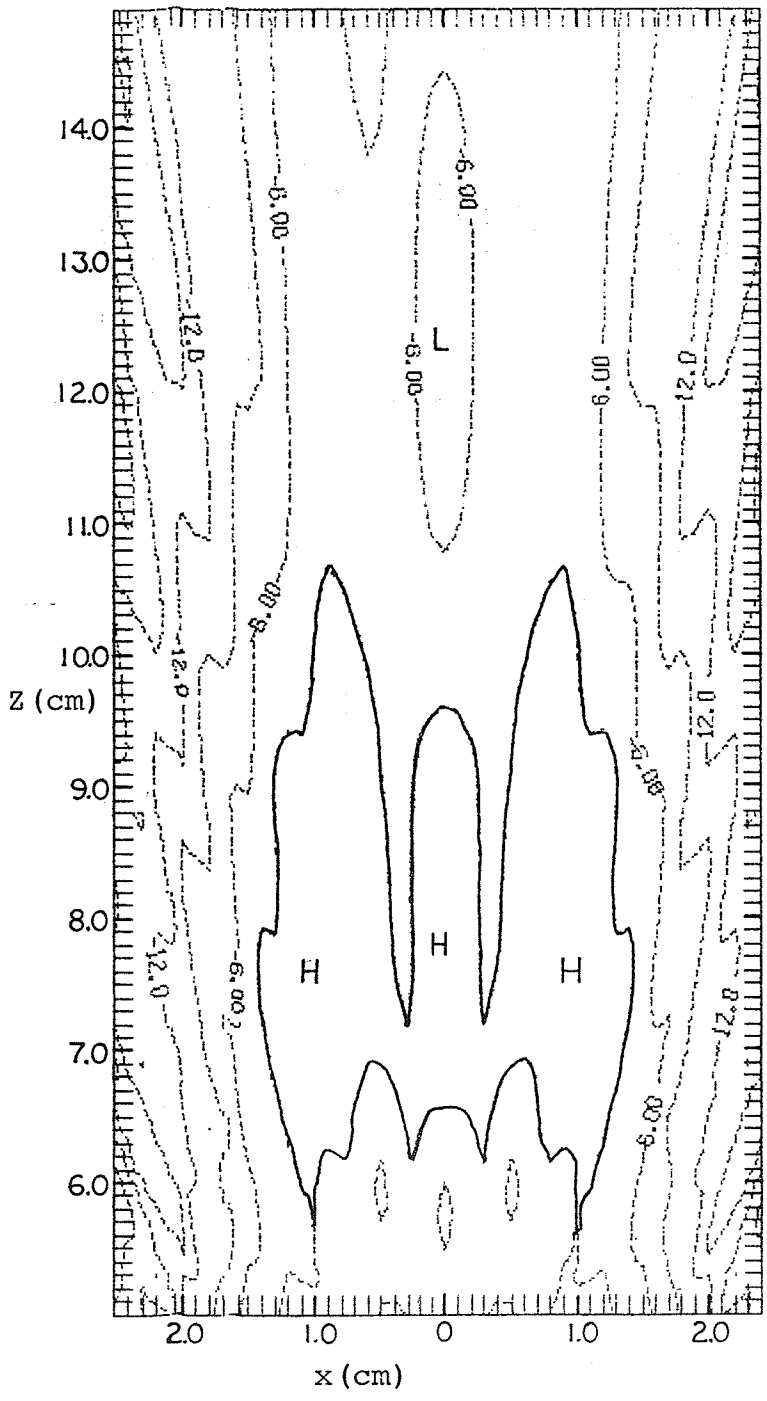

Figure A.20. Simulated 3 dB intensity contours from a single element.

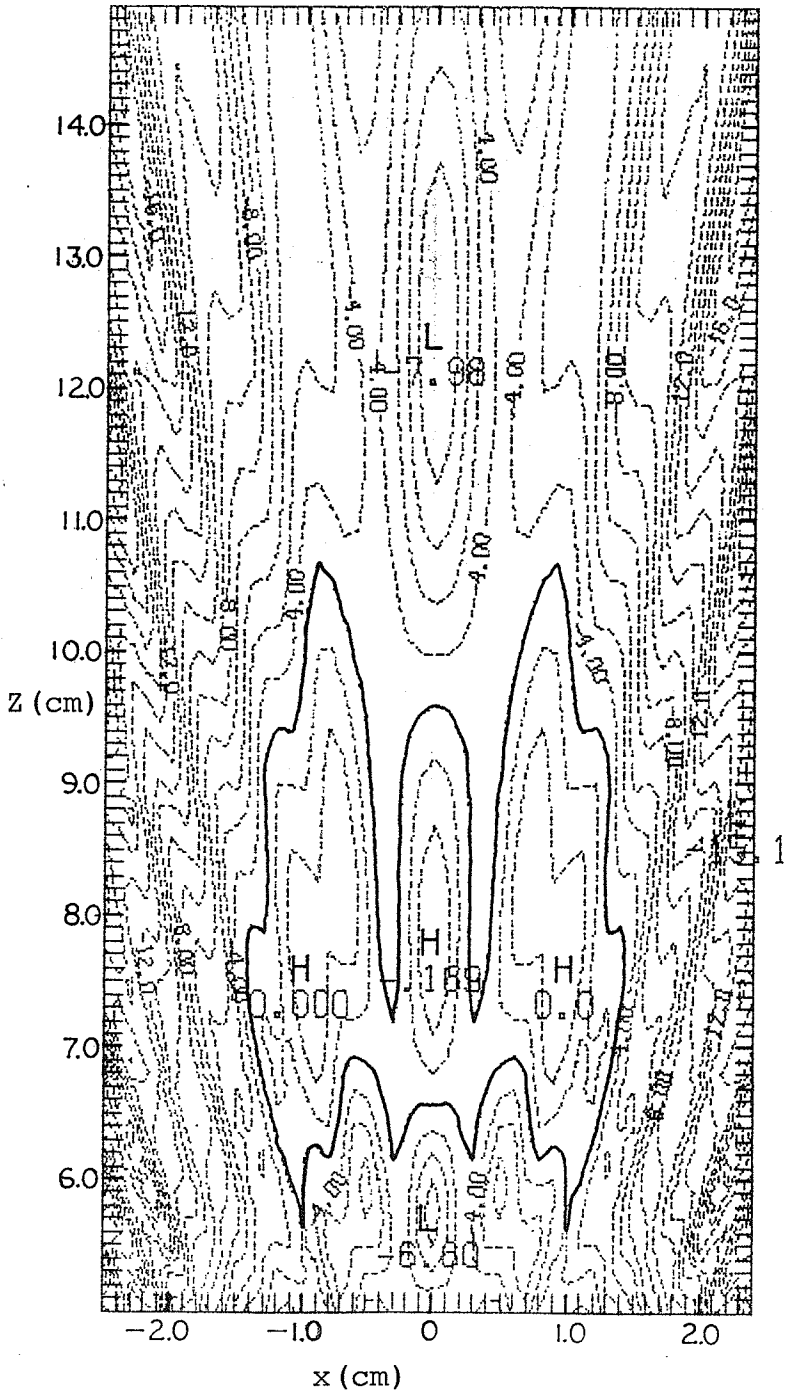

Figure A.21. Simulated 1 dB intensity contours from a single element.

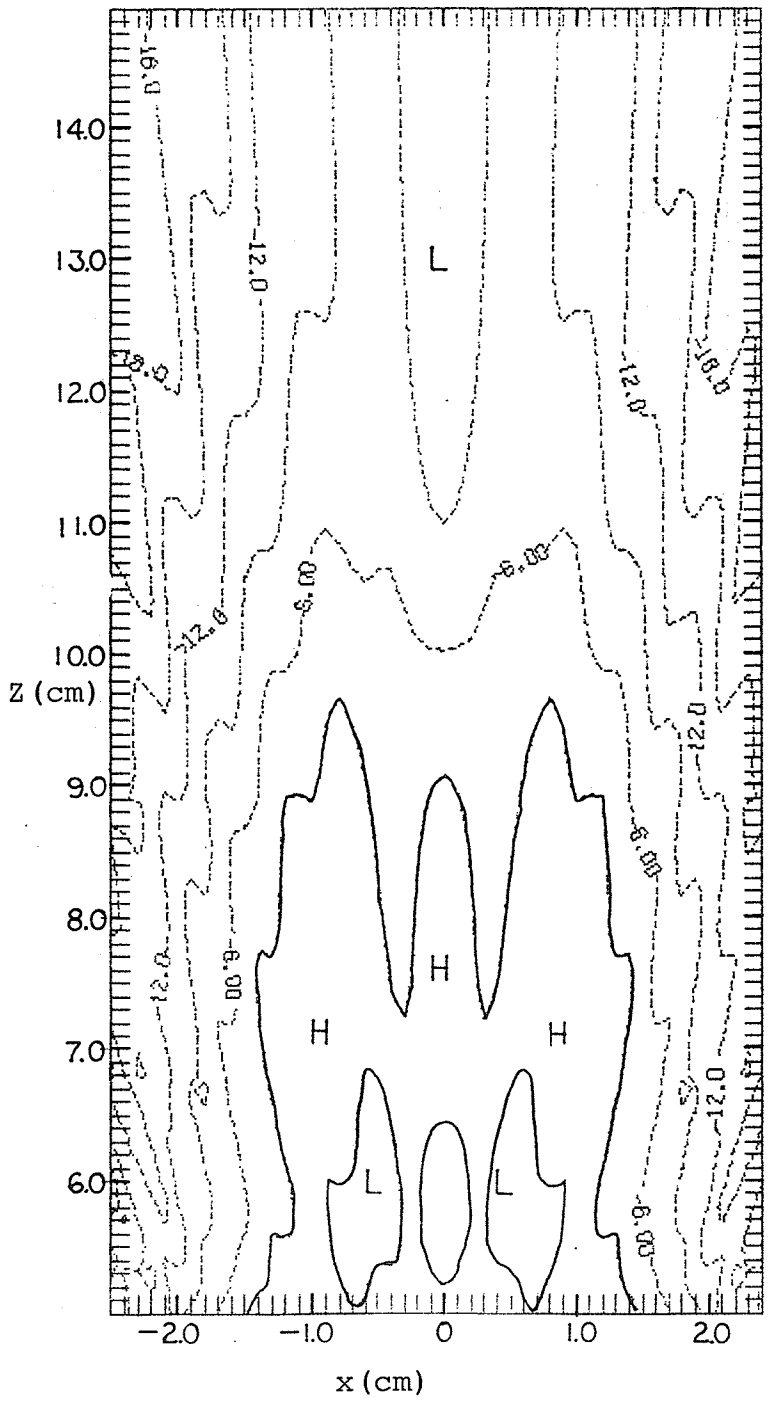

Figure A.22. Simulated 3 dB intensity contours with ratio tissue attenuation from a single element.

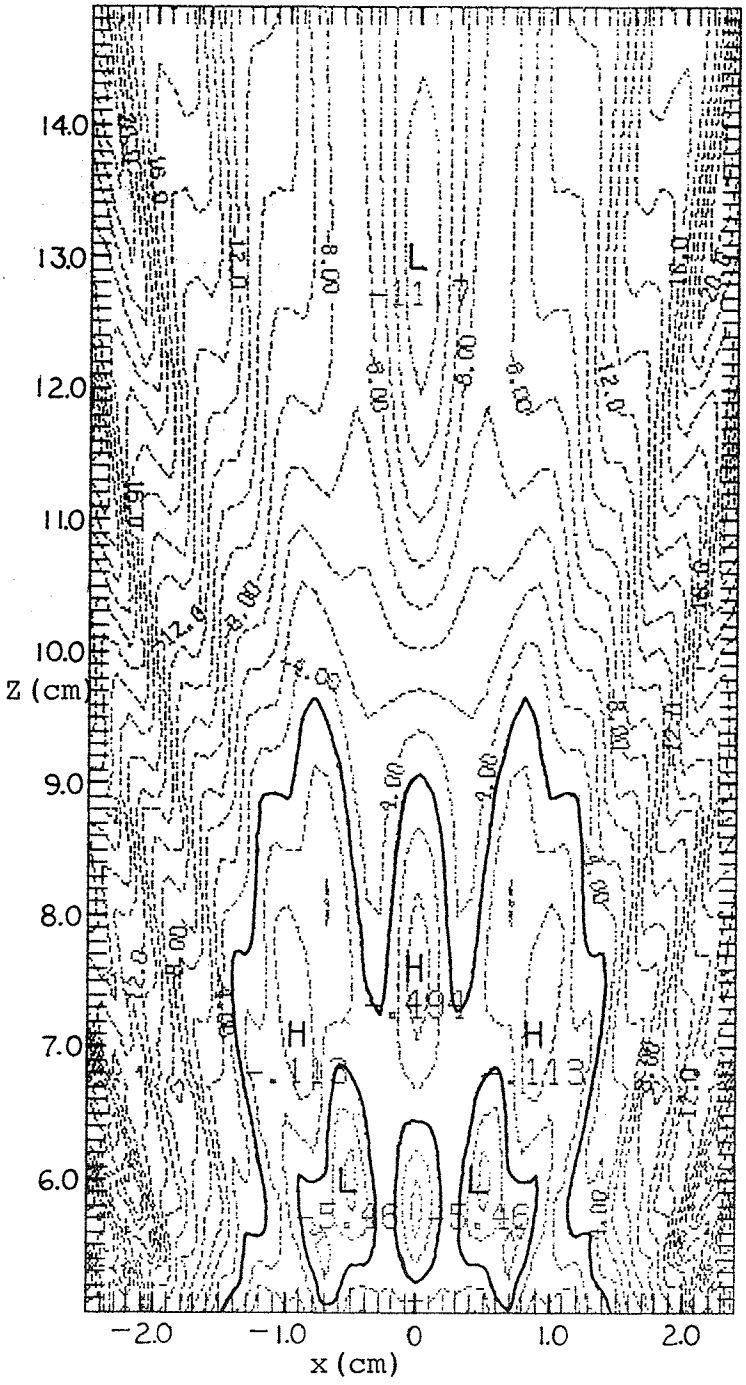

Figure A.23. Simulated 1 dB intensity contours with tissue attenuation from a single element.

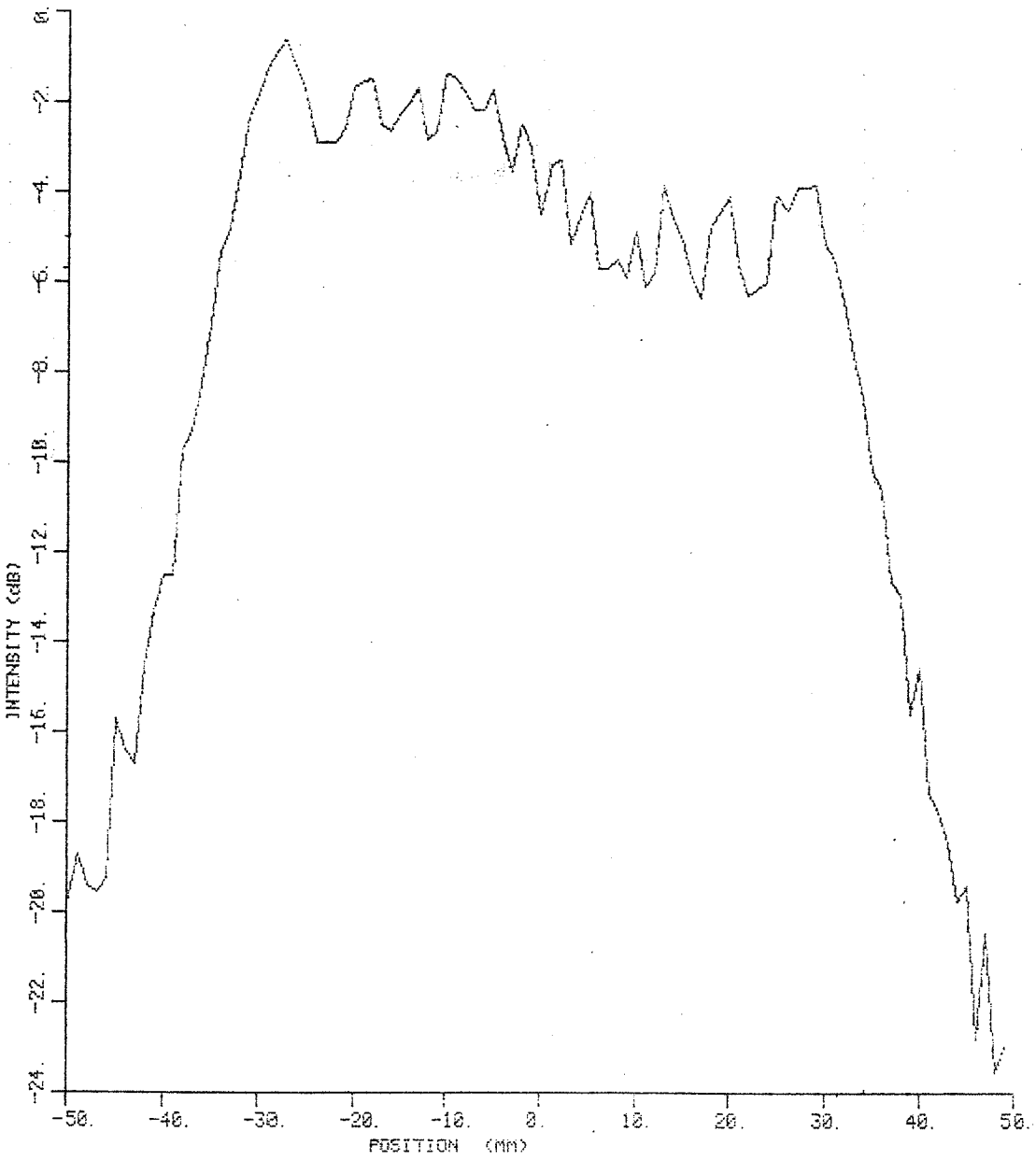

Figure A.24. Simulated transverse relative intensity profile at z = 7.0 cm from a pair of adjacent elements with a power ratio of one-half.

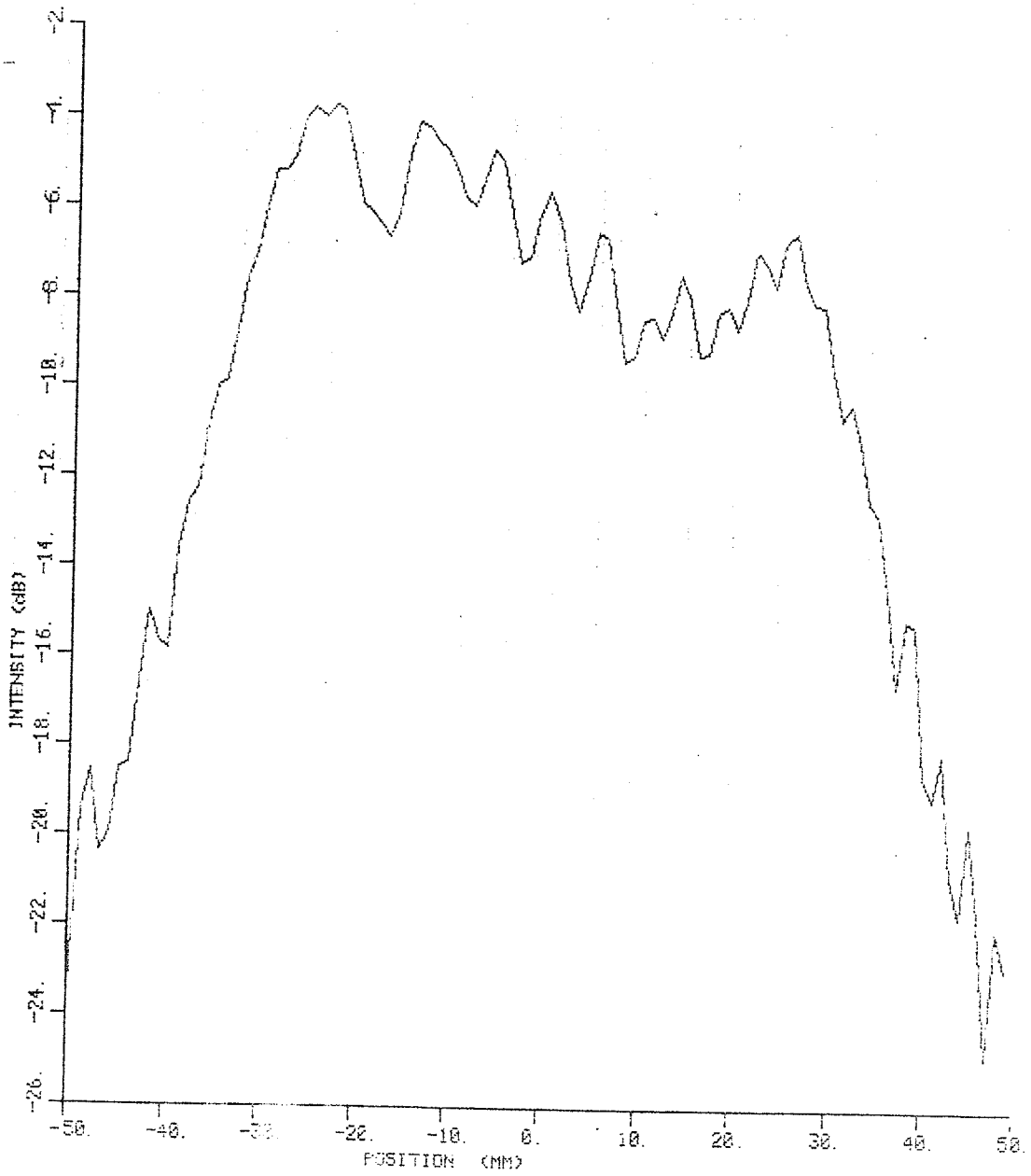

Figure A.25. Simulated transverse relative intensity profile at z = 13.0 cm from a pair of adjacent elements with a power ratio of one-half.

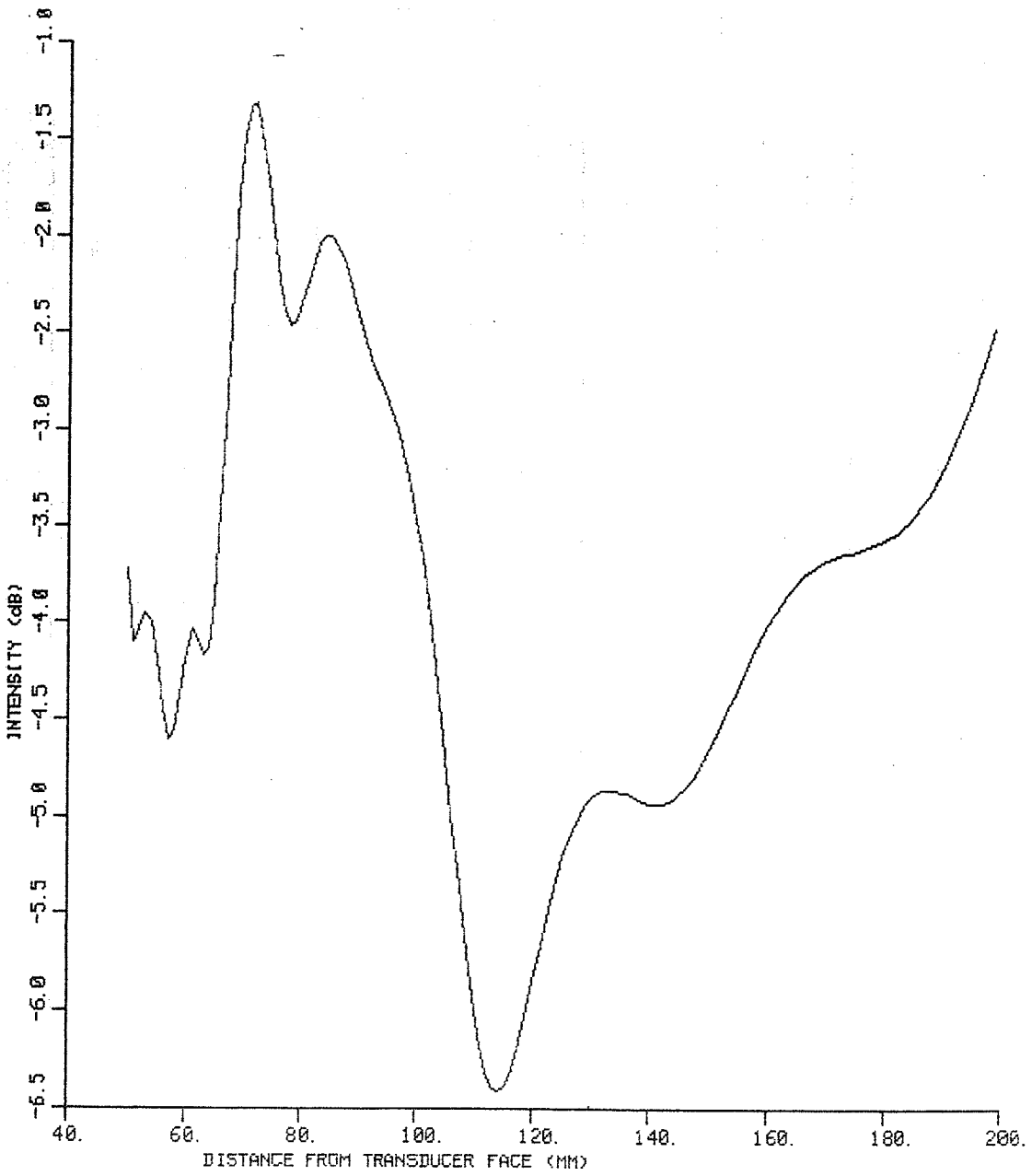

Figure A.26. Simulated offset axial relative intensity from a pair of adjacent elements with power variation.

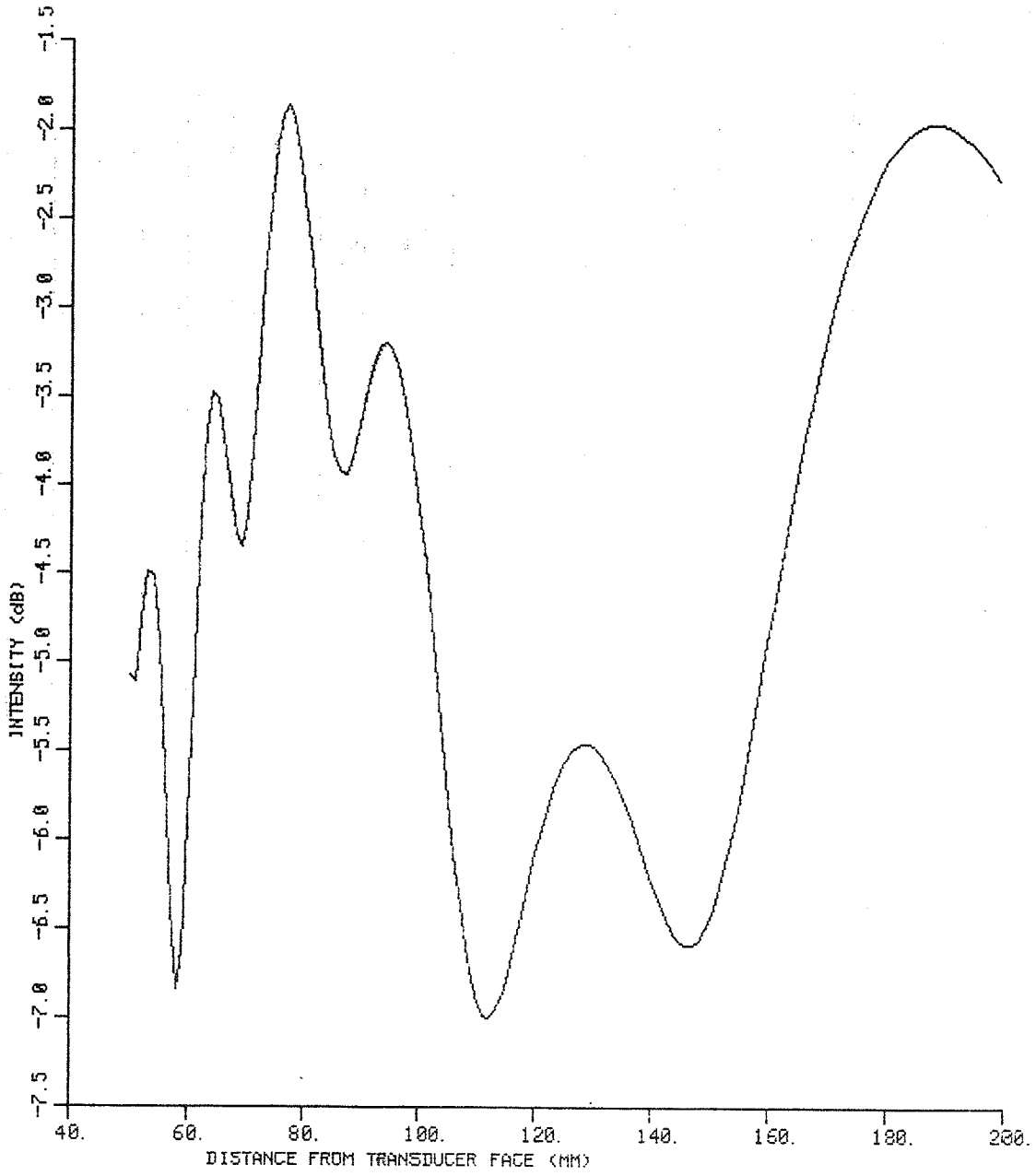

Figure A.27. Simulated axial relative intensity from a pair of adjacent elements with power variation.

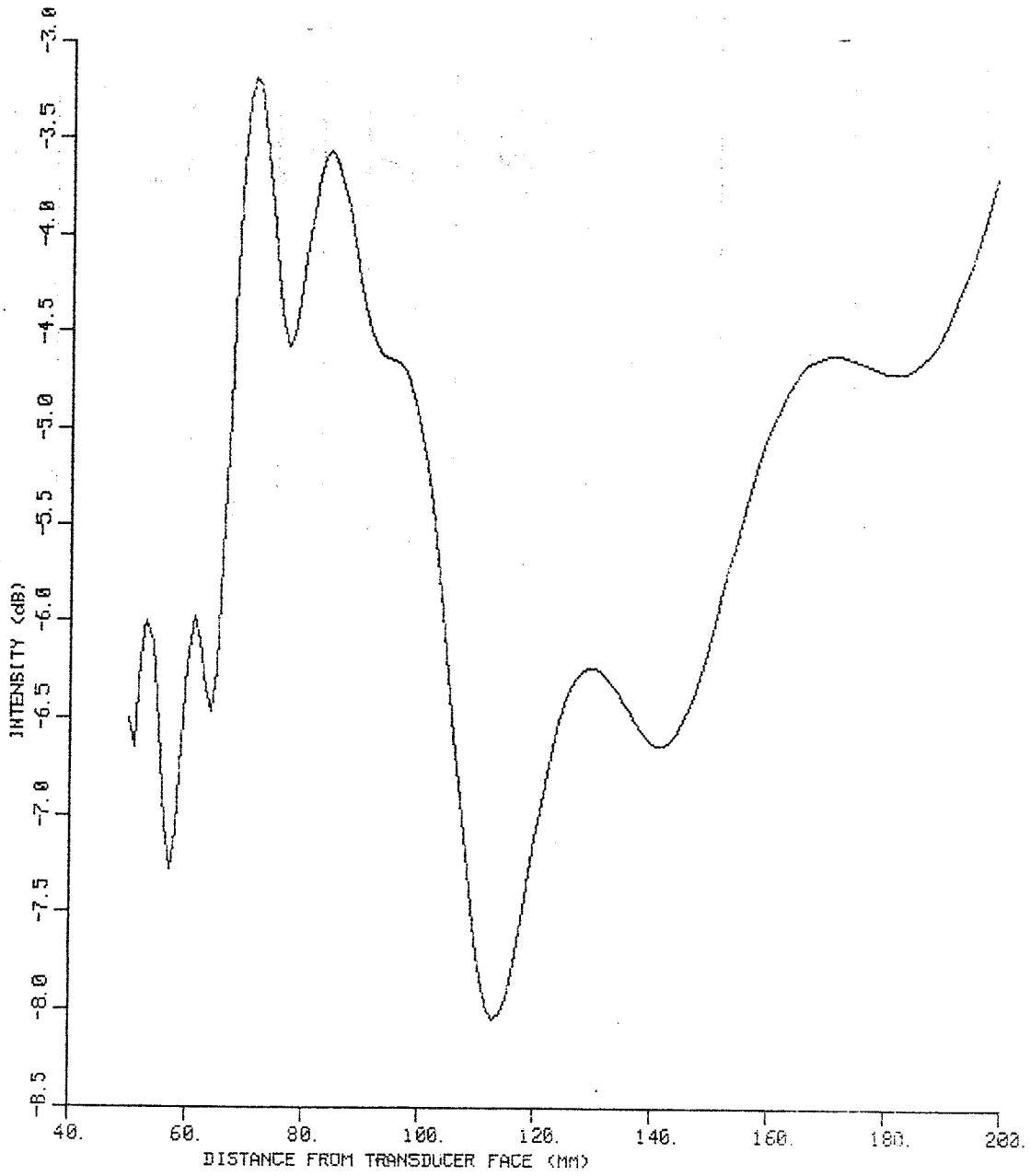

Figure A.28. Simulated offset axial relative intensity from a pair of adjacent elements with power variation.

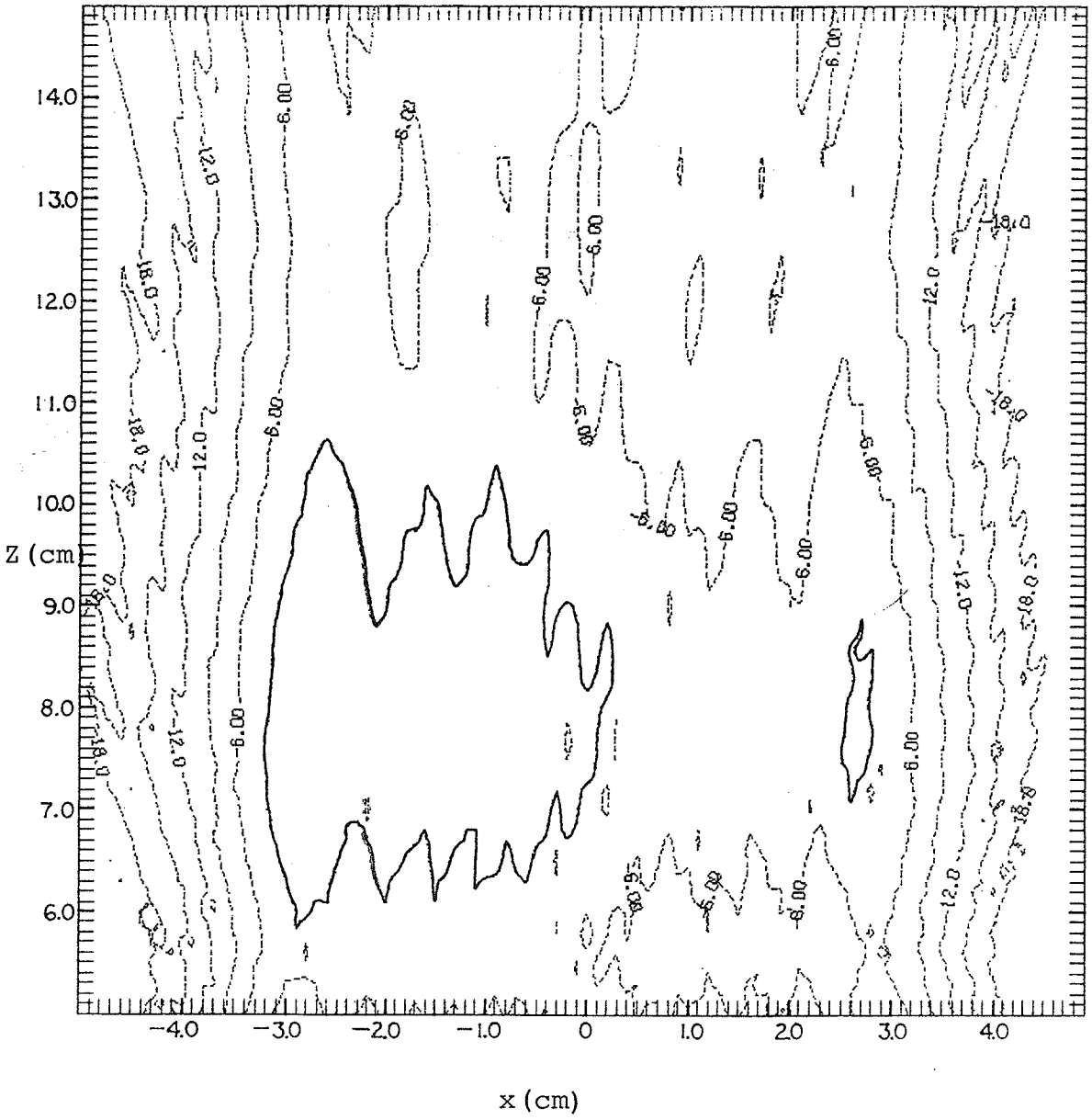

Figure A.29. Simulated 3 dB intensity contours from a pair of adjacent elements with power variation.

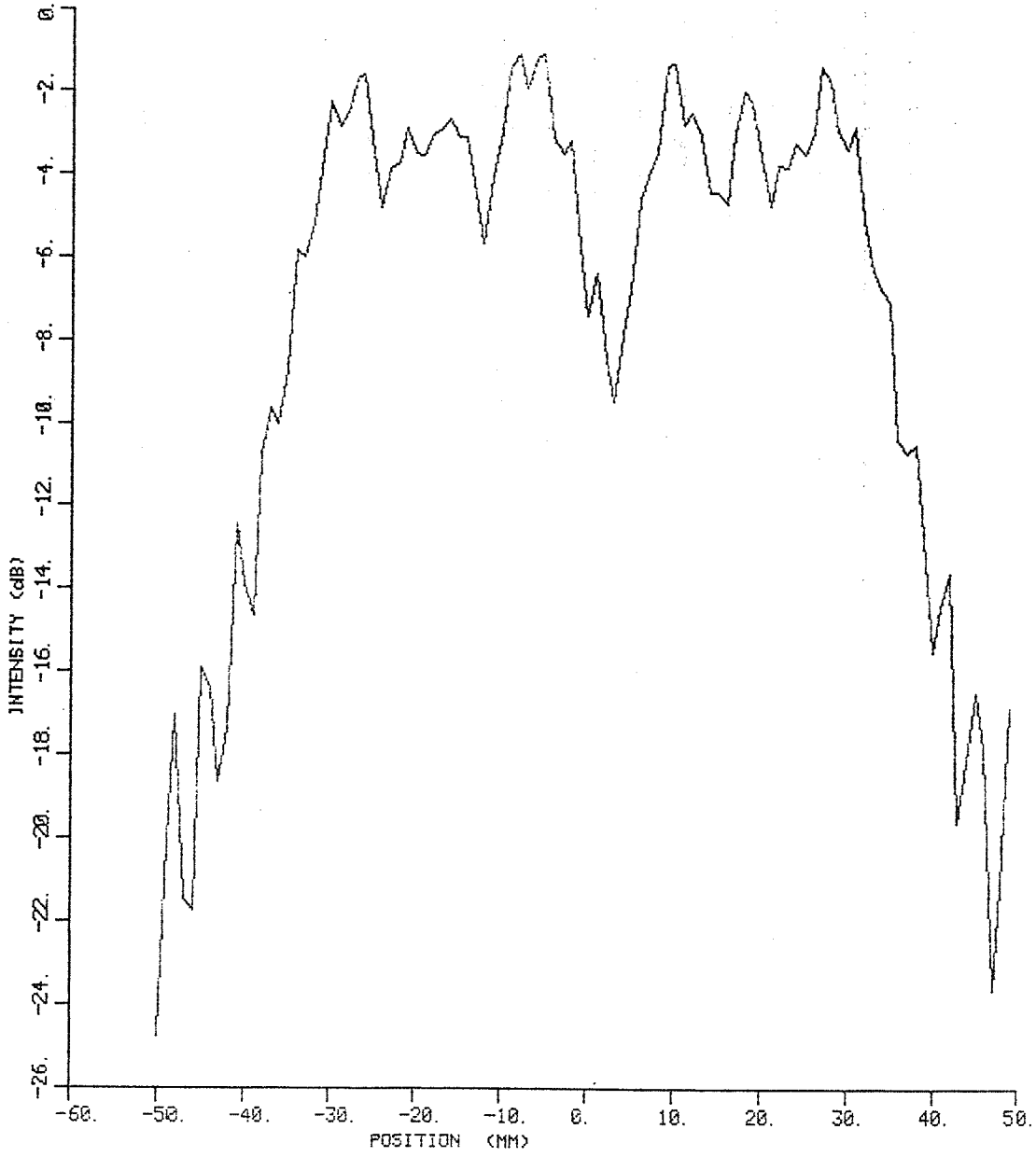

Figure A.30. Simulated transverse relative intensity profile at z = 7.0 cm from a pair of adjacent elements with a 90° phase difference.

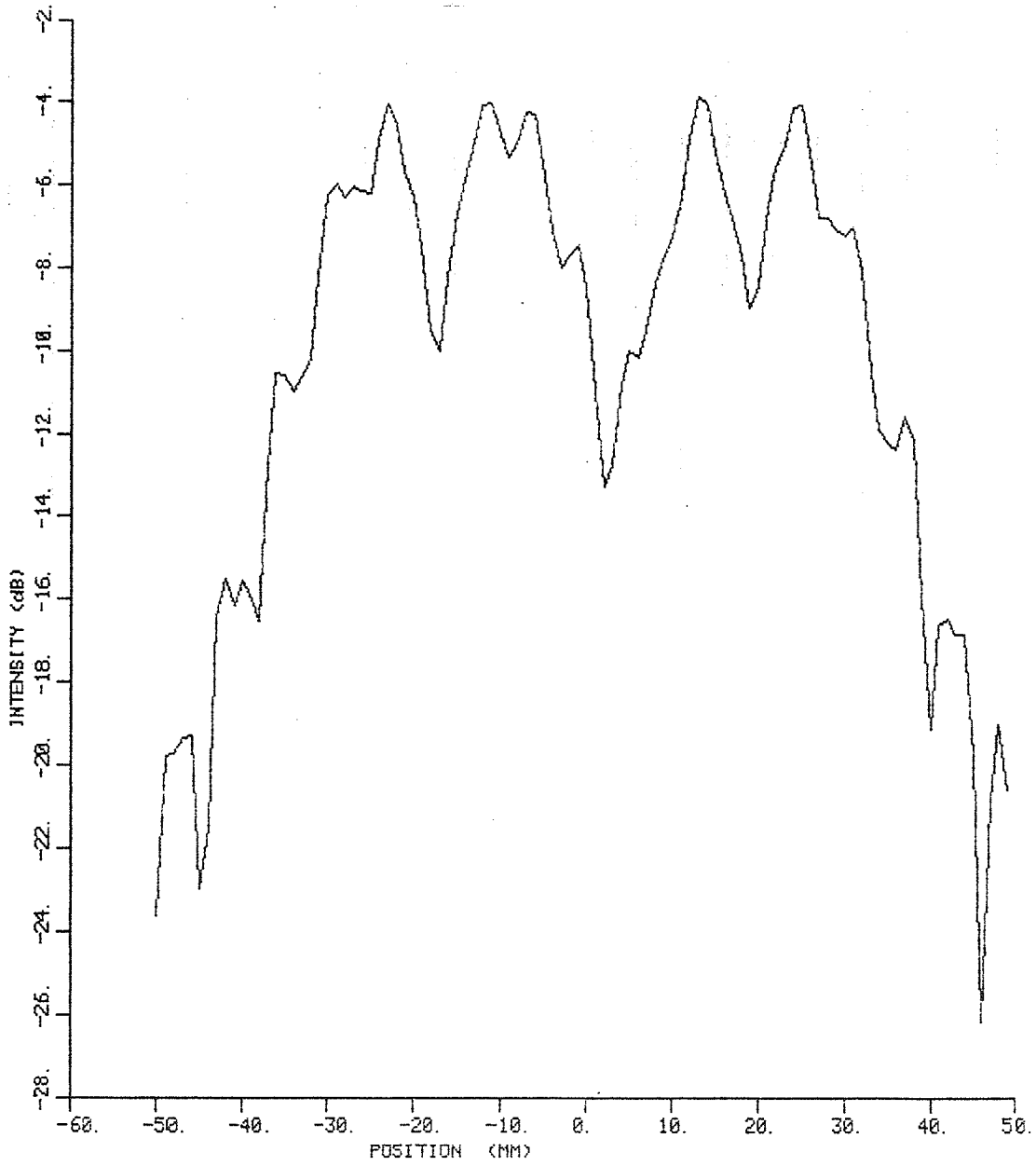

Figure A.31. Simulated transverse relative intensity profile at z = 13.0 cm from a pair of adjacent elements with a 90° phase difference.

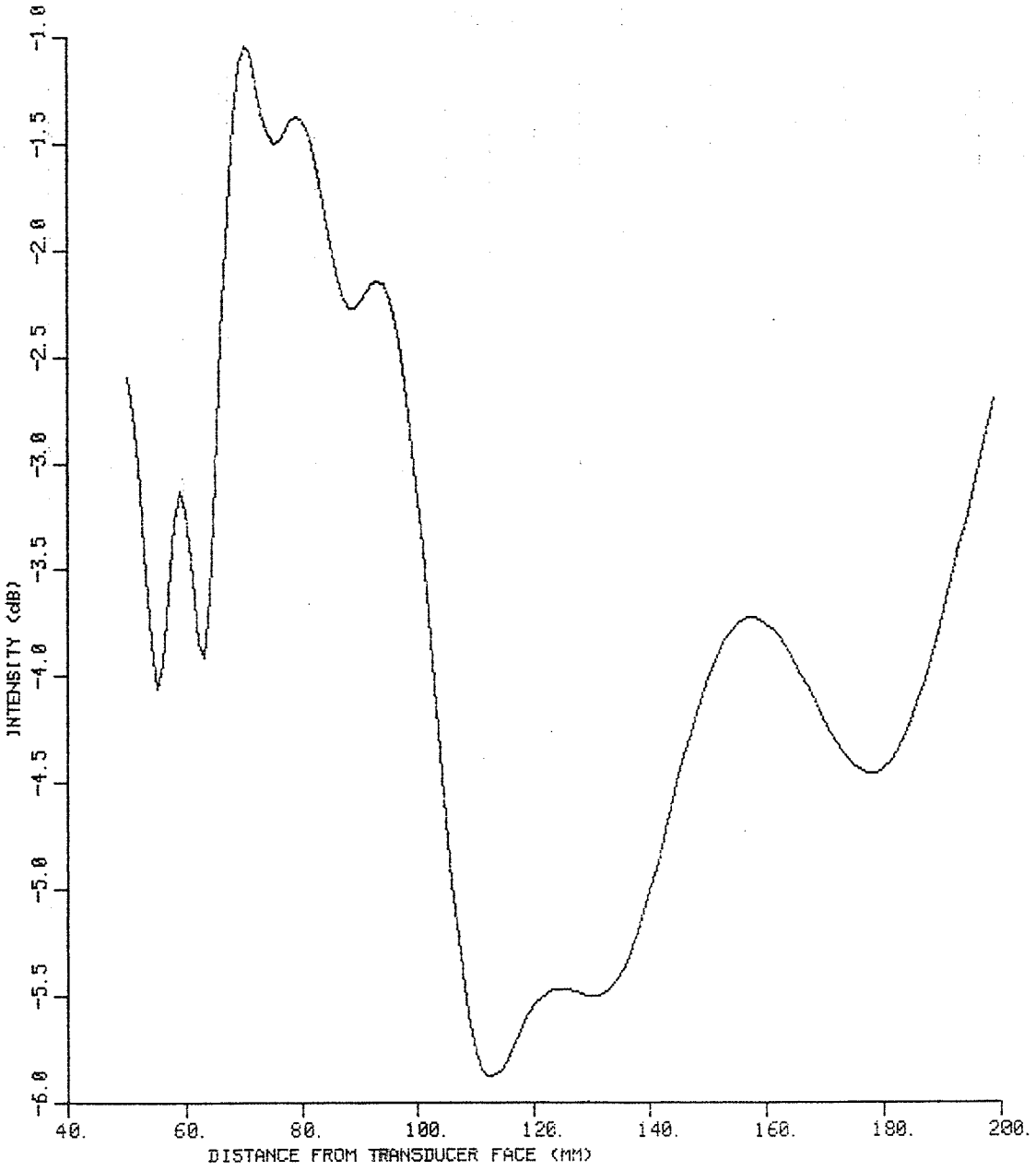

Figure A.32. Simulated offset axial relative intensity from a pair of adjacent elements with a 90^{o} phase difference.

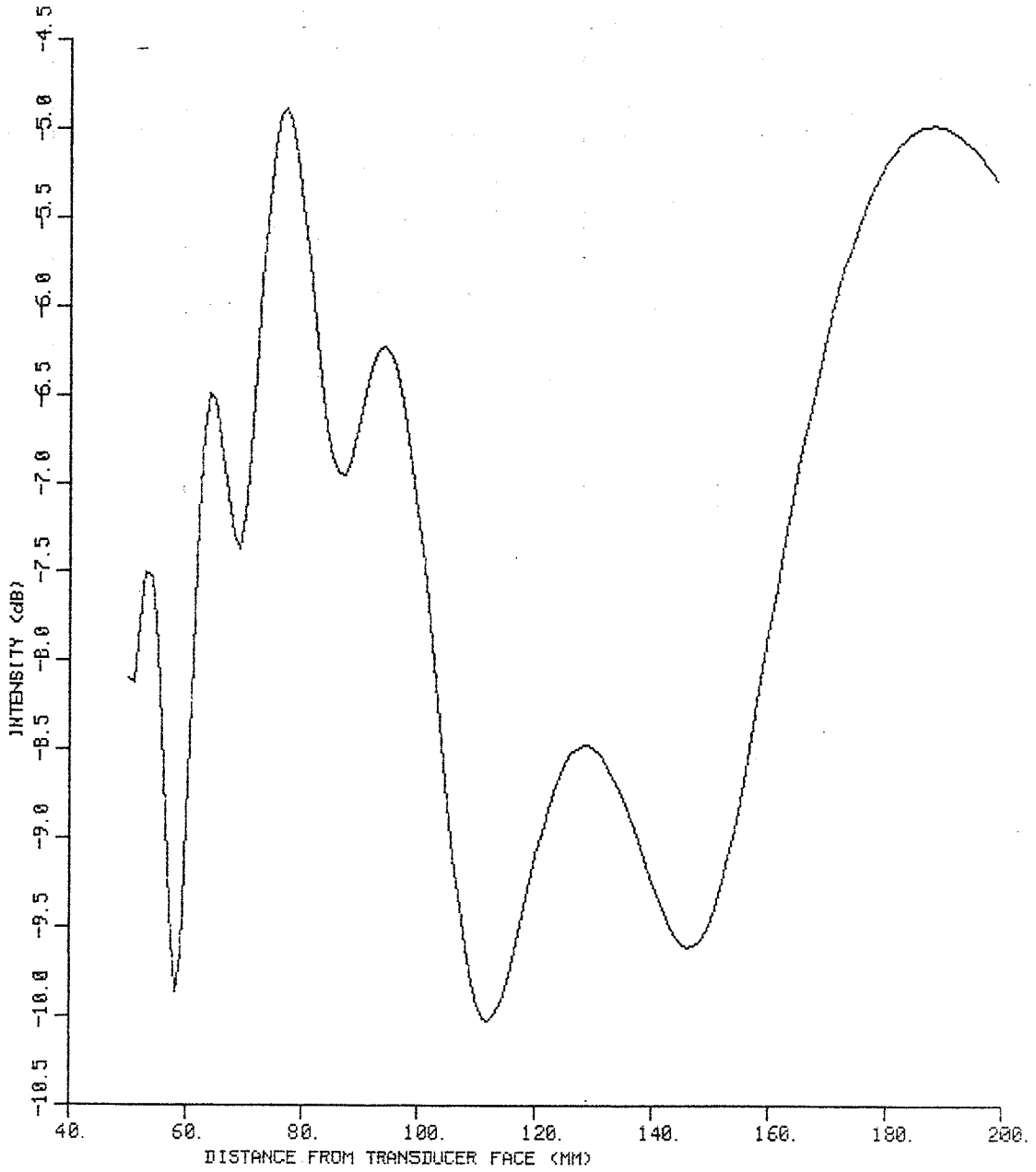

Figure A.33. Simulated axial relative intensity from a pair of adjacent elements with a 90^{o} phase difference.

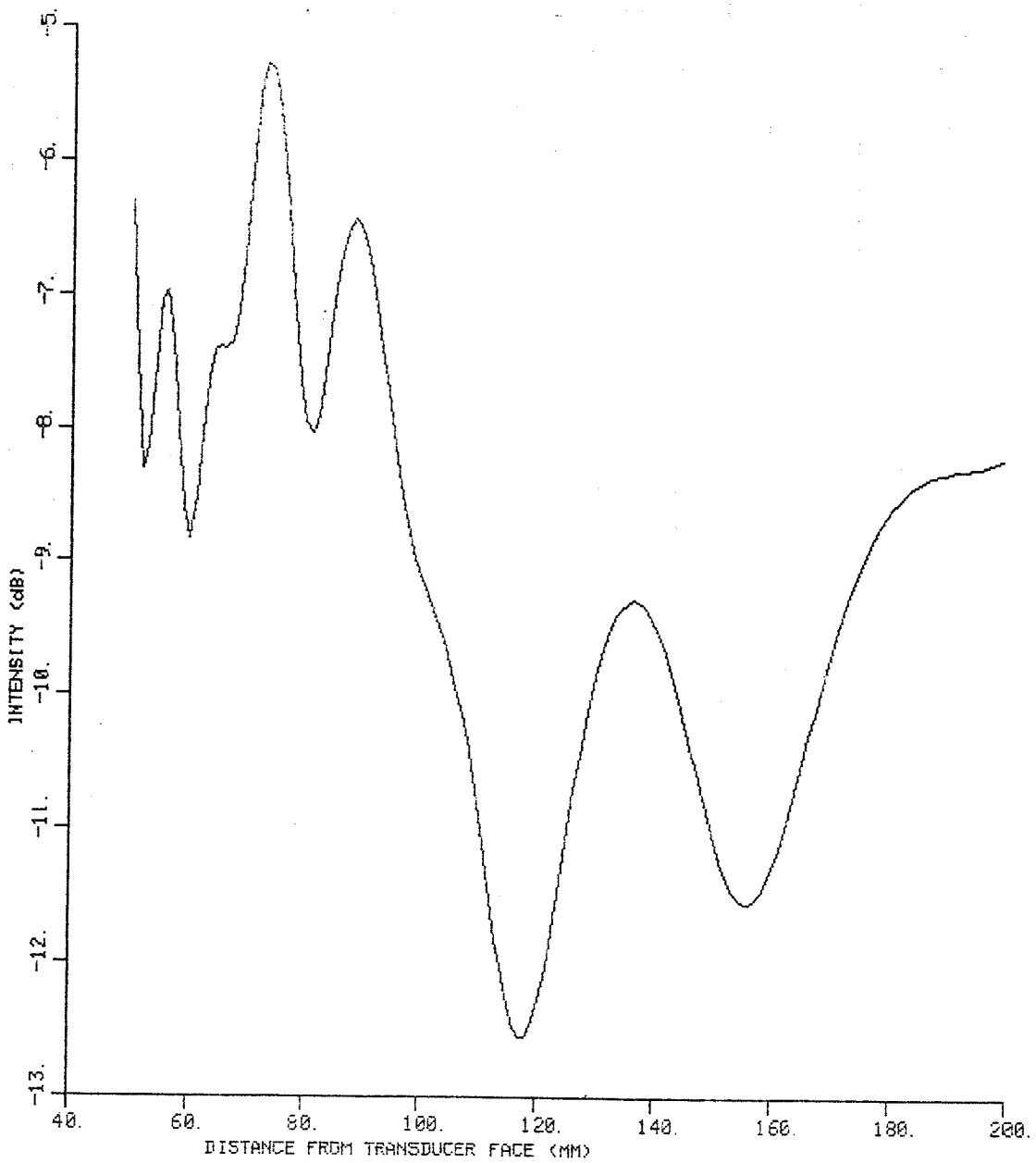

Figure A.34. Simulated offset axial relative intensity from a pair of adjacent elements with a 90° phase difference.

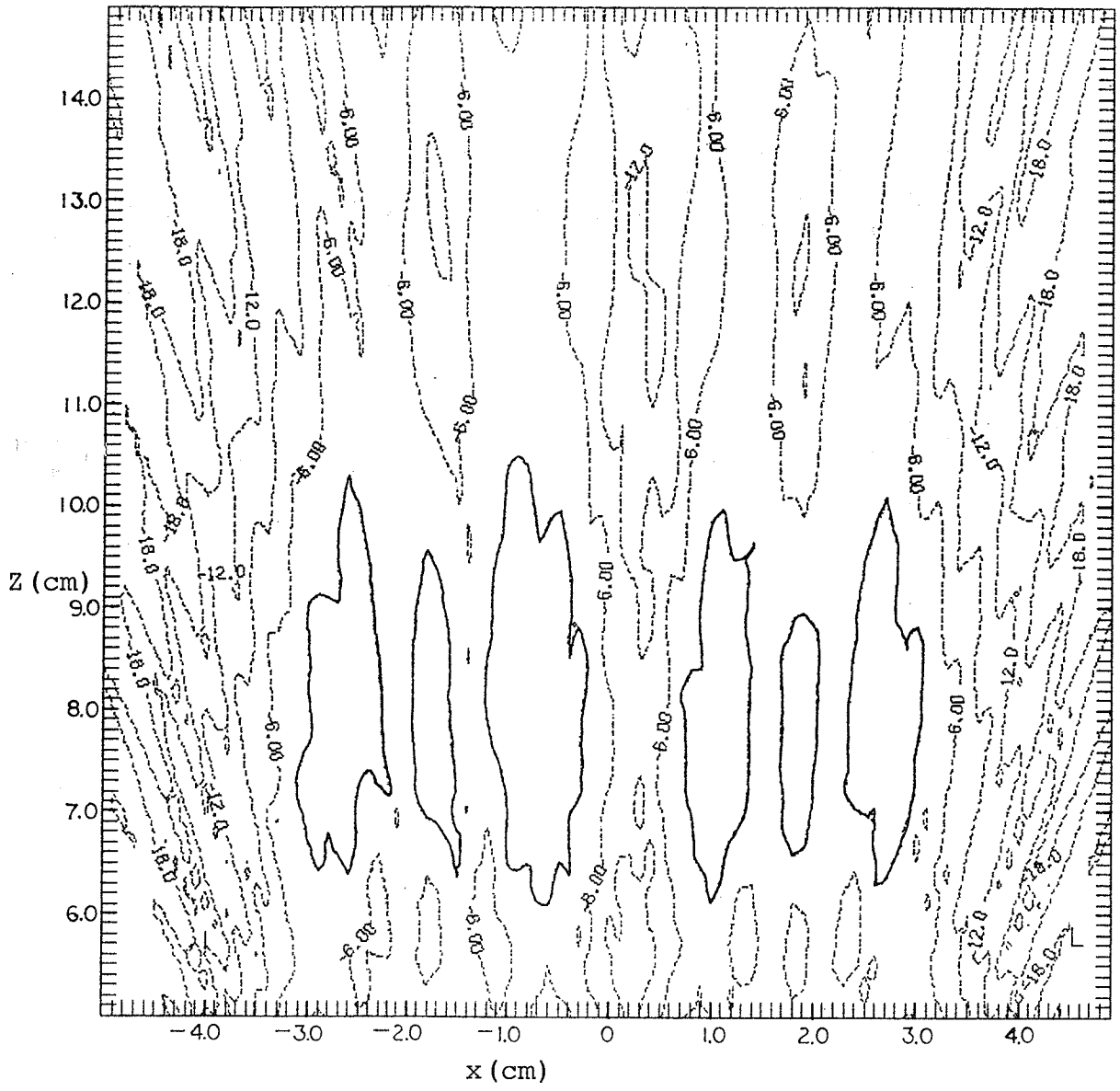

Figure A.35. Simulated 3 dB intensity contours from a pair of adjacent elements with a 90° phase difference.

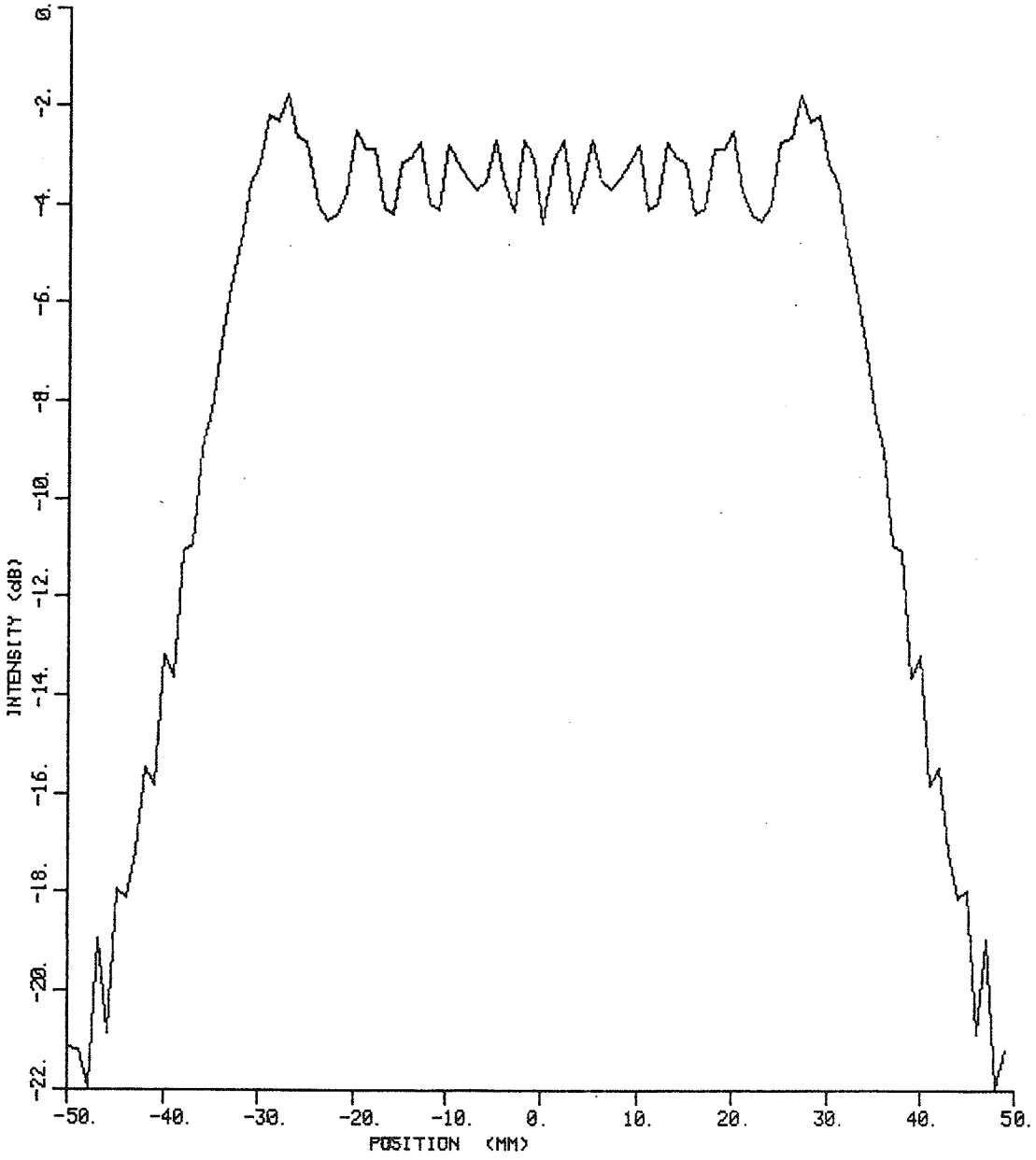

Figure A.36. Simulated transverse relative intensity at z = 7.0 cm from a block of 4 elements.

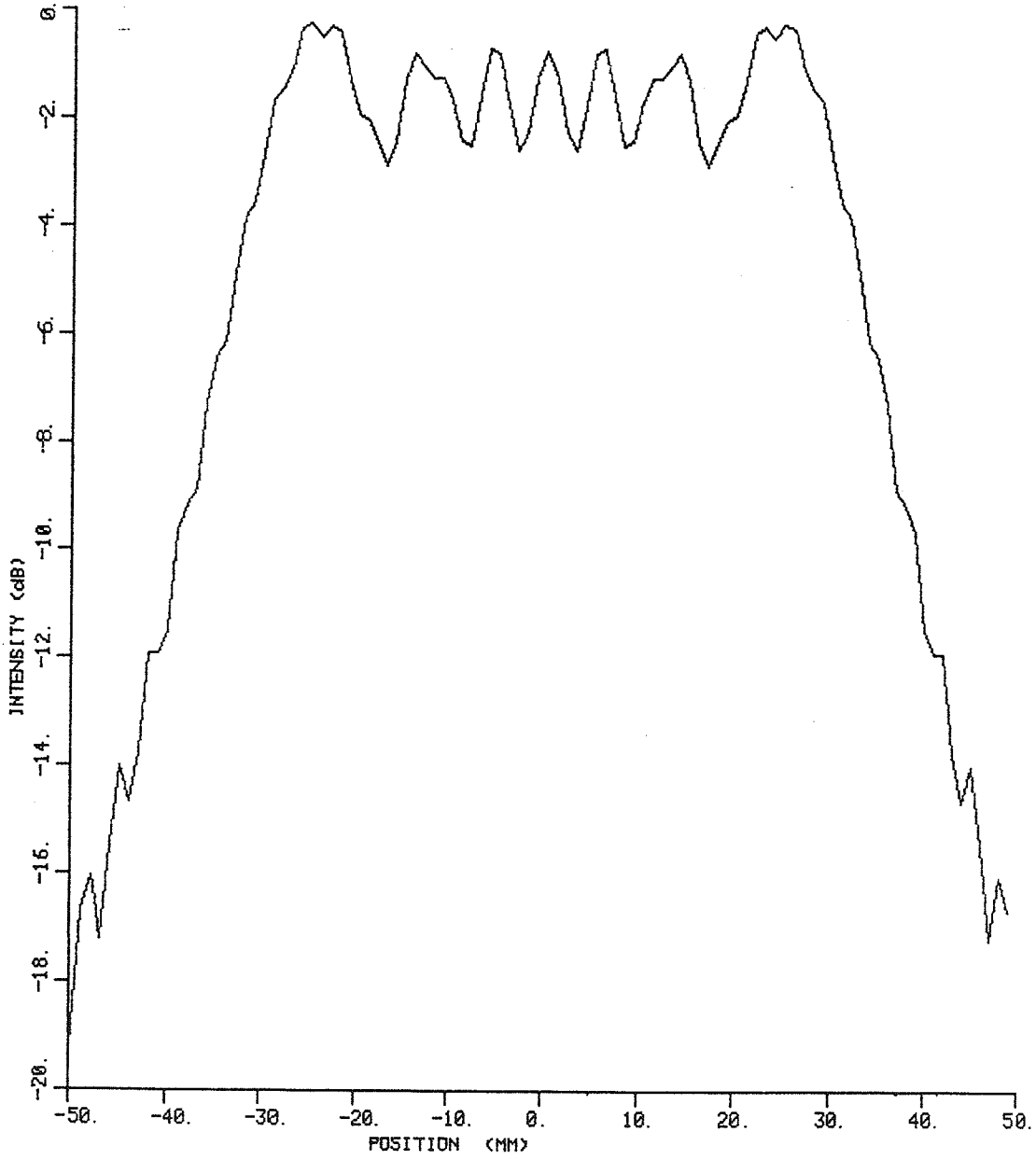

Figure A.37. Simulated transverse relative intensity at z = 13.0 cm from a block of 4 elements.

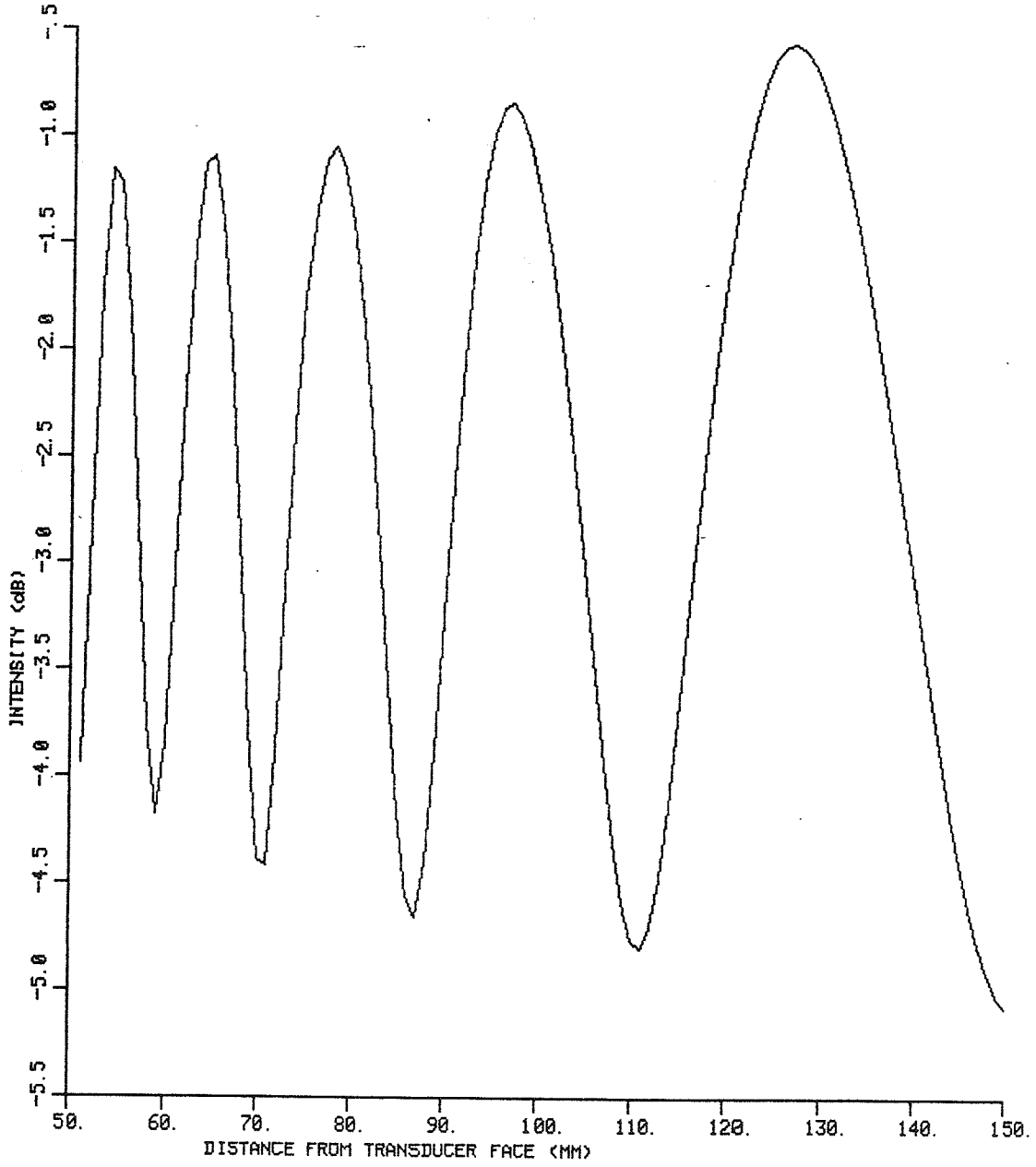

Figure A.38. Simulated axial relative intensity from a block of 4 elements.

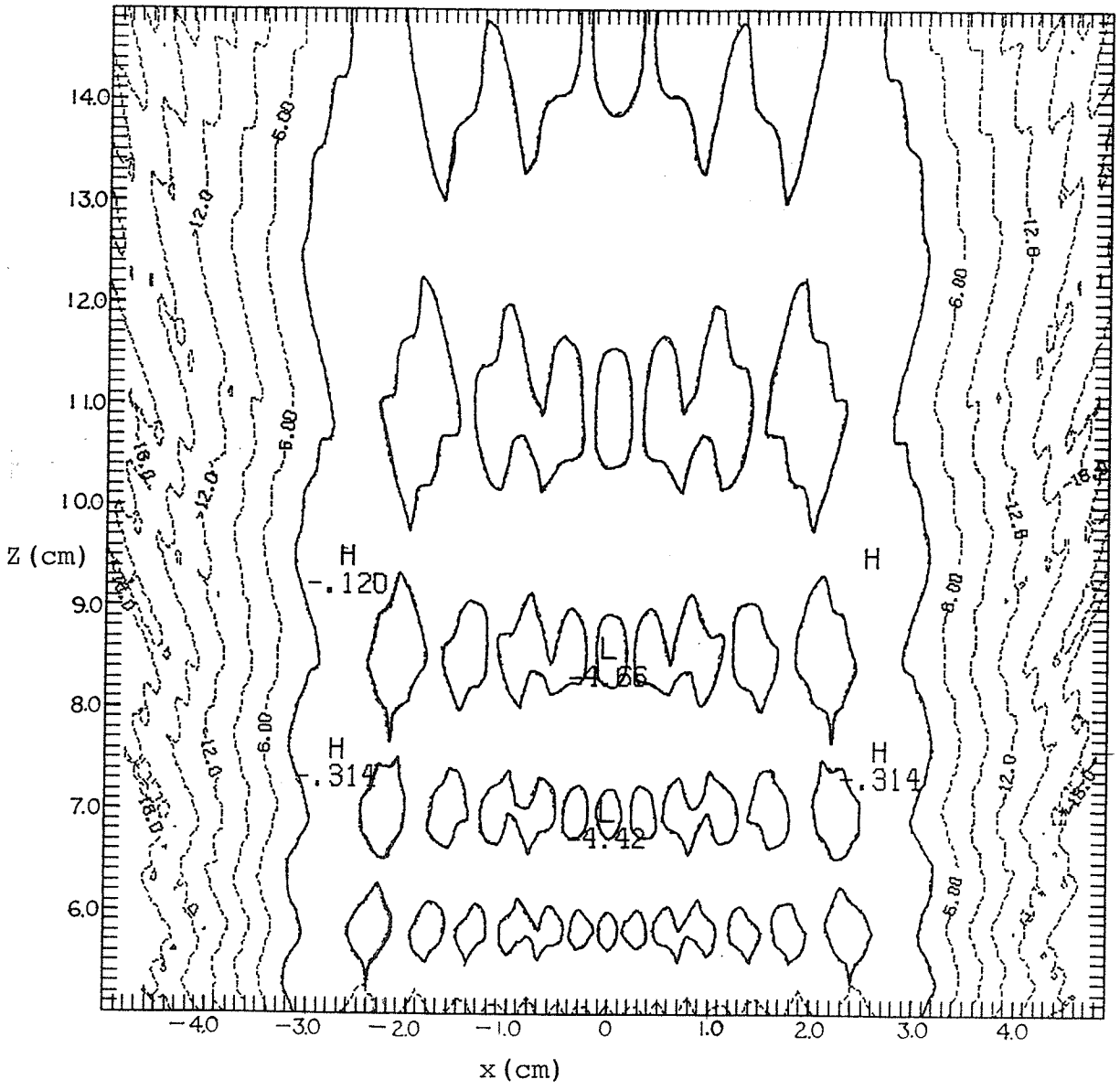

Figure A.39. Simulated 3 dB intensity contours from a block of 4 elements.

APPENDIX B

EXPERIMENTAL RESULTS

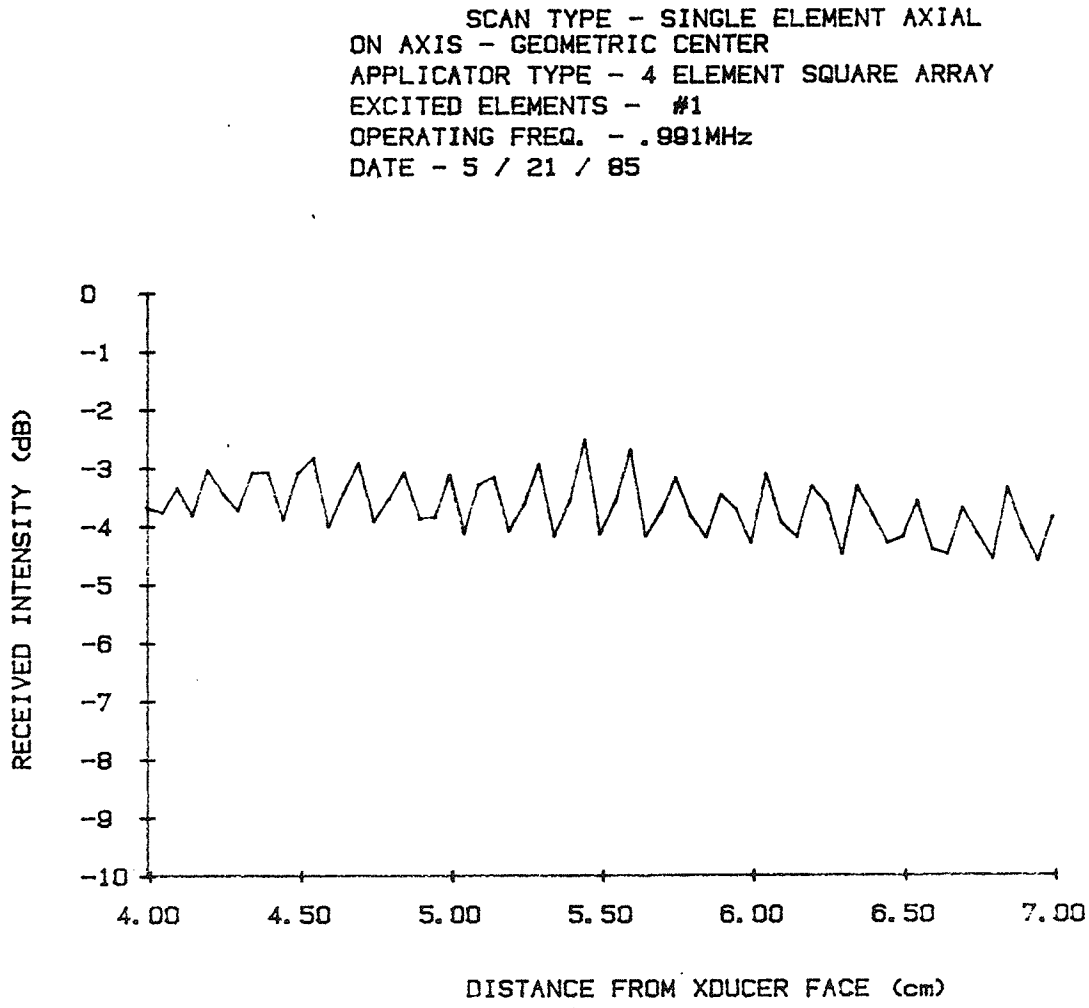

Figure B.1. Relative axial intensity from a single transducer element.

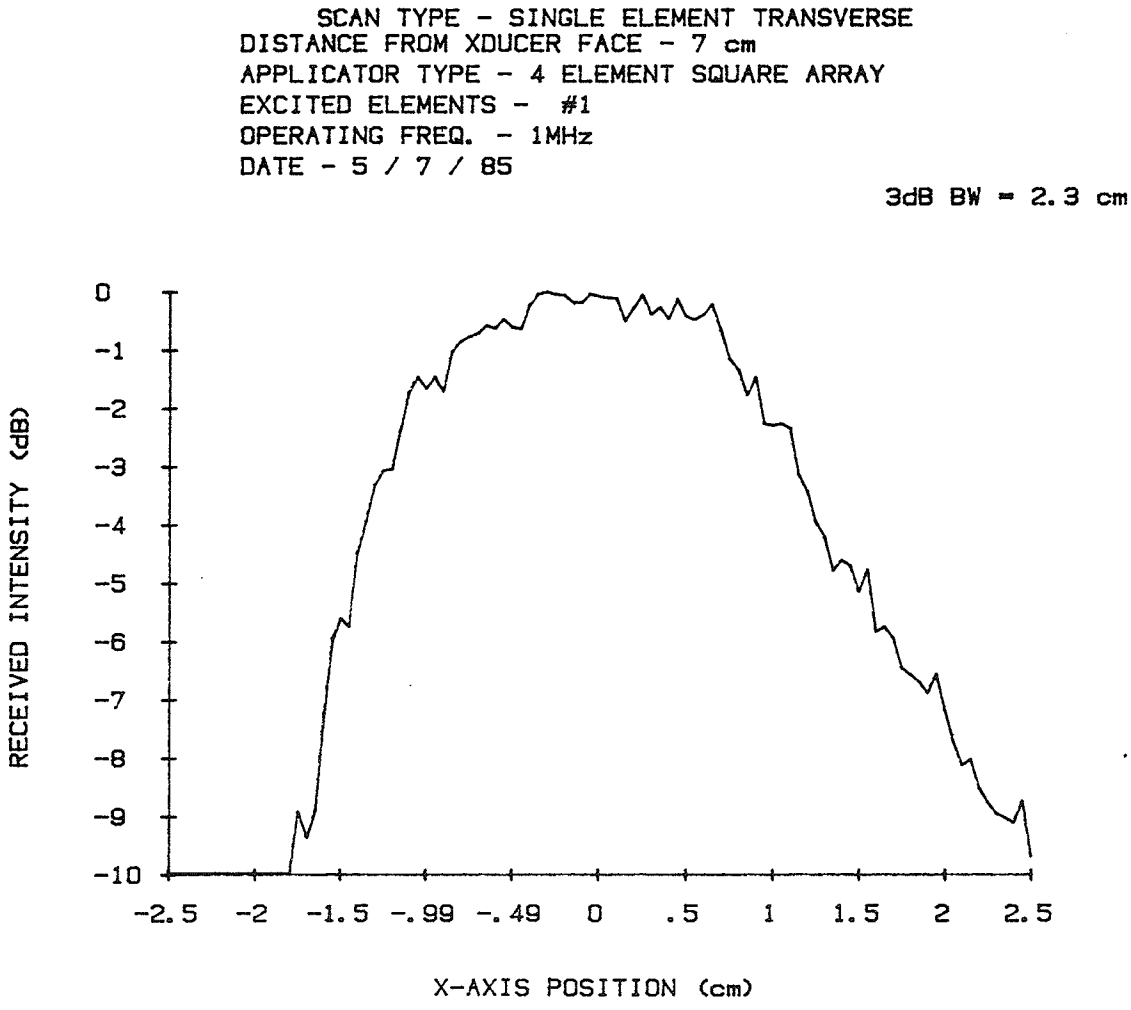

Figure B.2. Transverse relative intensity profile from element 1.

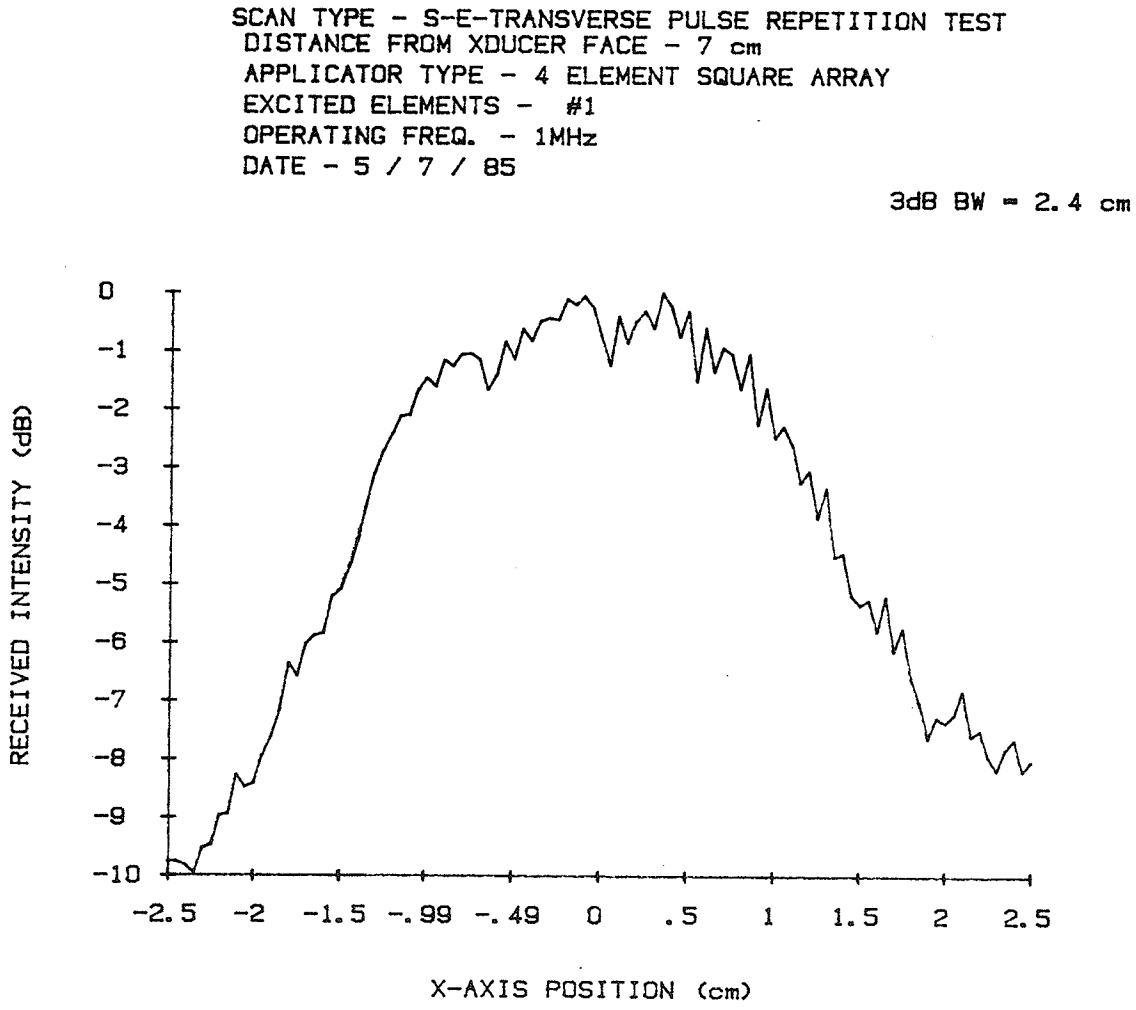

Figure B.3. Transverse relative intensity profile from element 1 at a 1 kHz pulse repetition frequency.

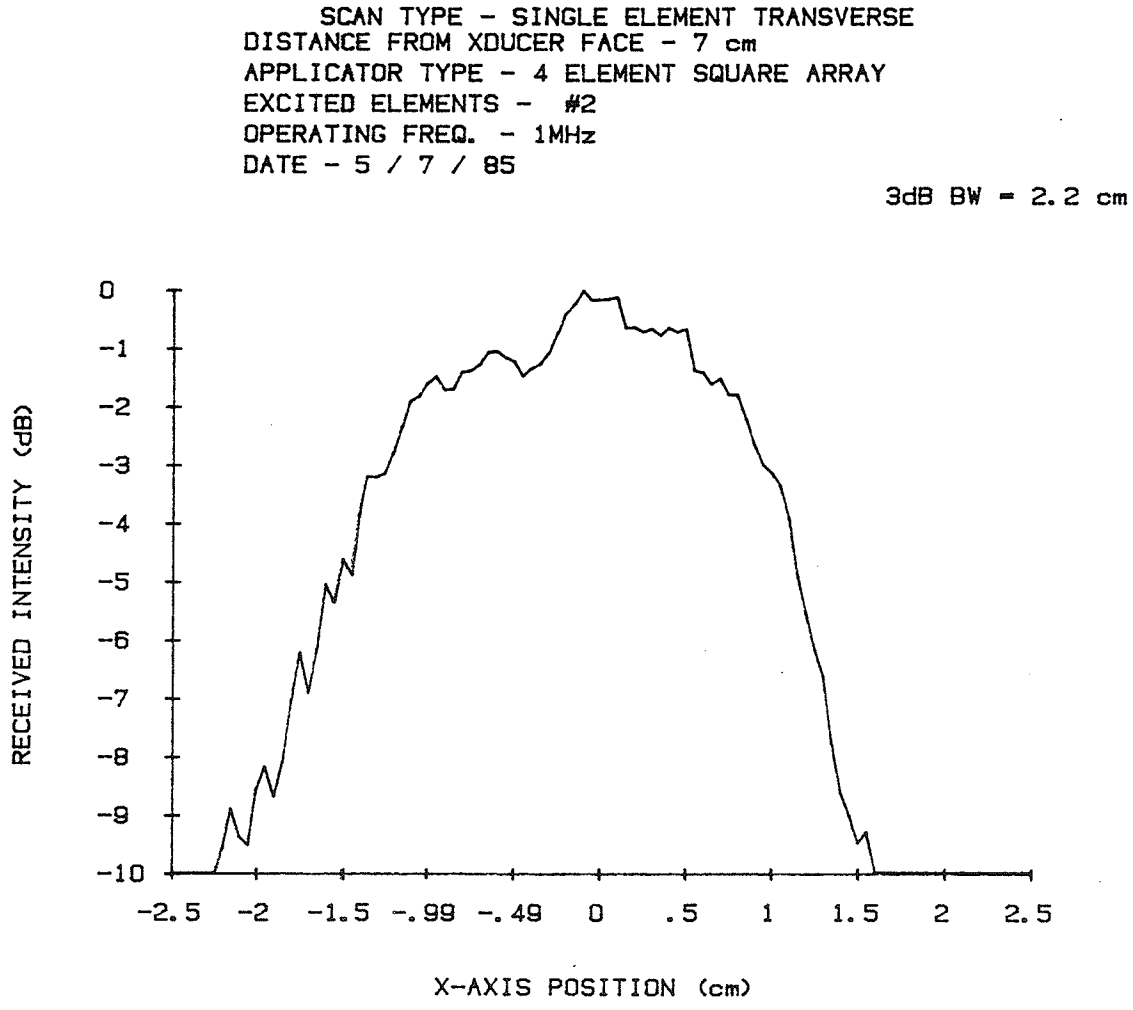

Figure B.4. Transverse relative intensity profile from element 2.

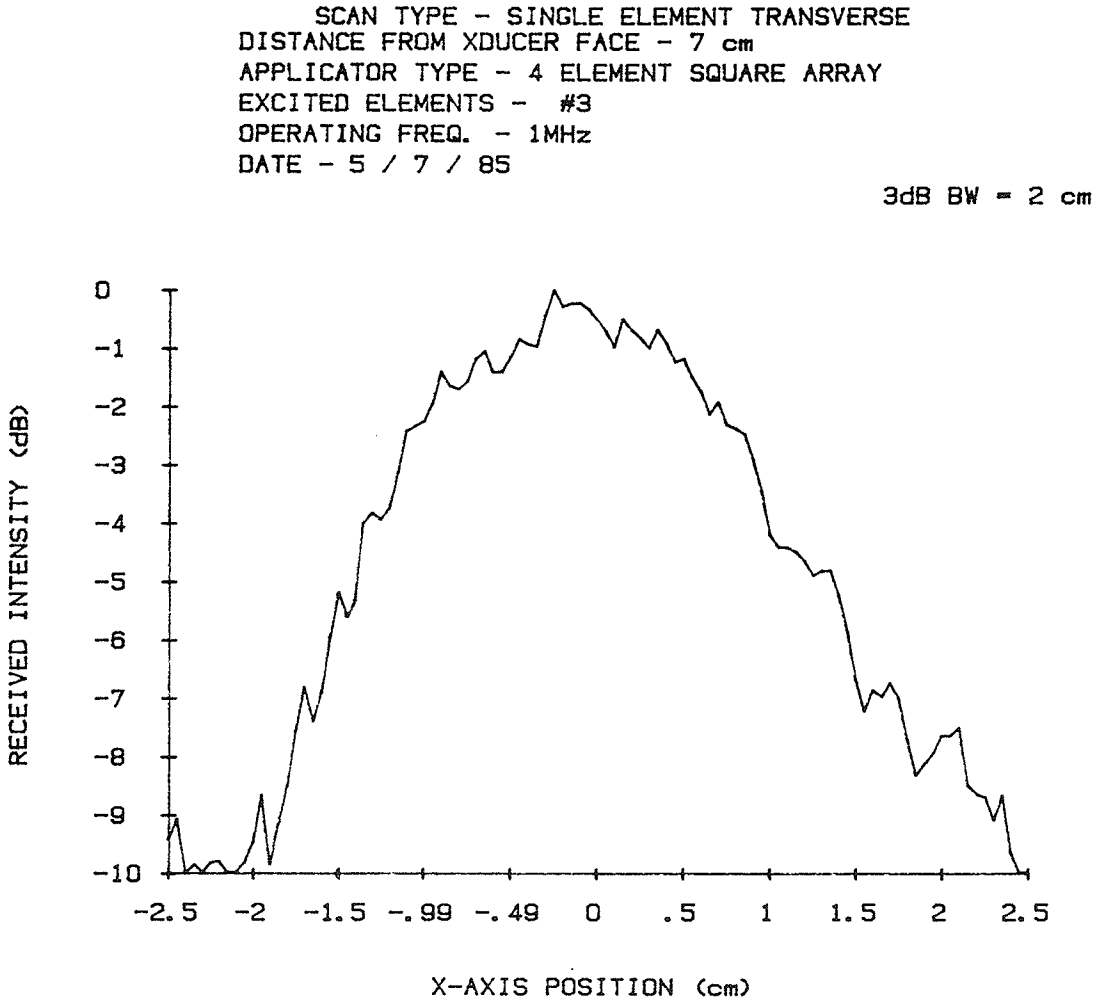

Figure B.5. Transverse relative intensity profile from element 3.

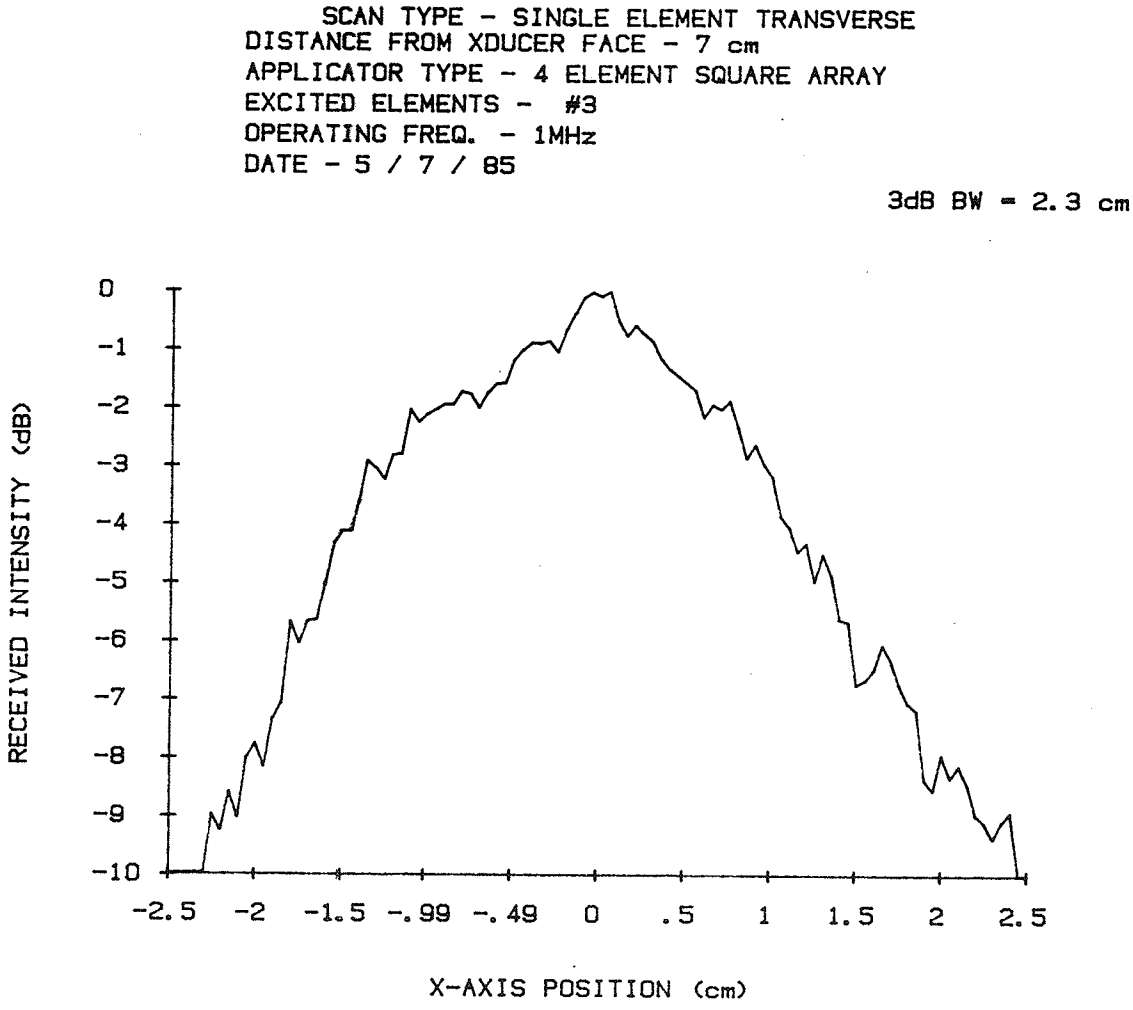

Figure B.6. Transverse relative intensity profile from element 3.

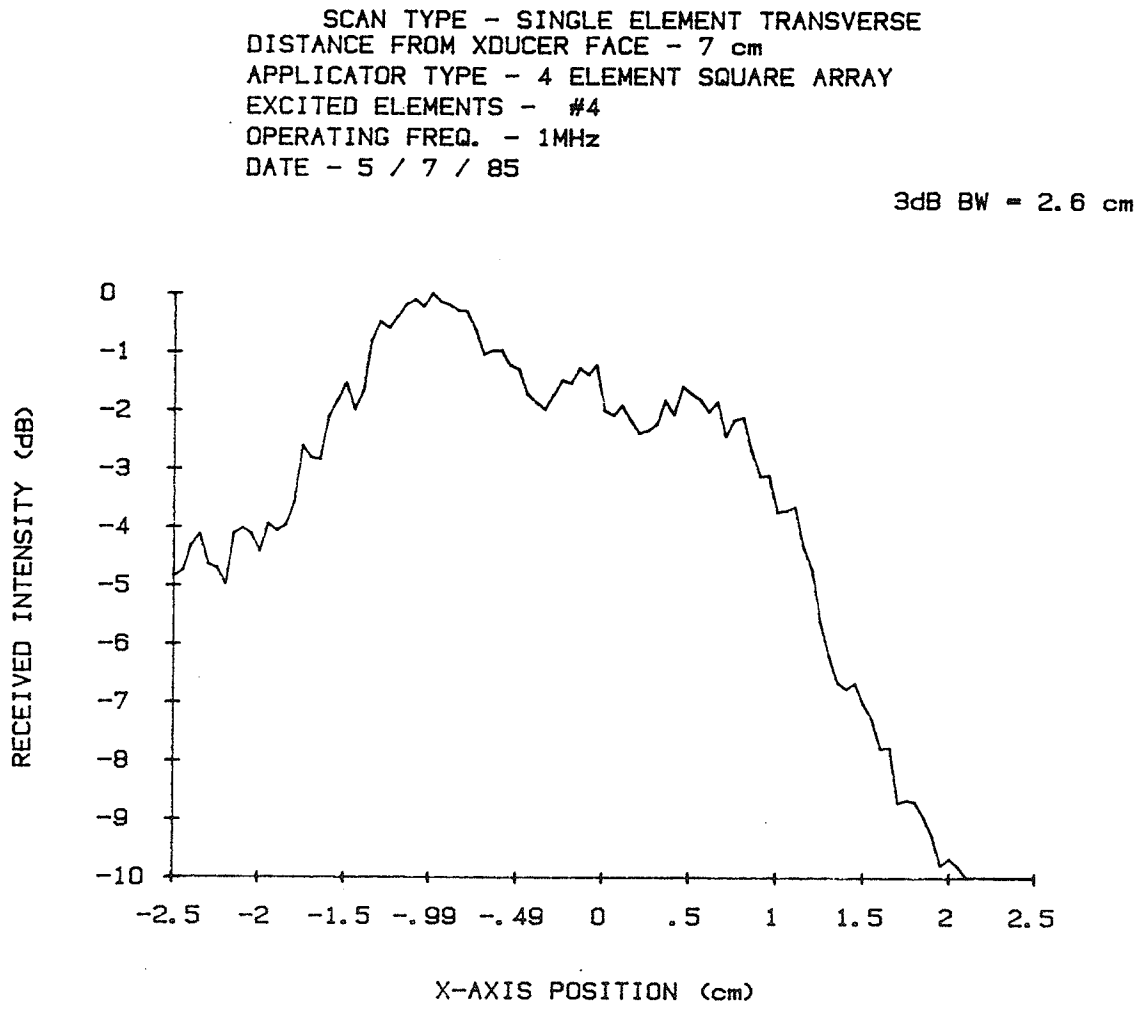

Figure B.7. Transverse relative intensity profile from element 4.

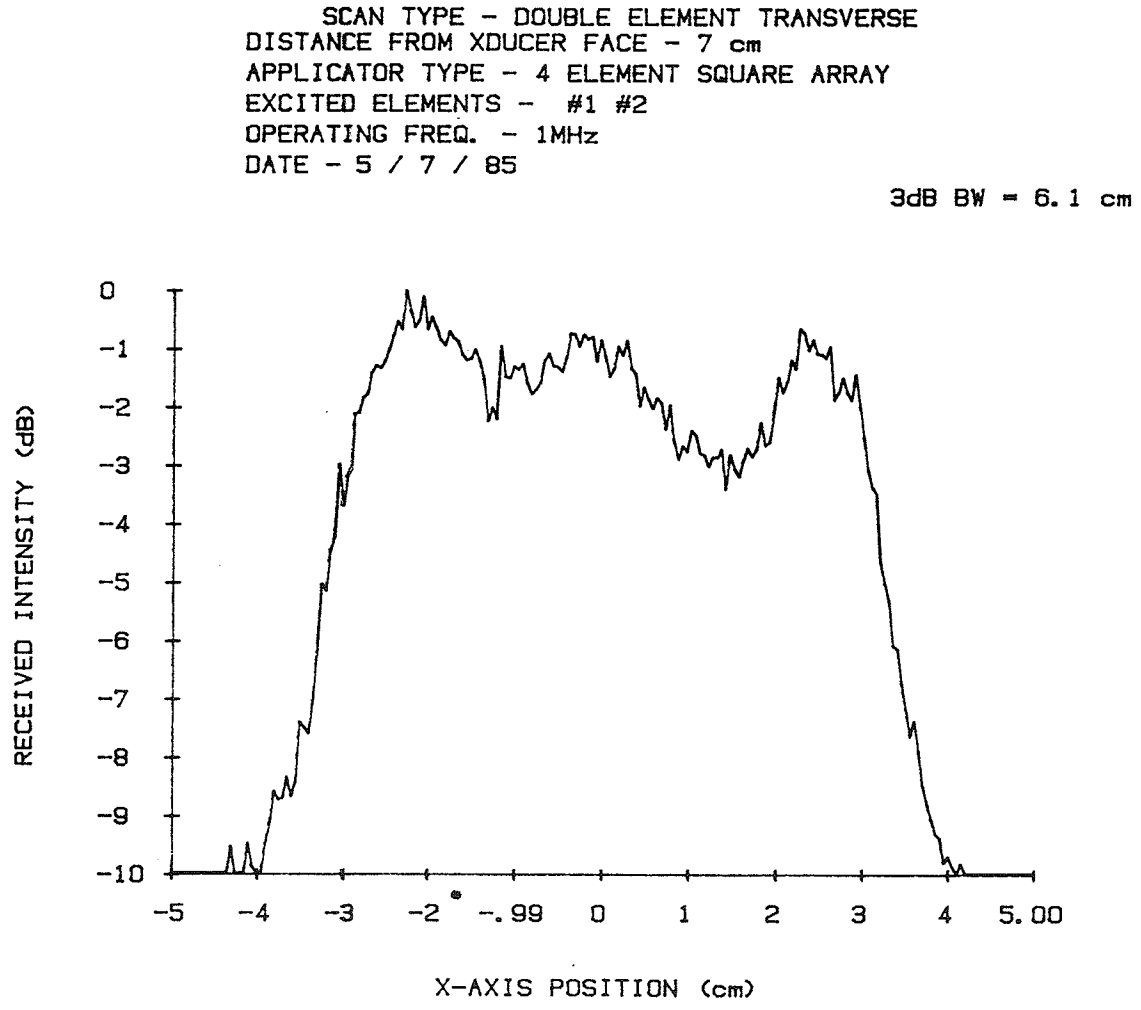

Figure B.8. Transverse relative intensity profile from elements 1 and 2.

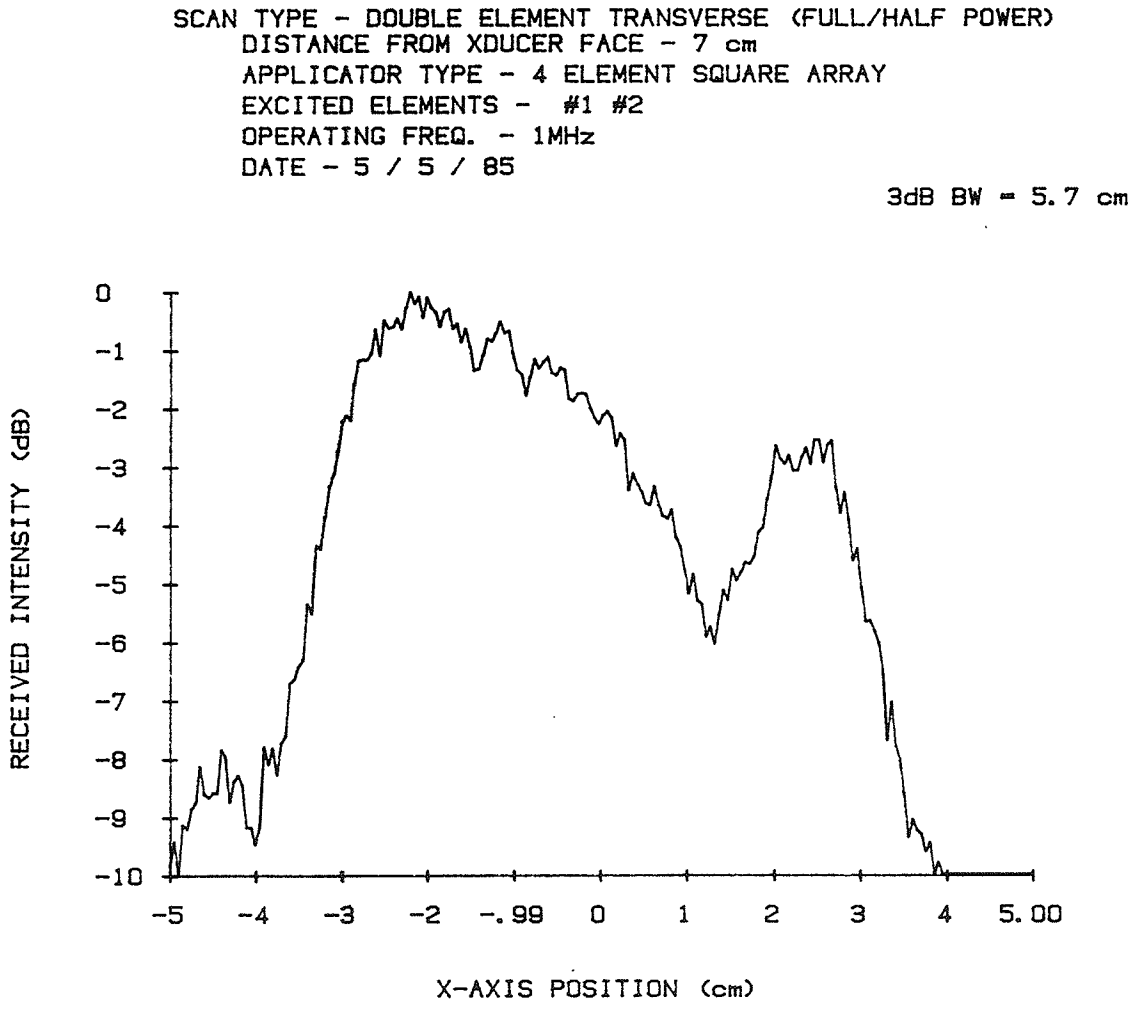

Figure B.9. Transverse relative intensity profile from elements 1 and 2 with power variation.

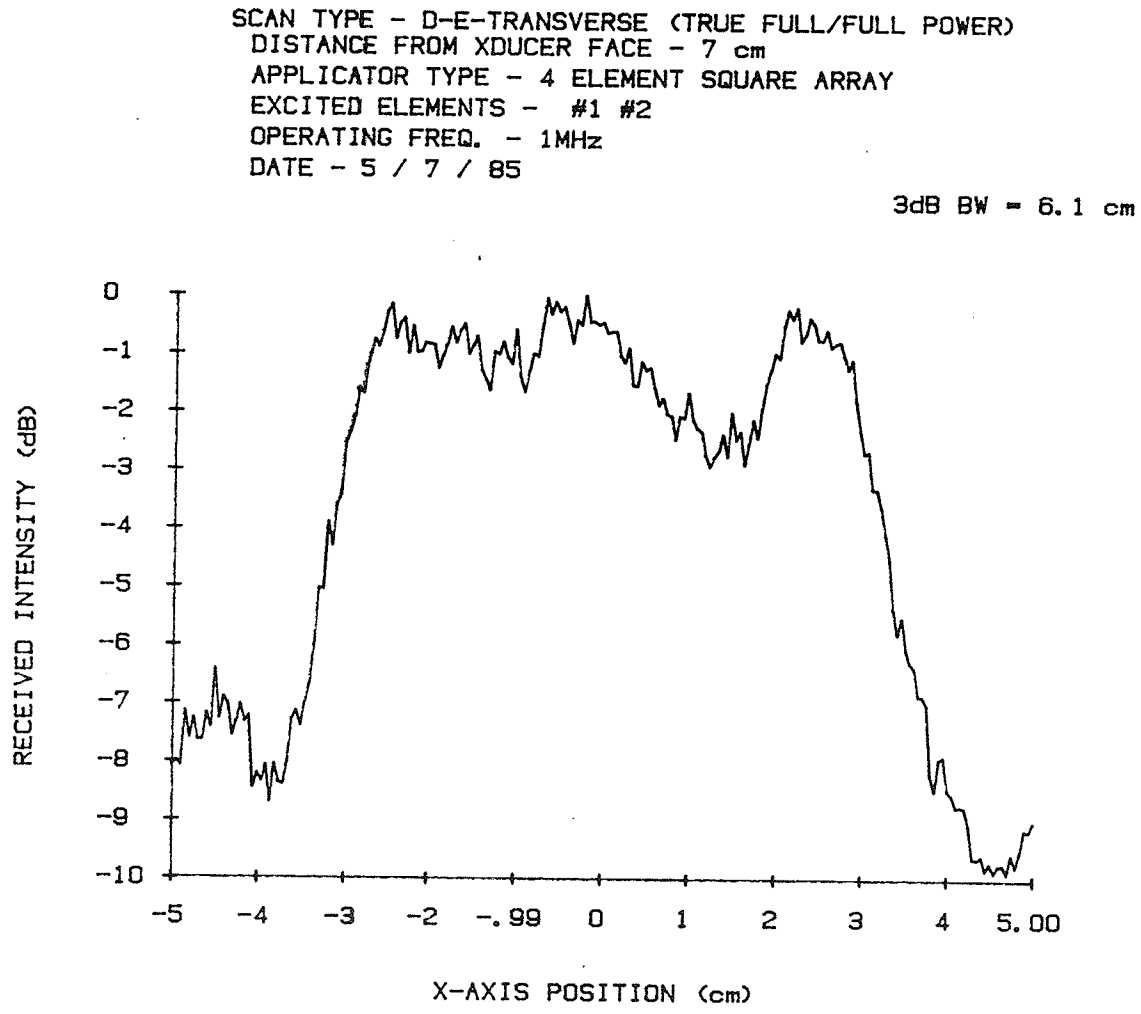

Figure B.10. Transverse relative intensity profile from elements 1 and 2 with compensation.

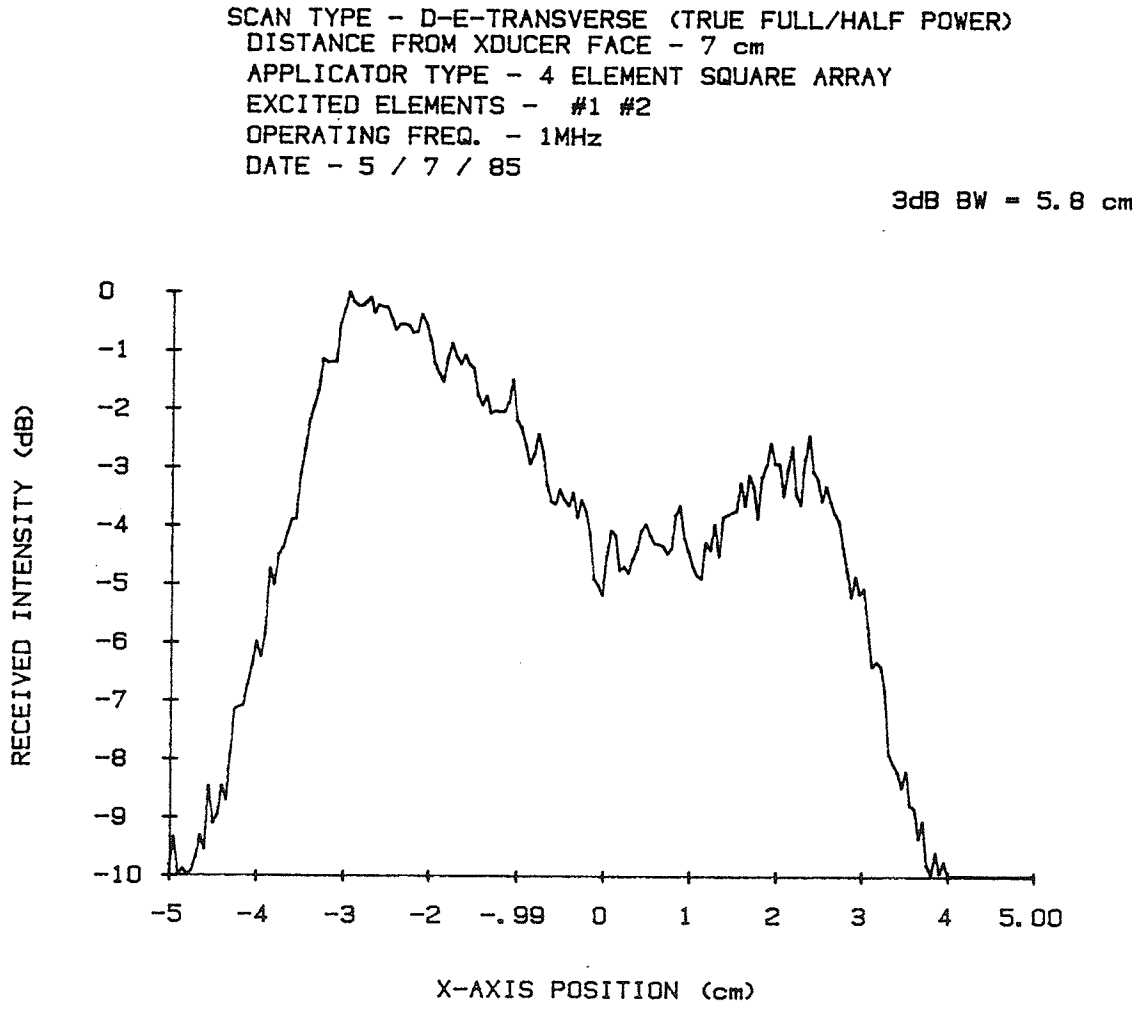

Figure B.11. Transverse relative intensity profile from elements 1 and 2 with compensated power variation.

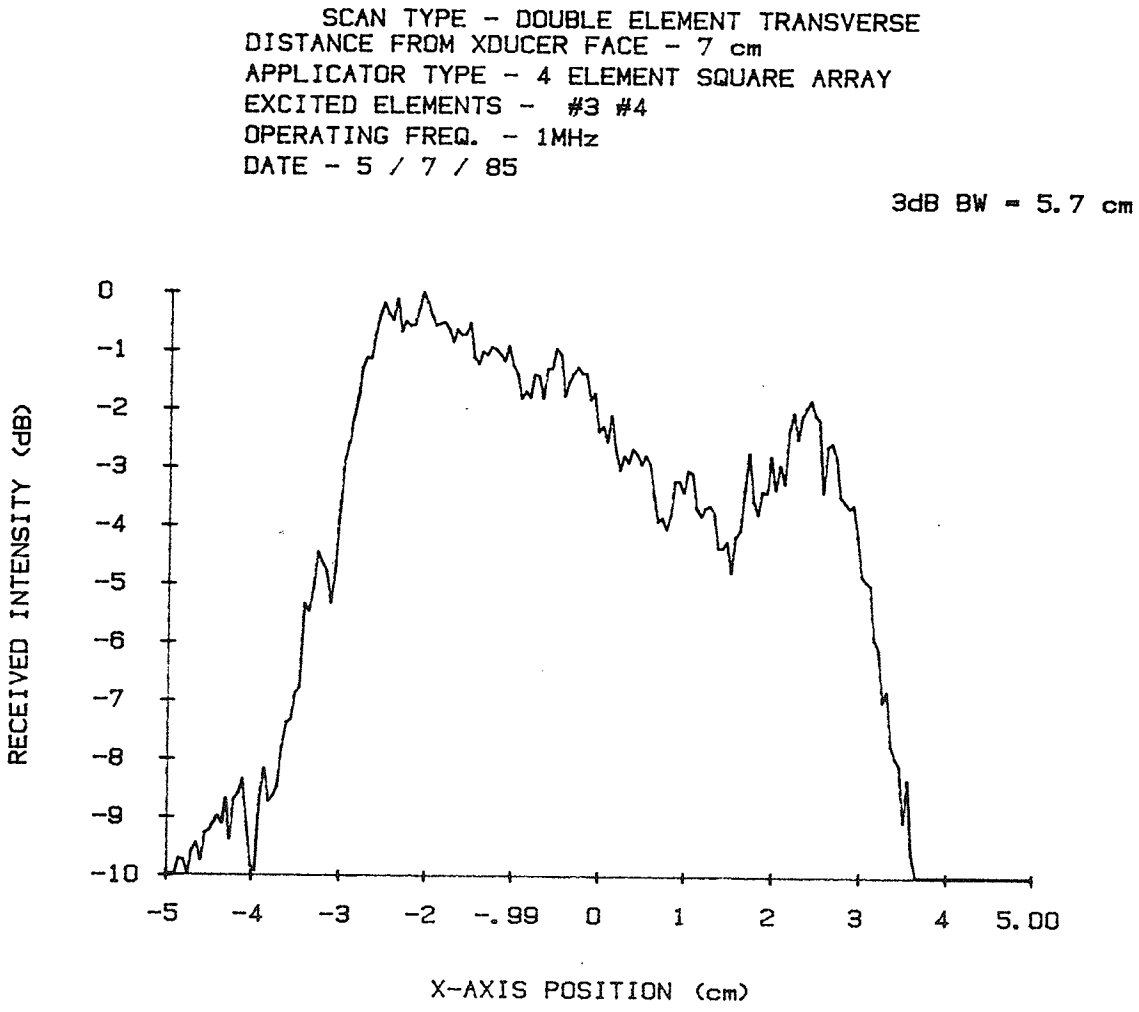

Figure B.12. Transverse relative intensity profile from elements 3 and 4.

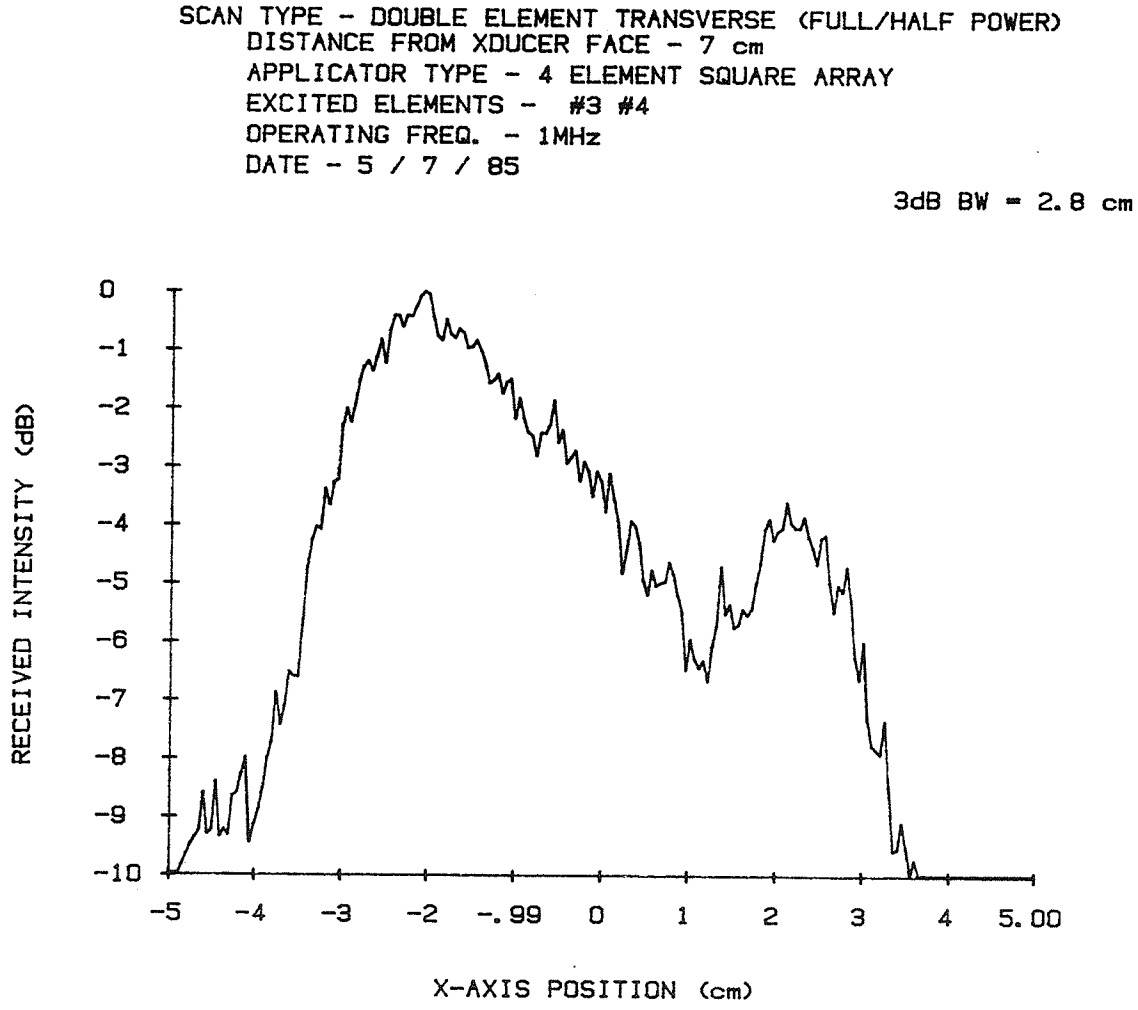

Figure B.13. Transverse relative intensity profile from elements 3 and 4 with power variation.

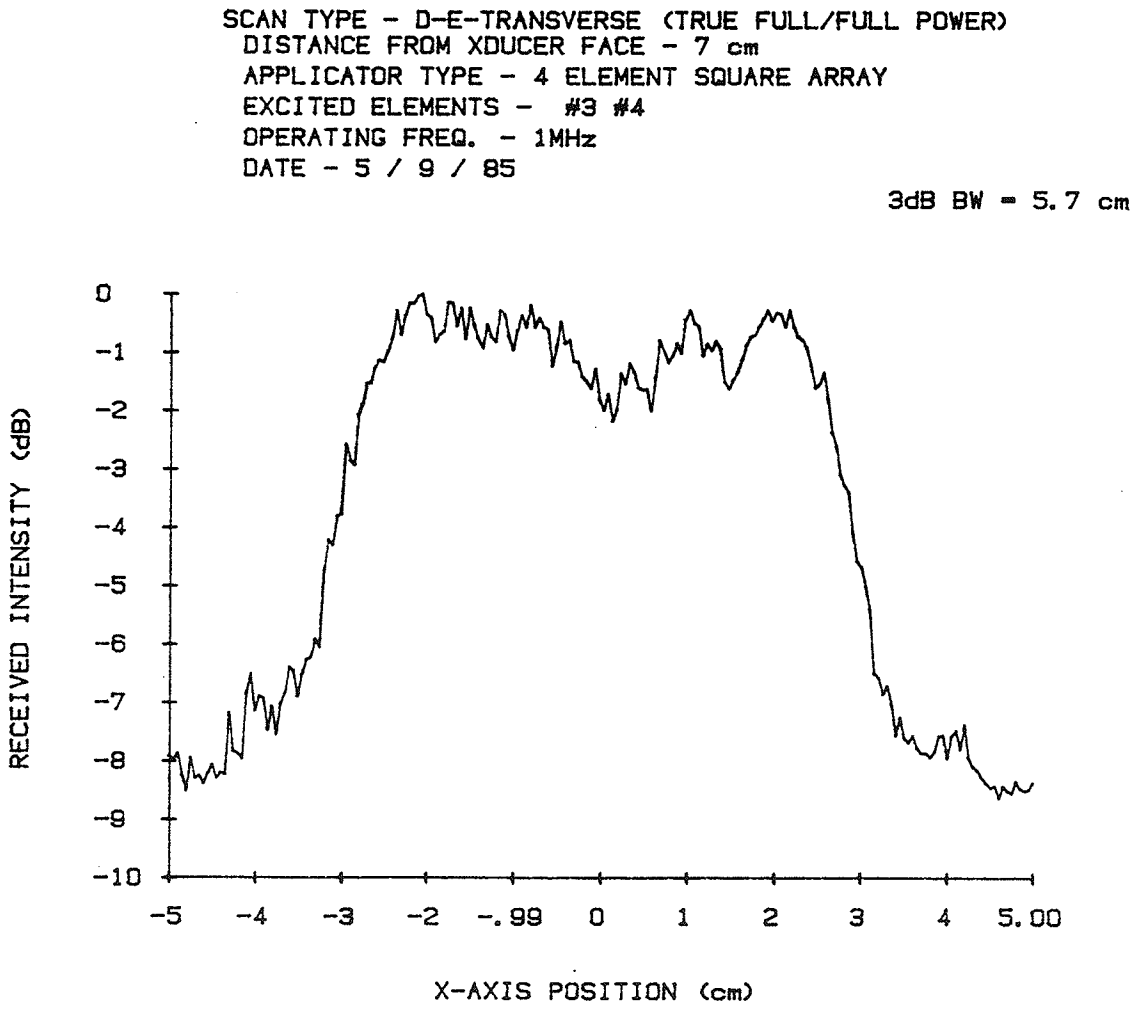

Figure B.14. Transverse relative intensity profile from elements 3 and 4 with compensation.

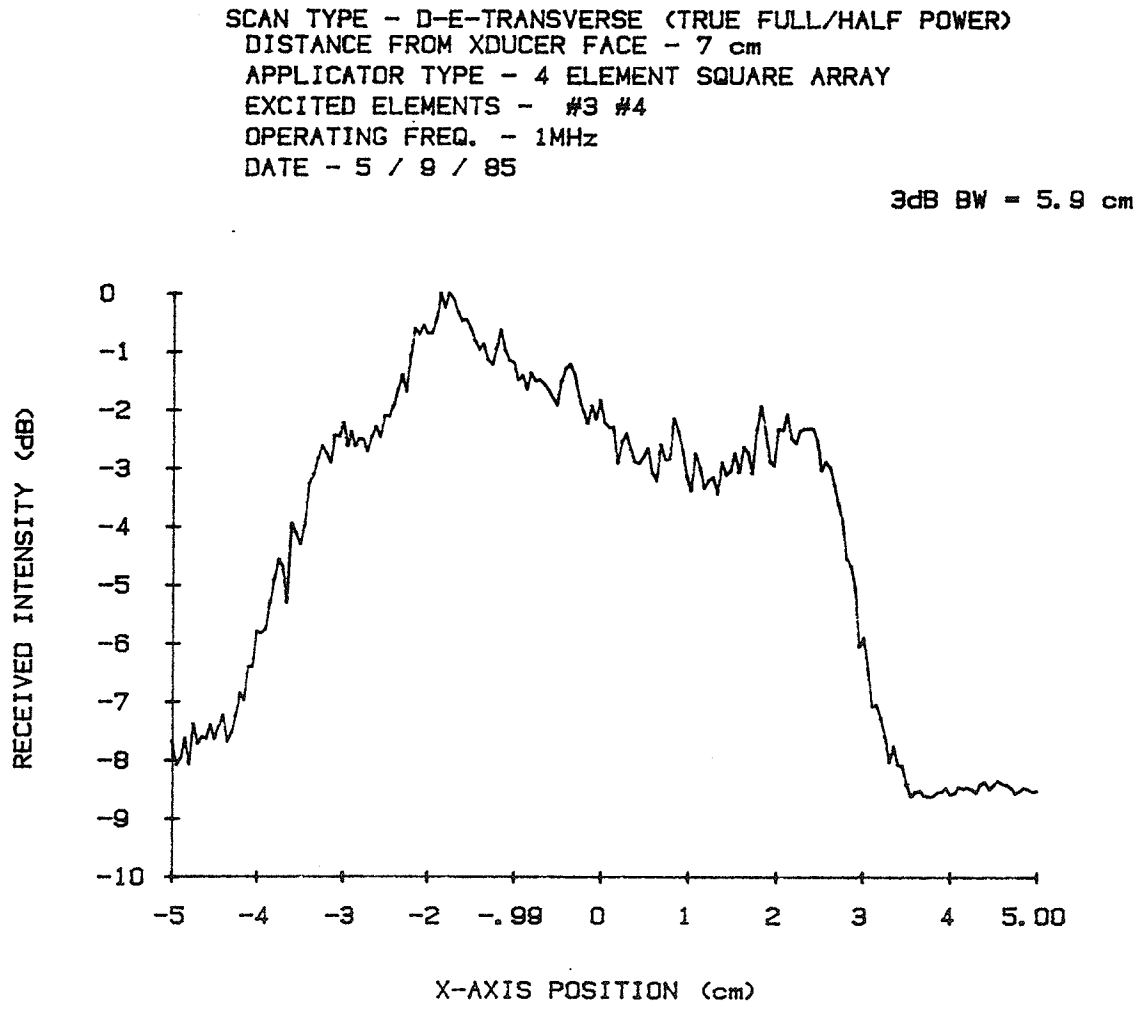

Figure B.15. Transverse relative intensity profile from elements 3 and 4 with compensated power variation.

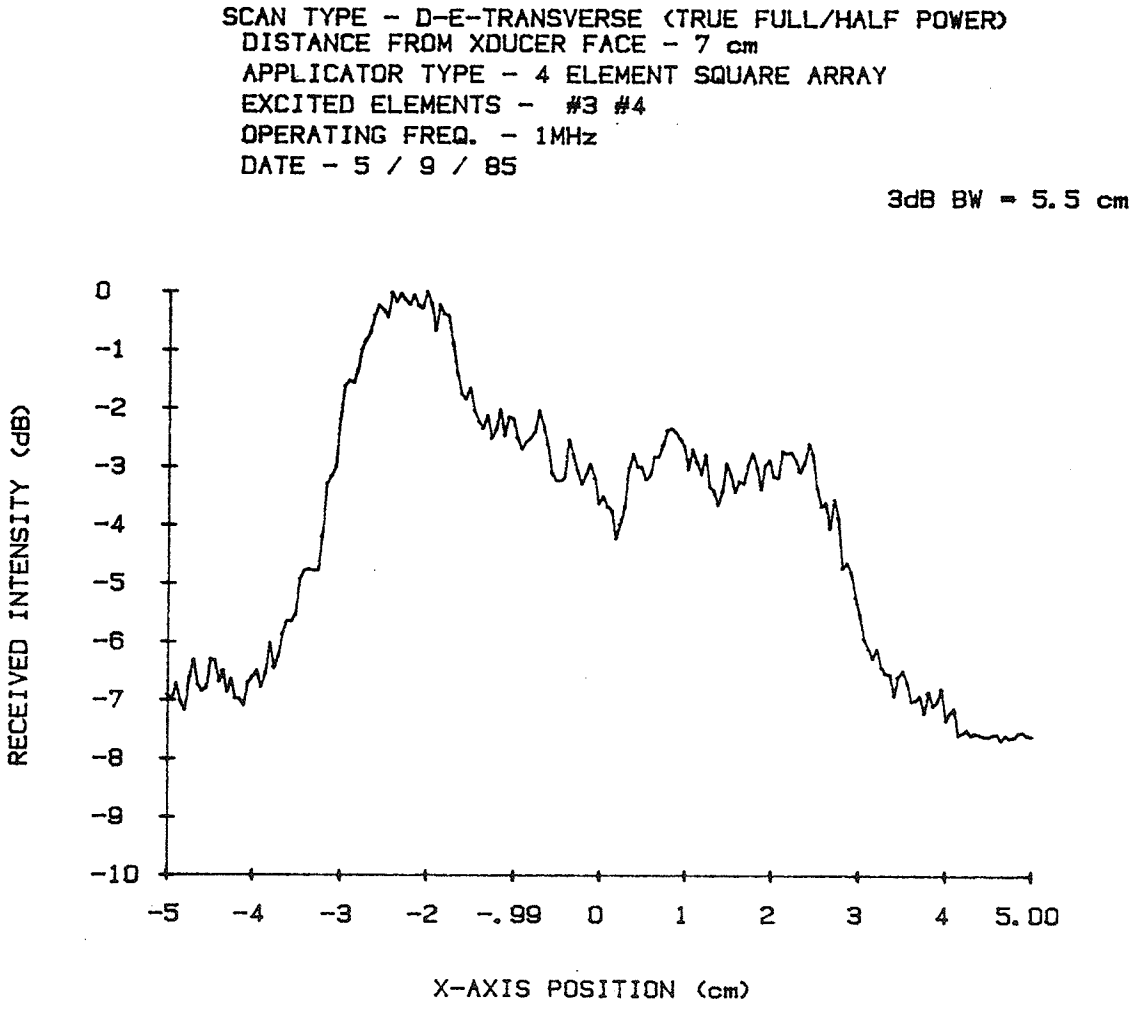

Figure B.16. Transverse relative intensity profile from elements 3 and 4 with compensated power variation at 993 kHz.

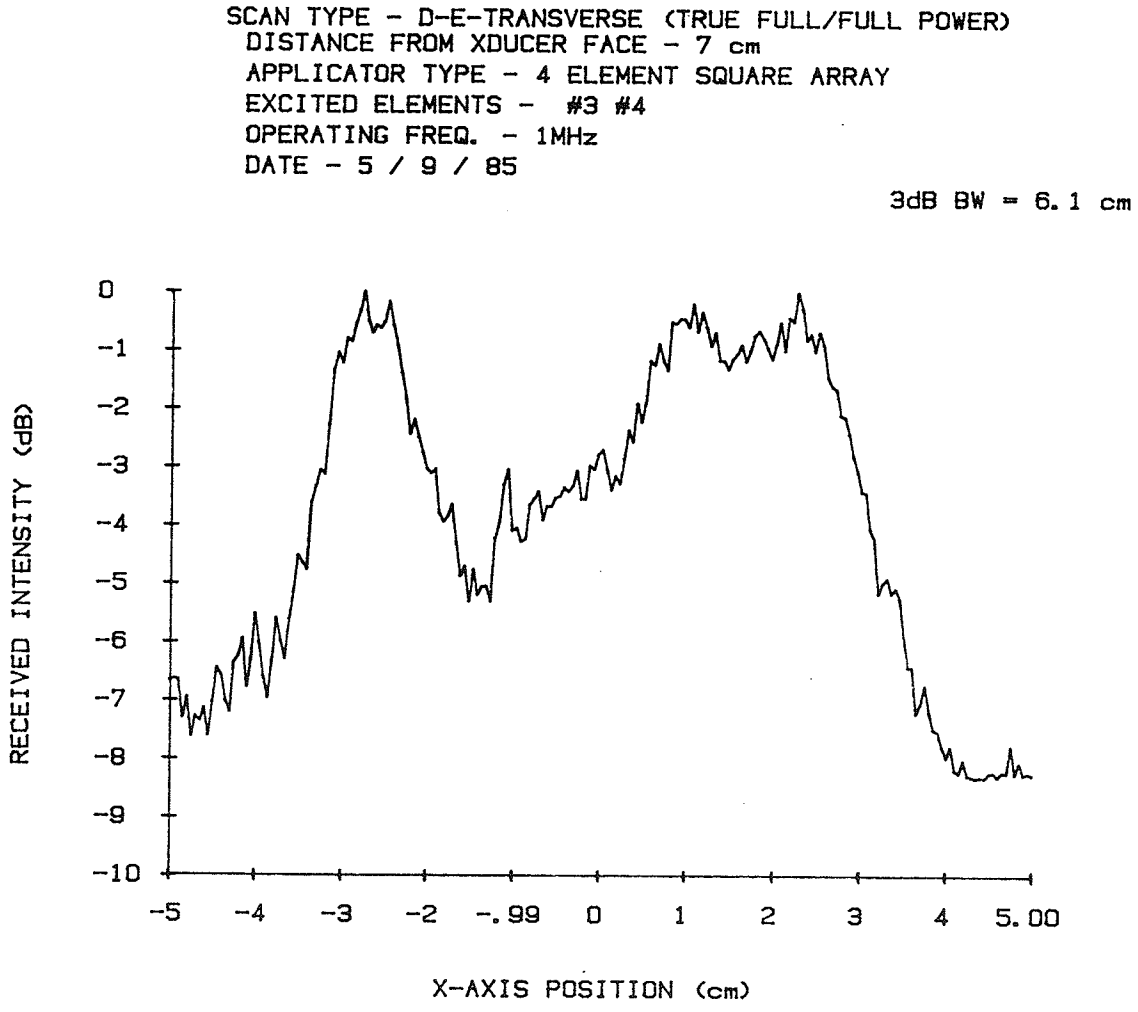

Figure B.17. Transverse relative intensity profile from elements 3 and 4 with compensation at 993 kHz.

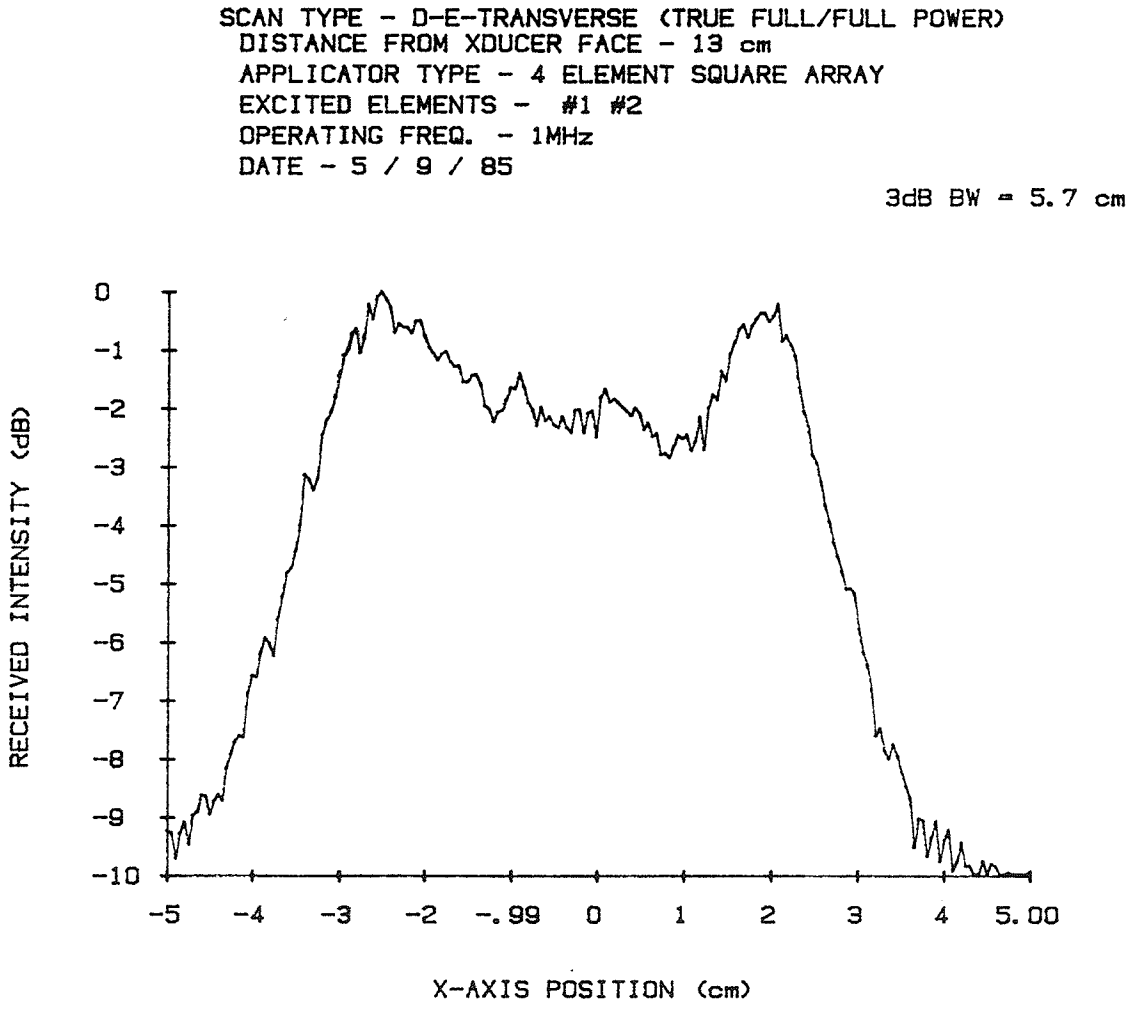

Figure B.18. Transverse relative intensity profile from elements 1 and 2 with compensation at z = 13.0 cm.

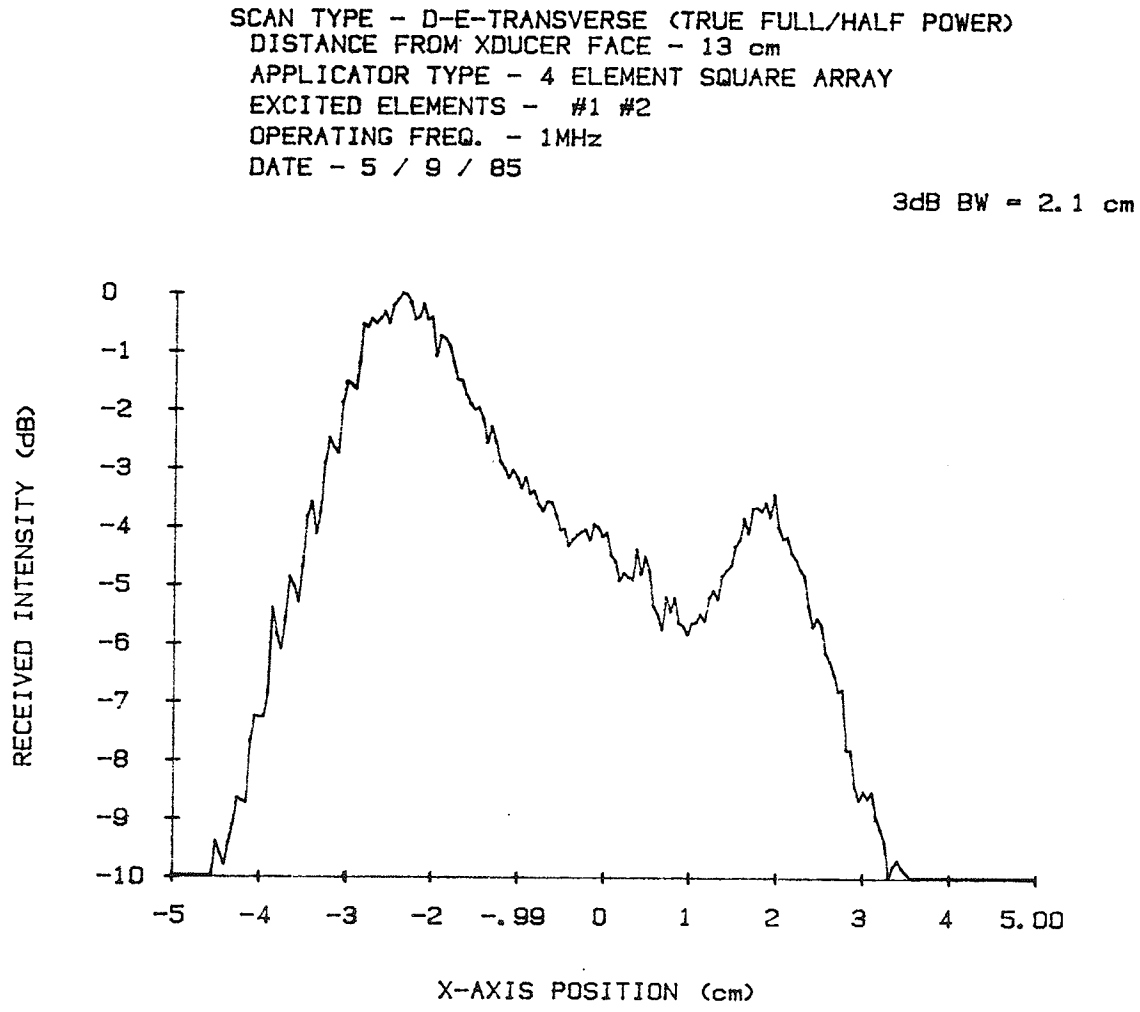

Figure B.19. Transverse relative intensity profile from elements 1 and 2 with compensated power variation at z = 13.0 cm.

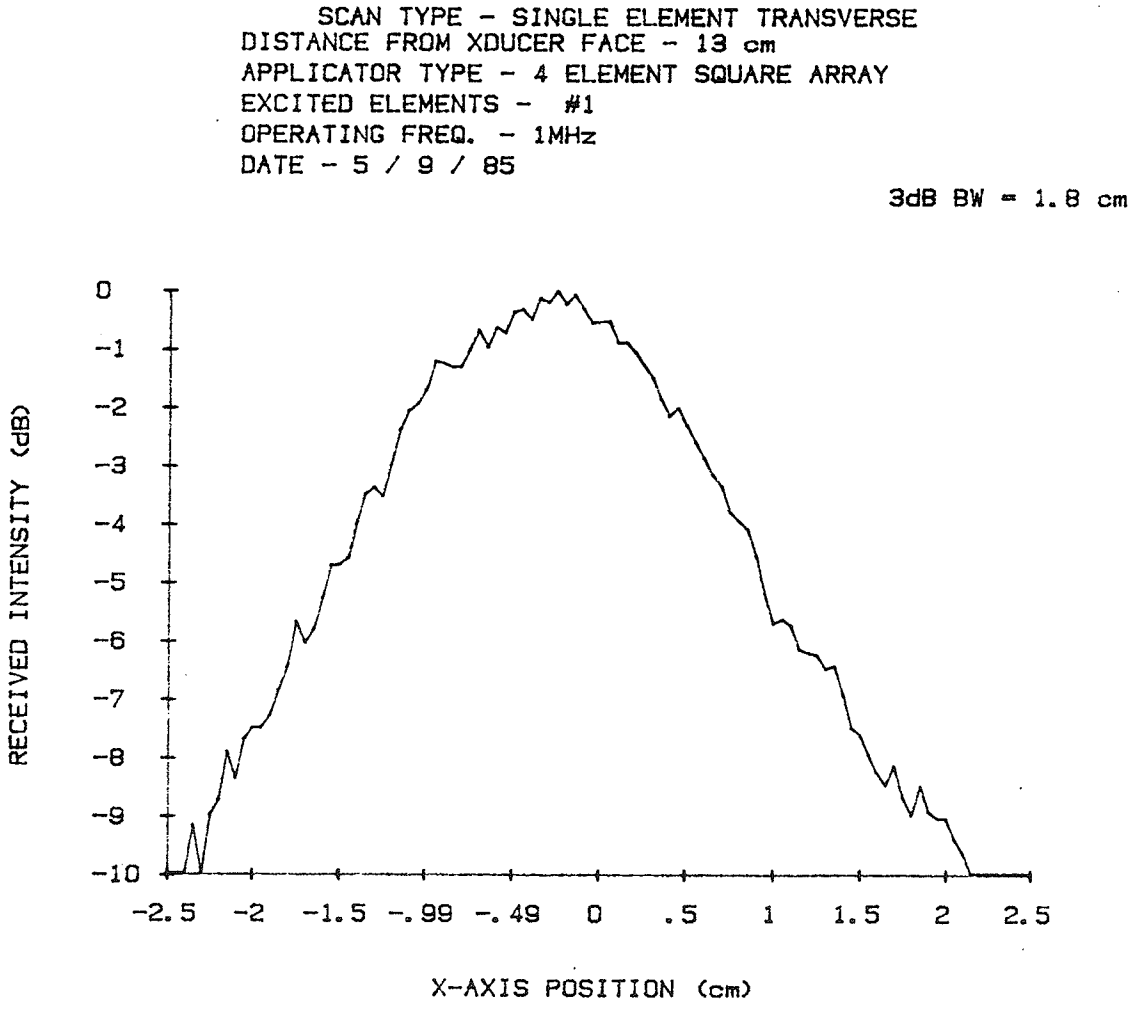

Figure B.20. Transverse relative intensity profile from element 1 at z = 13.0 cm.

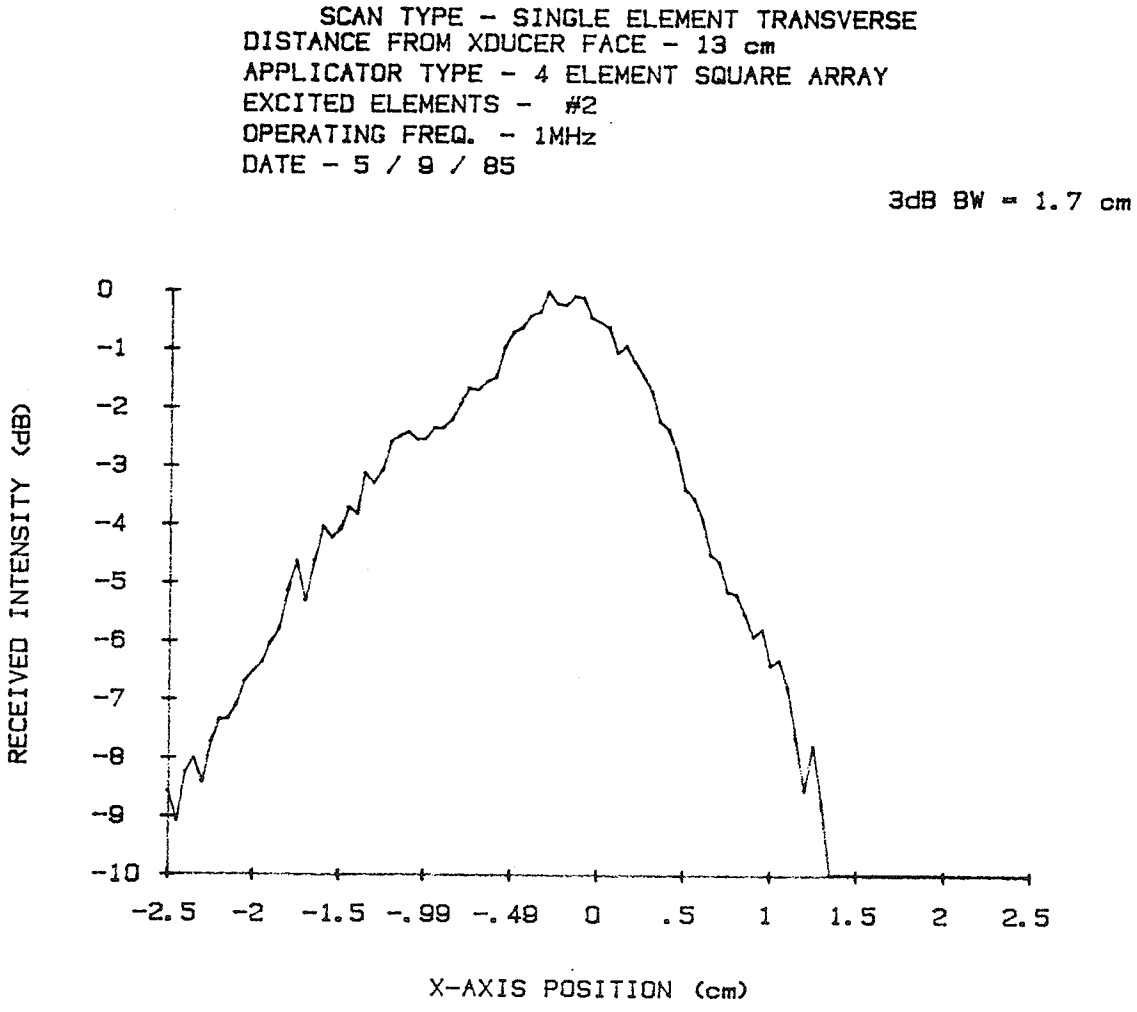

Figure B.21. Transverse relative intensity profile from element 2 at z = 13.0 cm.

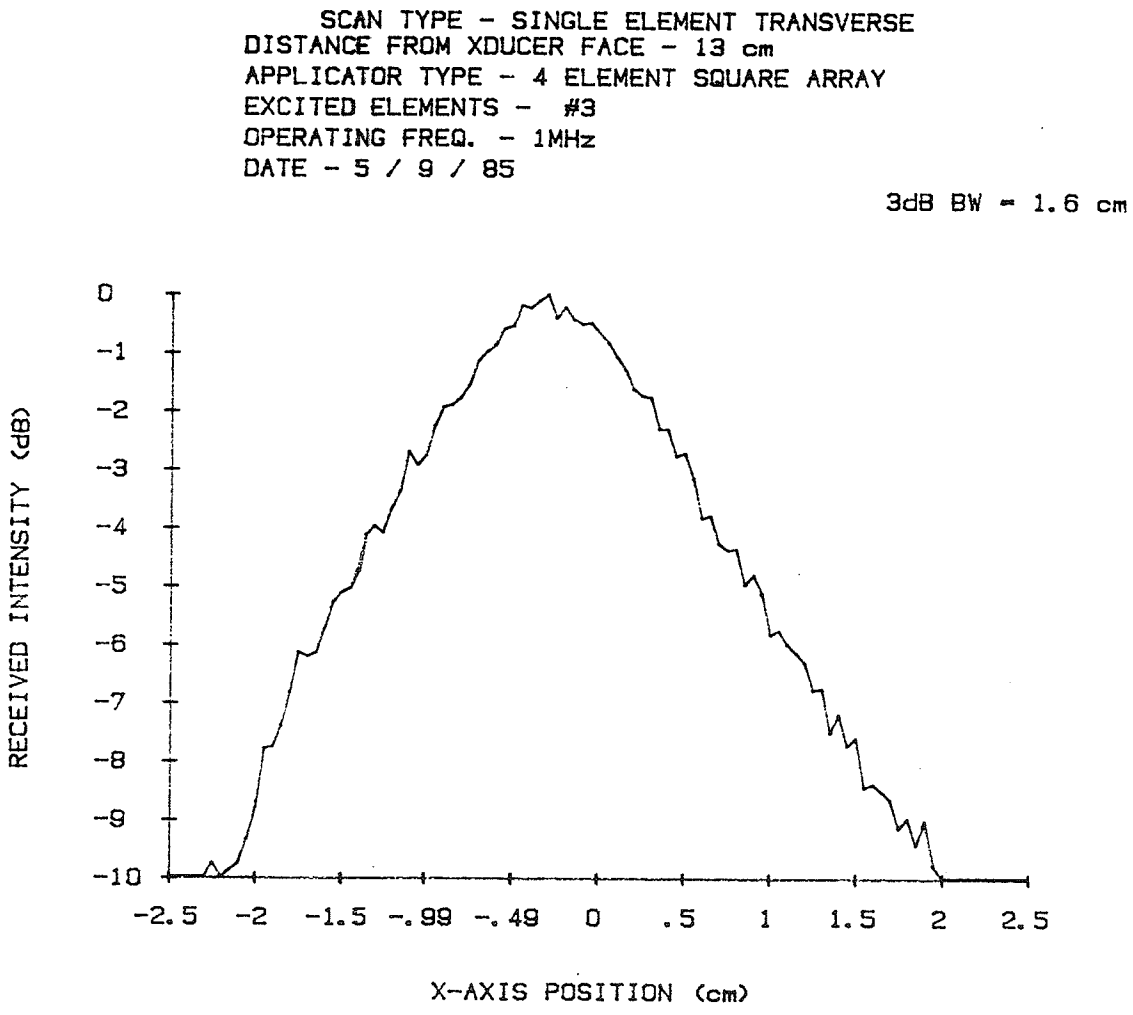

Figure B.22. Transverse relative intensity profile from element 3 at z = 13.0 cm and 997 kHz.

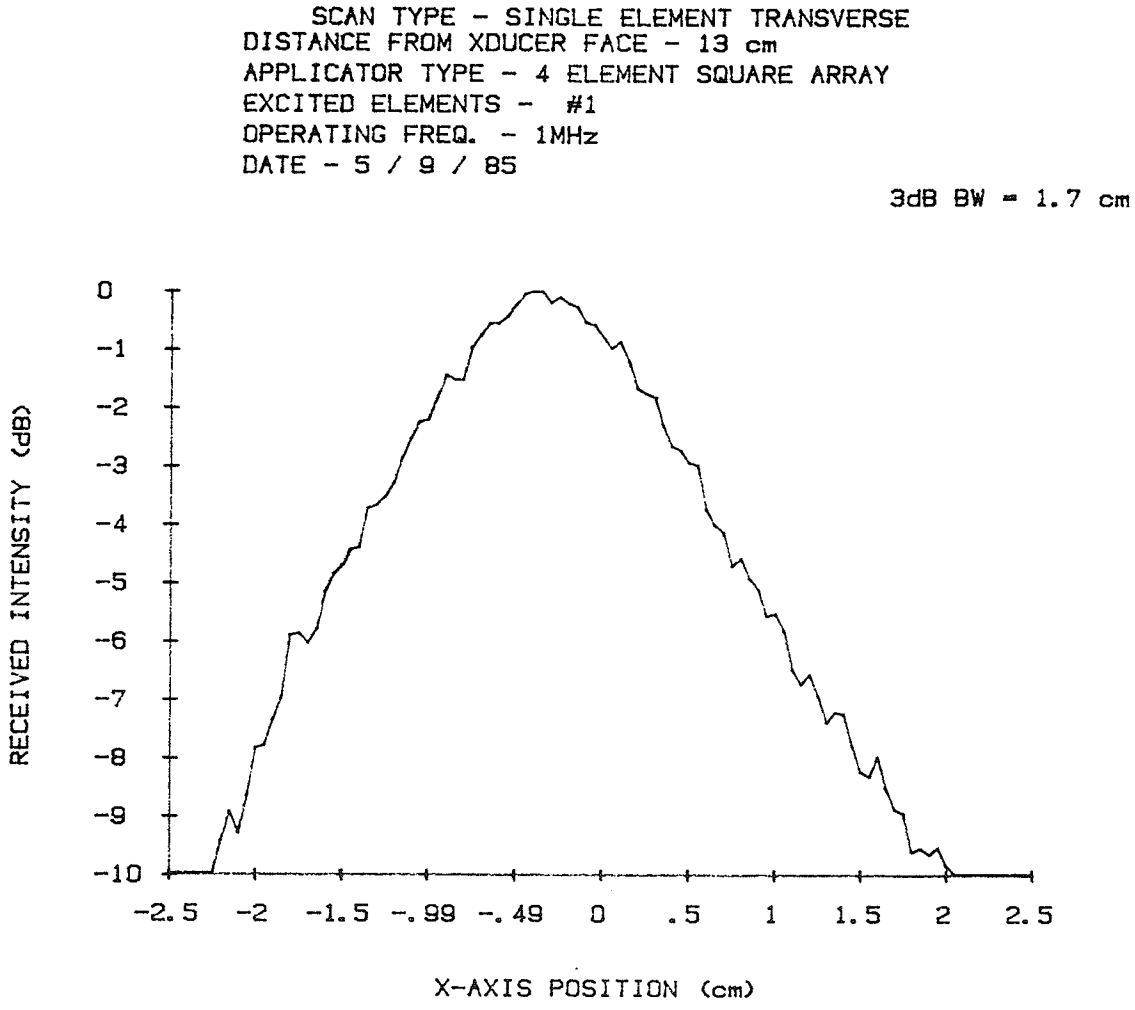

Figure B.23. Transverse relative intensity profile from element 3 at z = 13.0 cm.

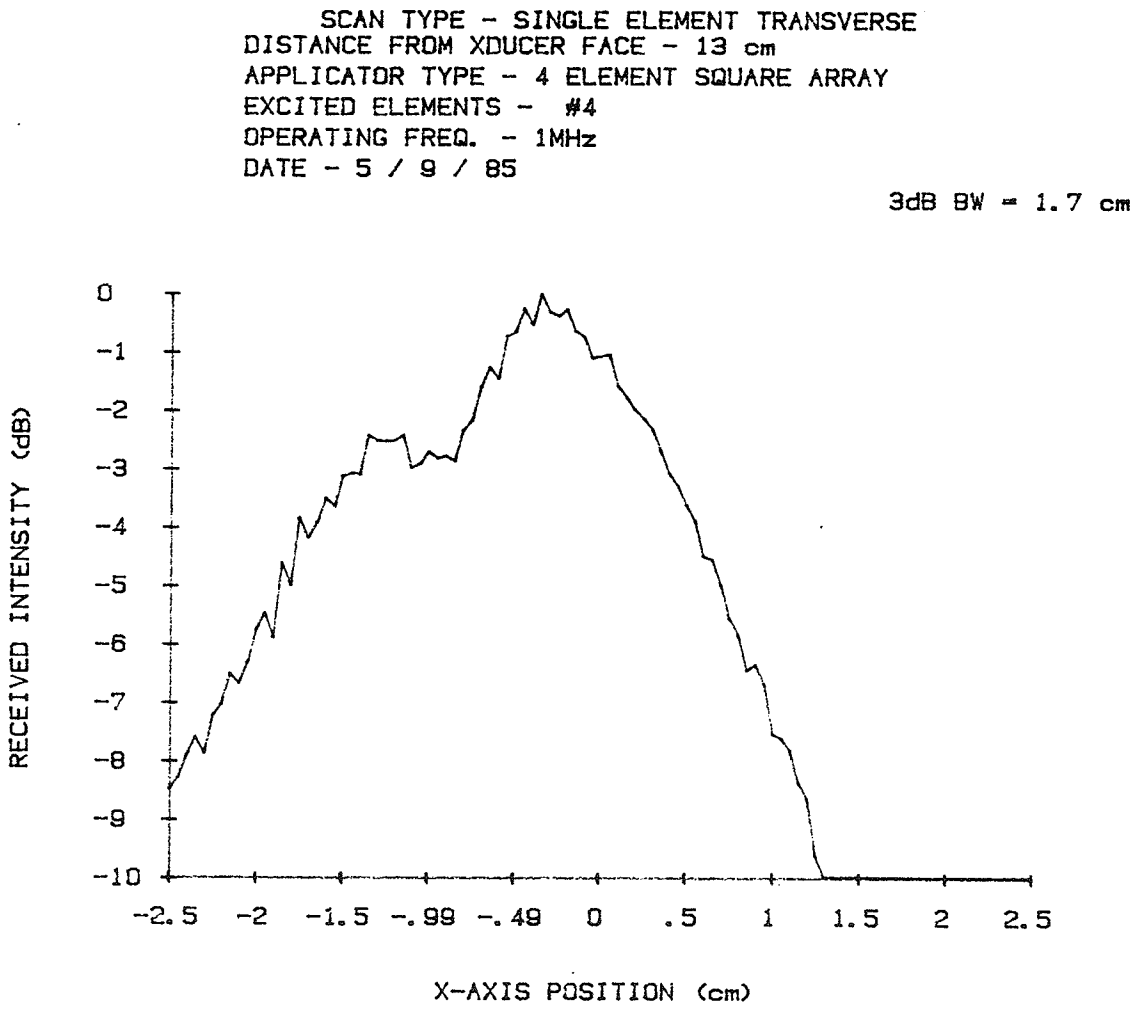

Figure B.24. Transverse relative intensity profile from element 4 at z = 13.0 cm.

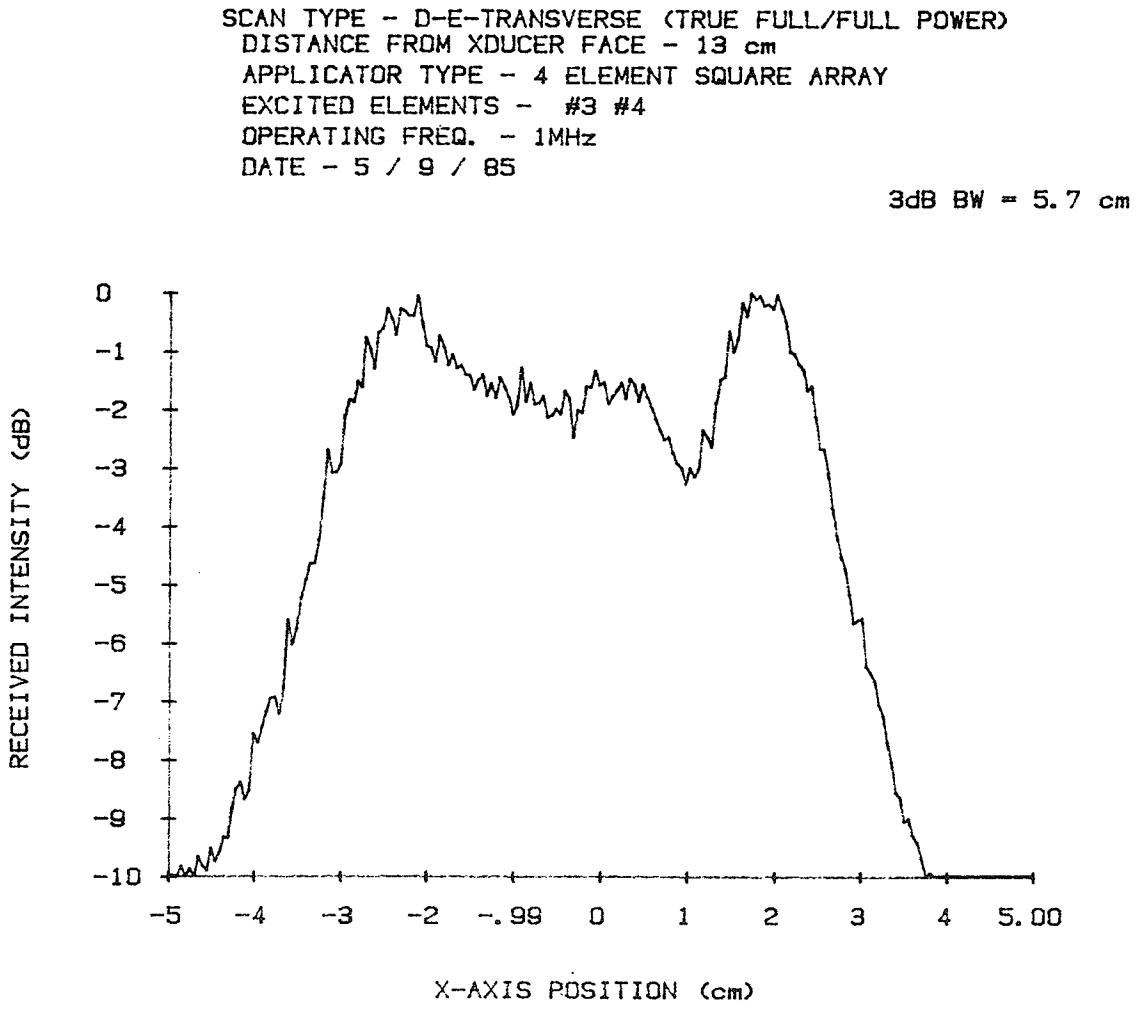

Figure B.25. Transverse relative intensity profile from elements 3 and 4 with compensation.

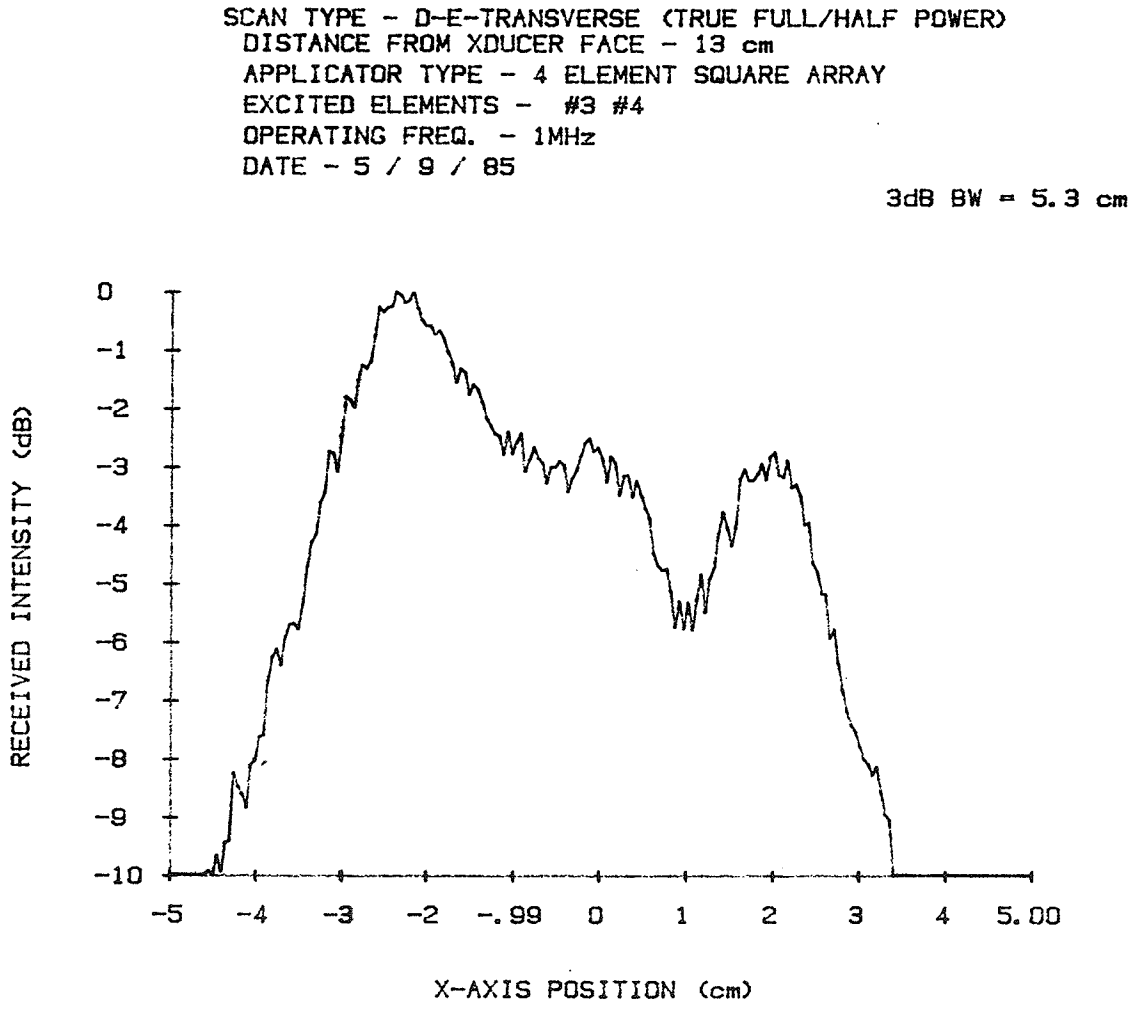

Figure B.26. Transverse relative intensity profile from elements 3 and 4 with compensated power variation.

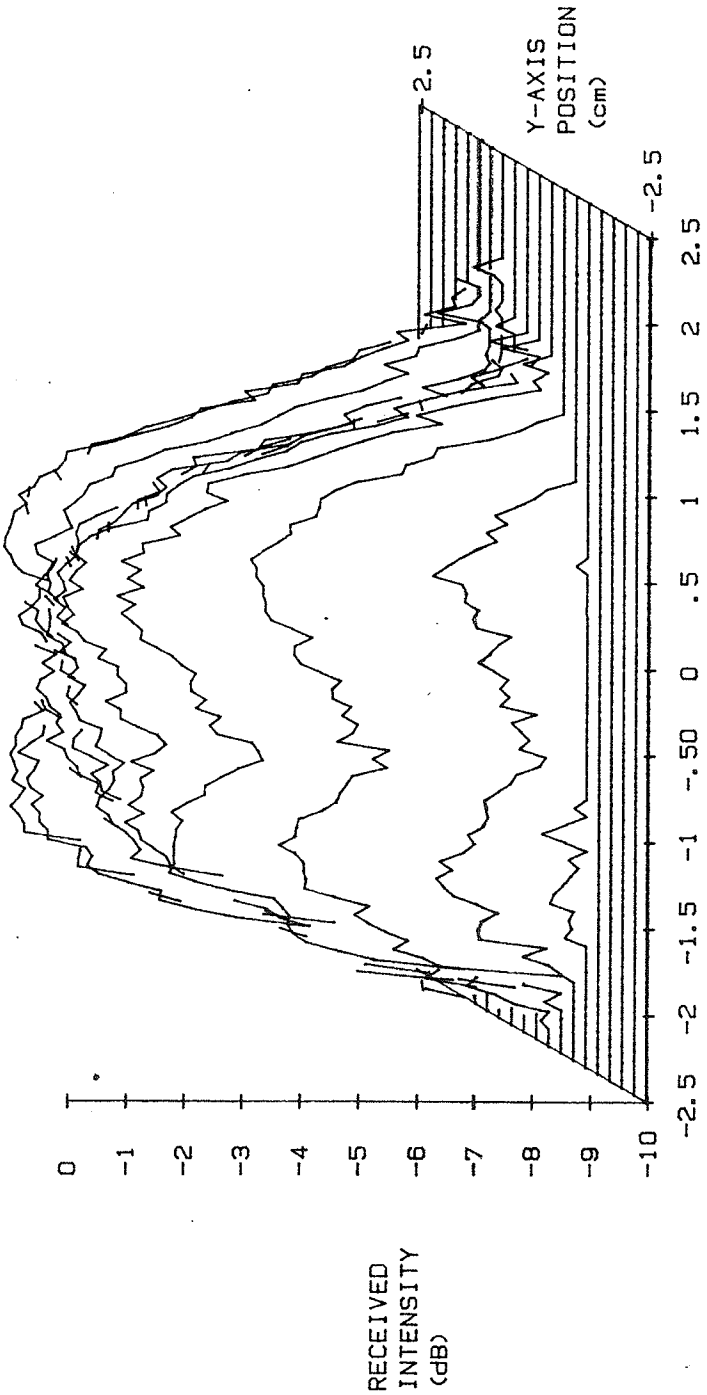

Figure B.27. Three-dimensional view of multiple transverse relative intensity scans from a single transducer element.

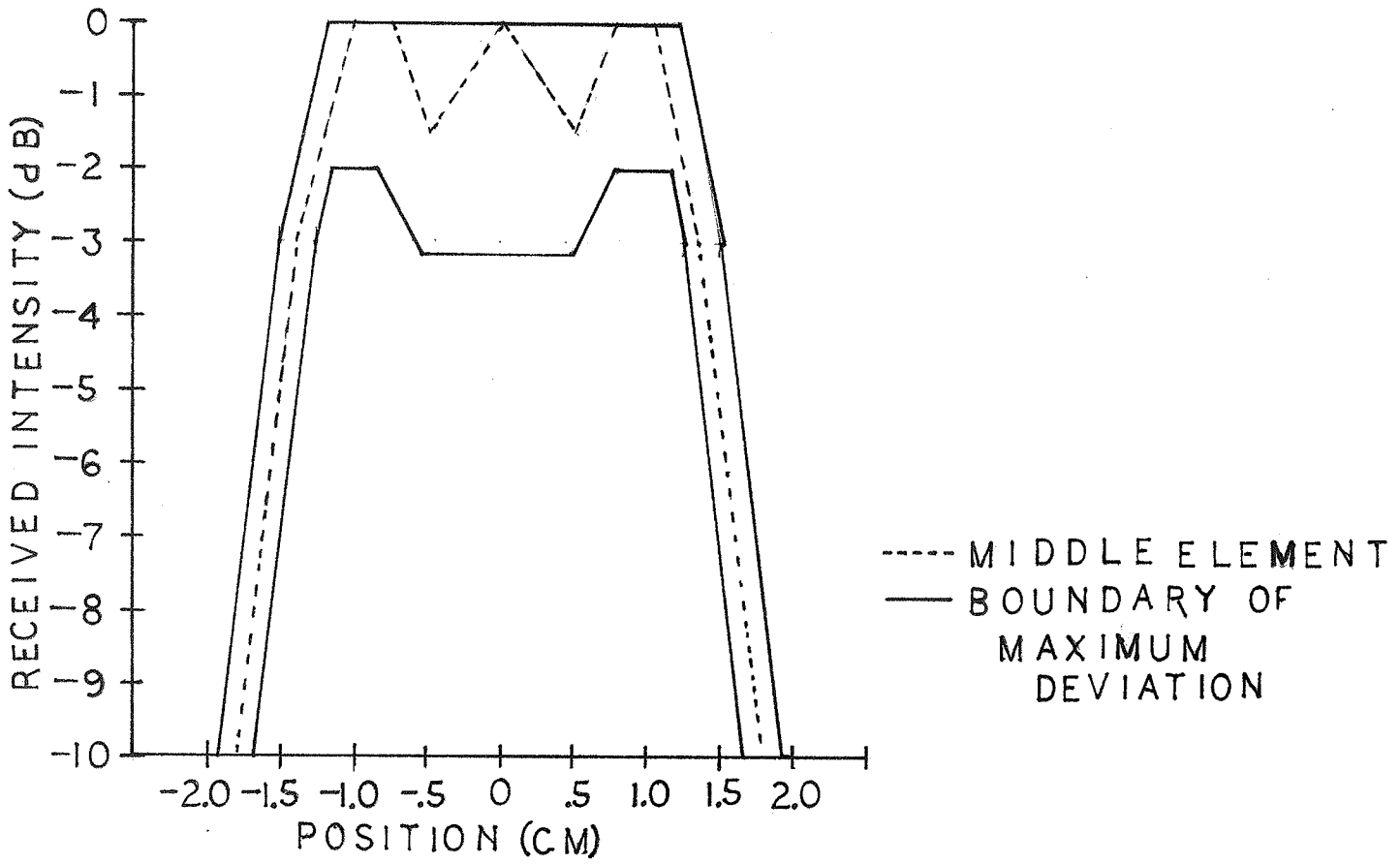

Figure B.28. Typical middle-element beam profile with average 3 dB width, average ripple amplitude and maximum range of deviation for an arbitrary element from the 16-element square array.

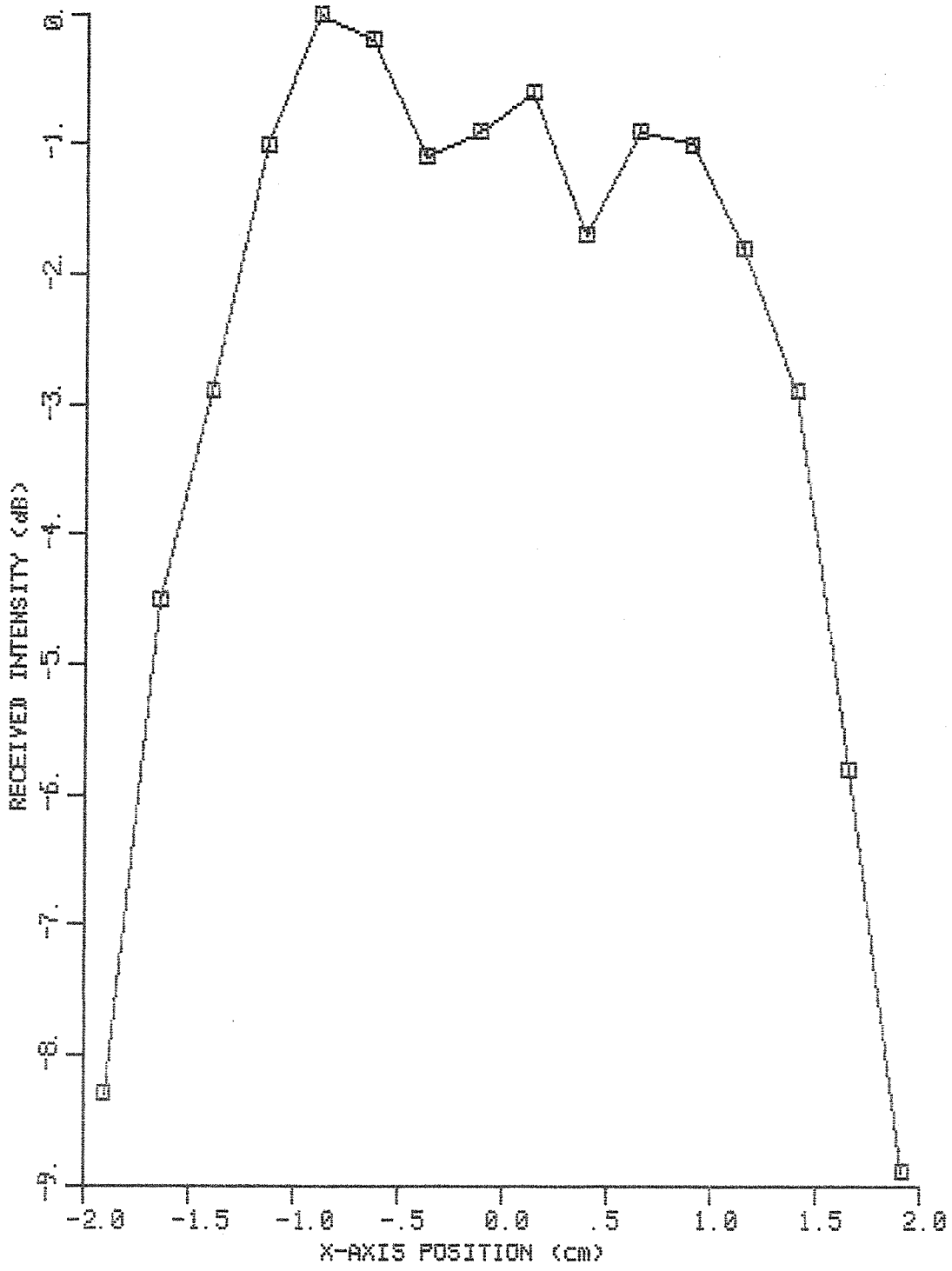

Figure B.29. Intensity profile for an edge element (element 5) of the 16-element applicator.

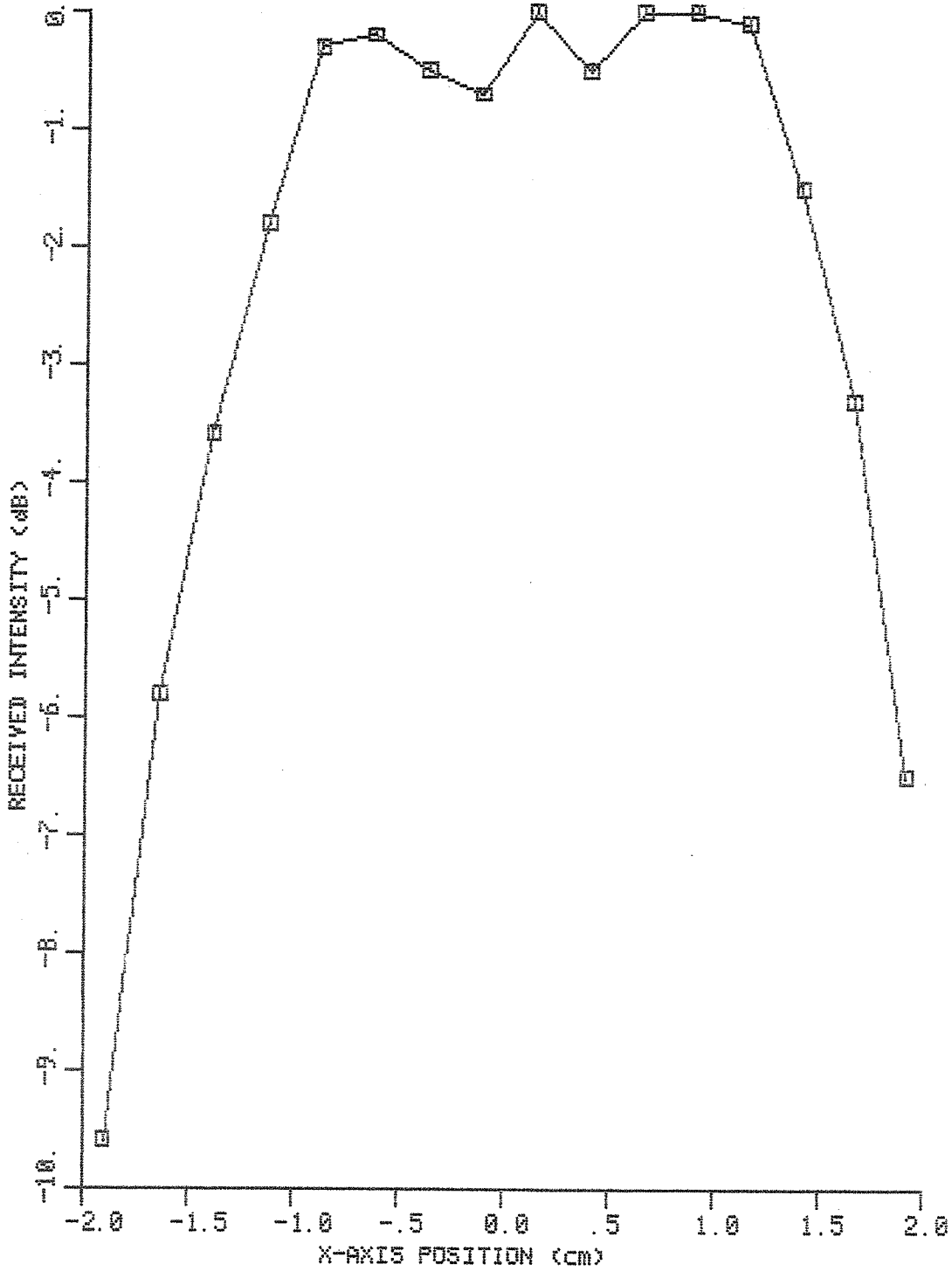

Figure B.30. Intensity profile for a middle element (element 6) of the 16-element applicator

APPENDIX C

SIMULATIONS WITH AN IMPROVED MODEL

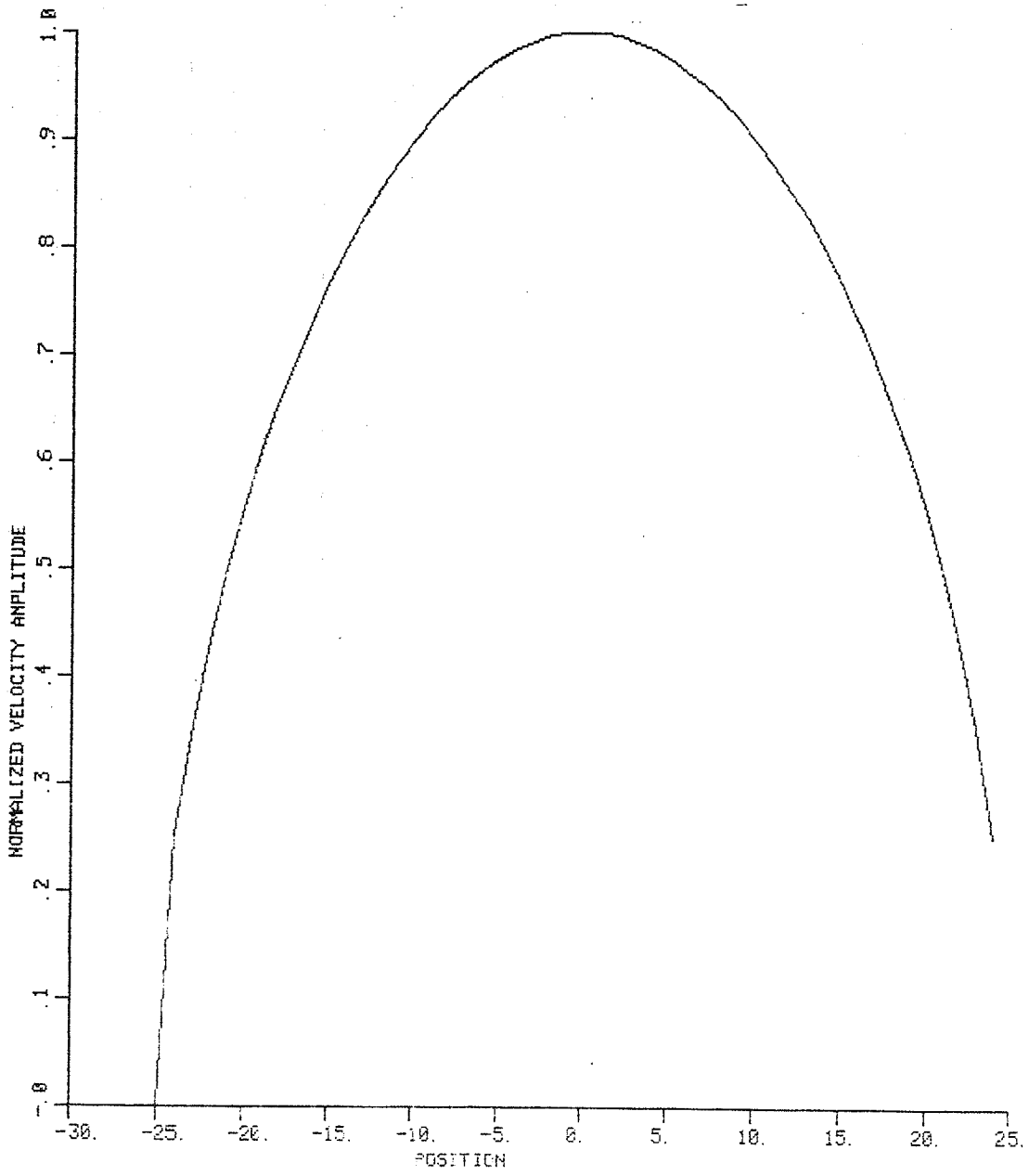

Figure C.1. Nonuniform velocity amplitude profile of a transducer element with n = 2.

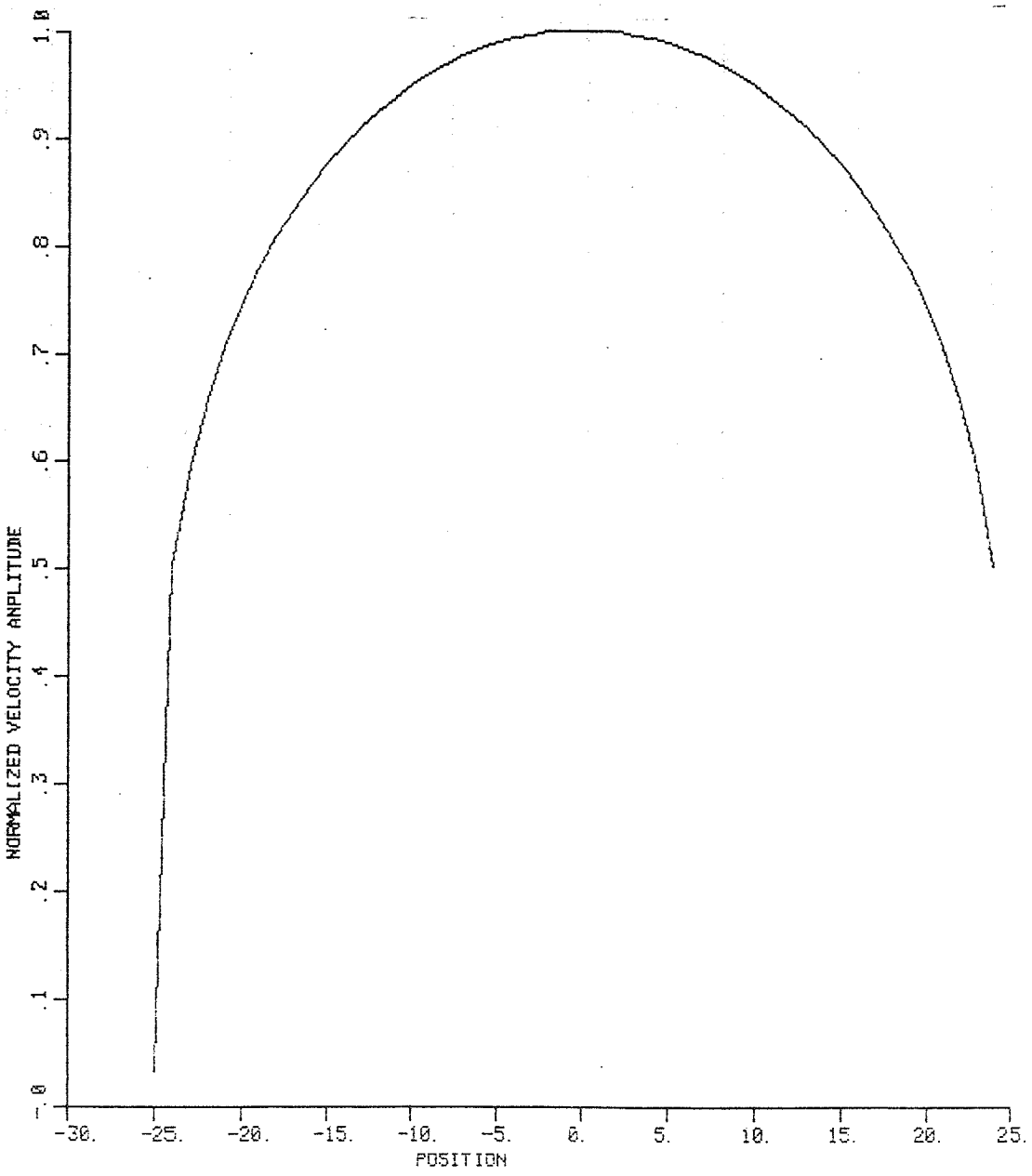

Figure C.2. Nonuniform velocity amplitude profile of a transducer element with n = 4.

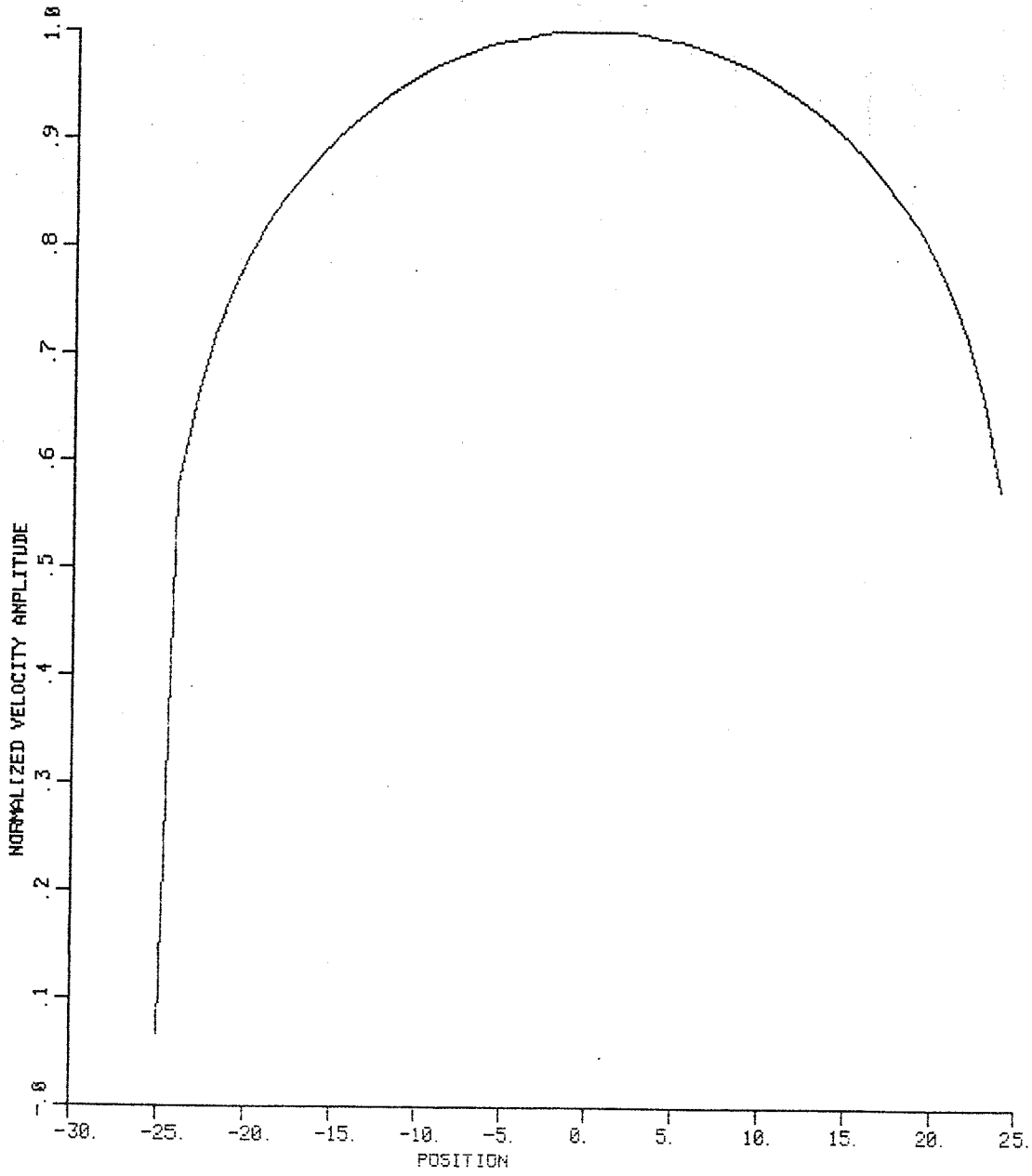

Figure C.3. Nonuiform velocity amplitude profile of a transducer element with n = 5.

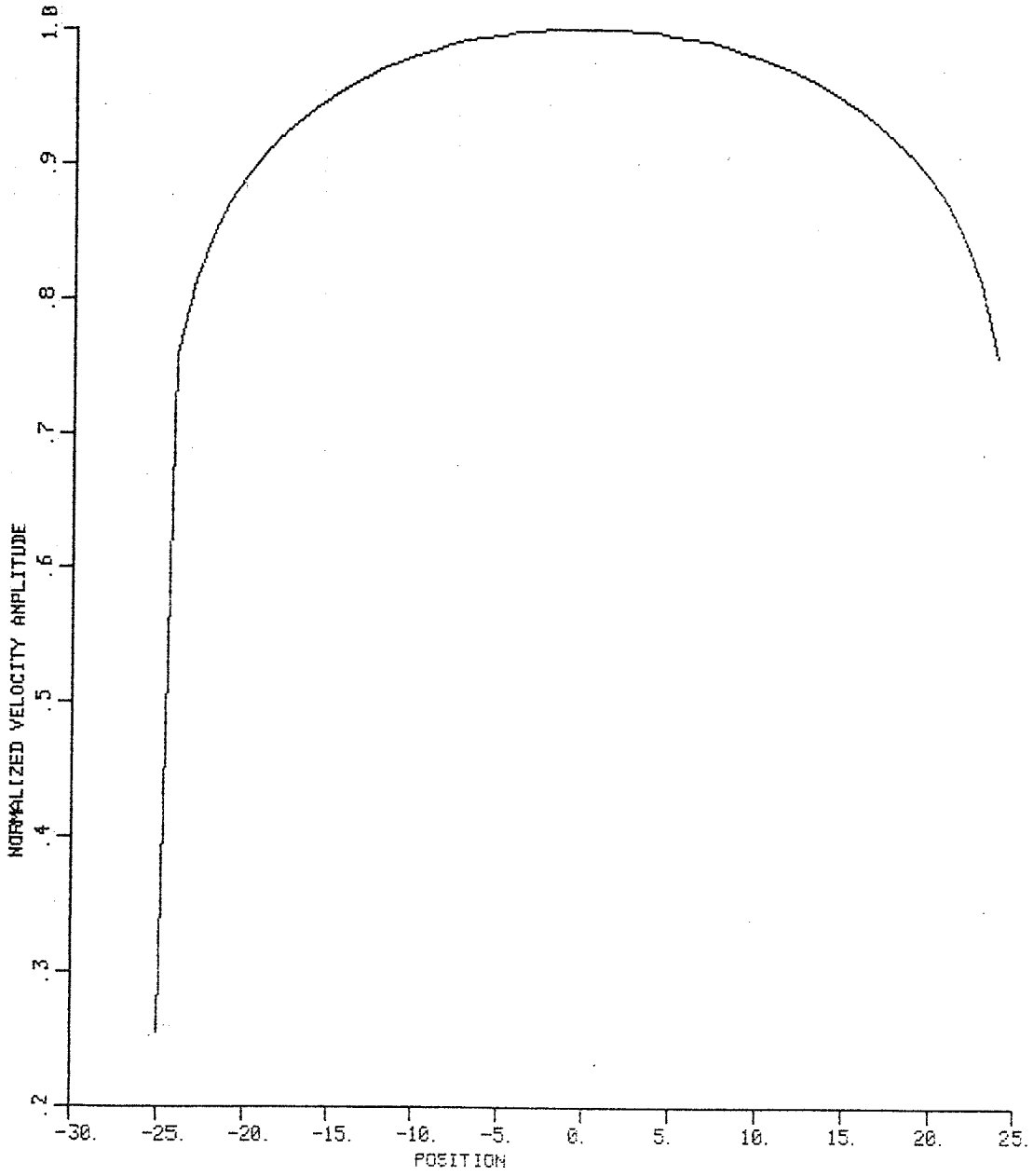

Figure C.4. Nonuniform velocity amplitude profile of a transducer element with n = 10.

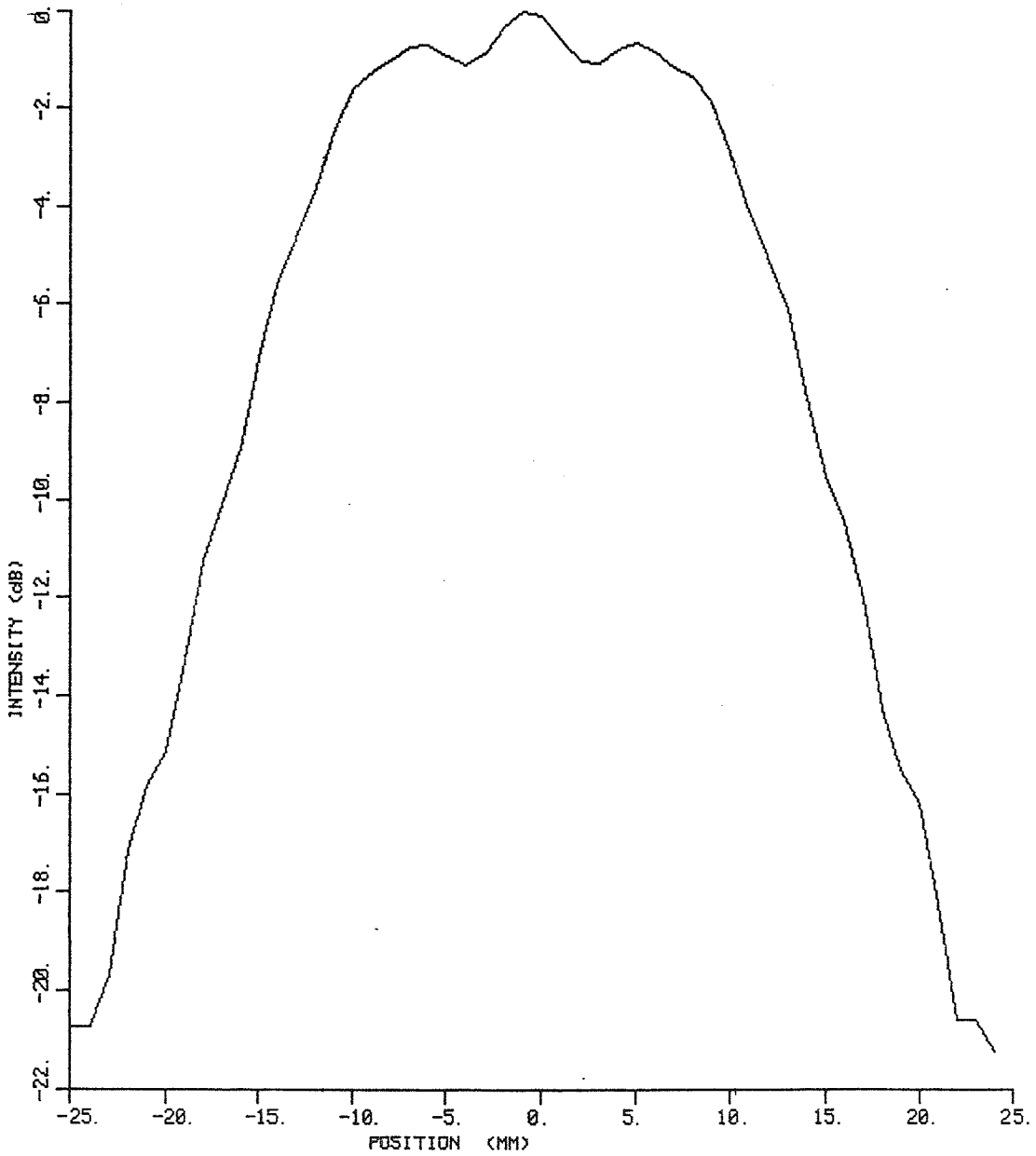

Figure C.5. Simulated transverse relative intensity at z = 7.0 cm from a single element with n = 2.

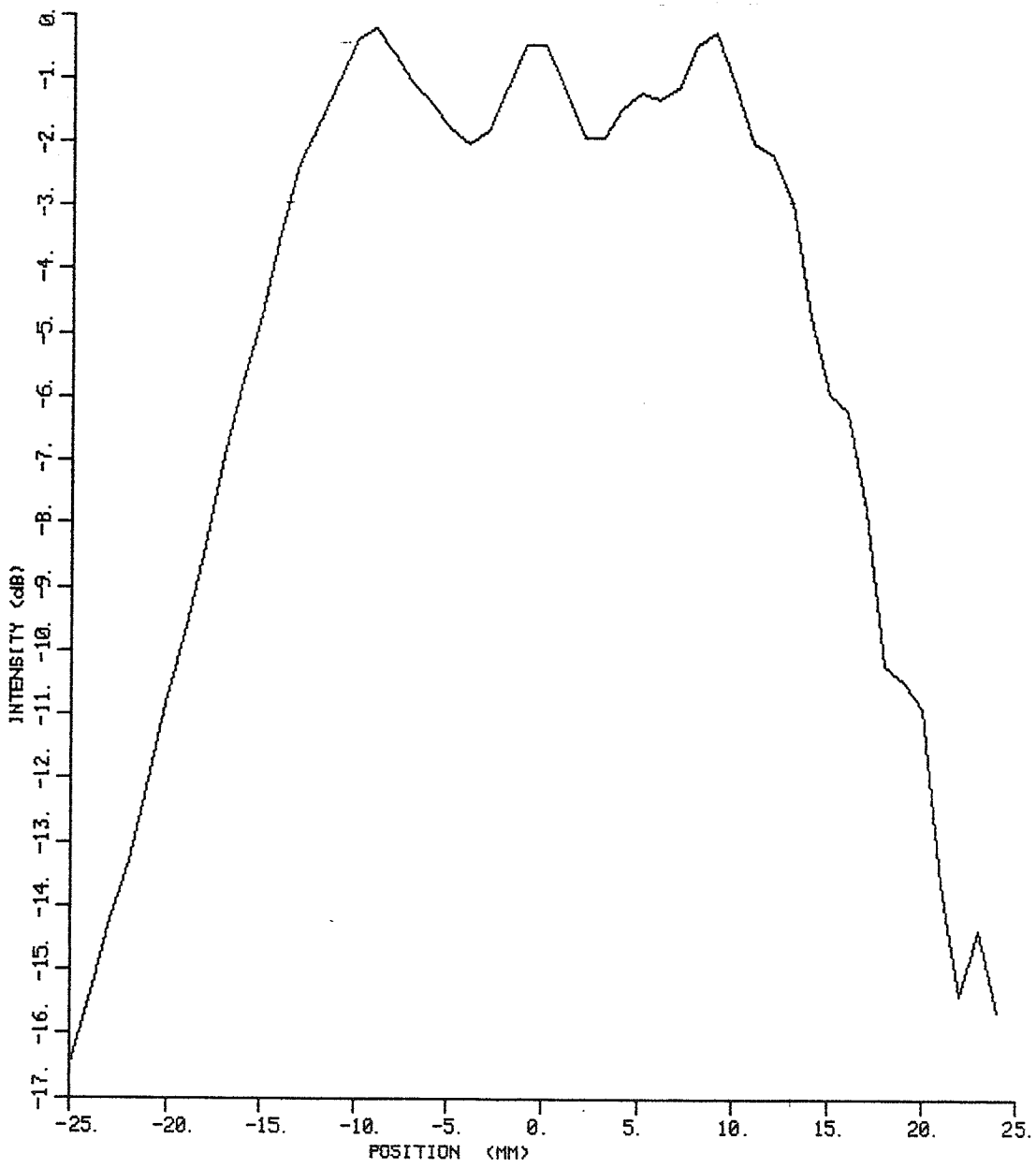

Figure C.6. Simulated transverse relative intensity at z = 7.0 cm from a single element with n = 10.

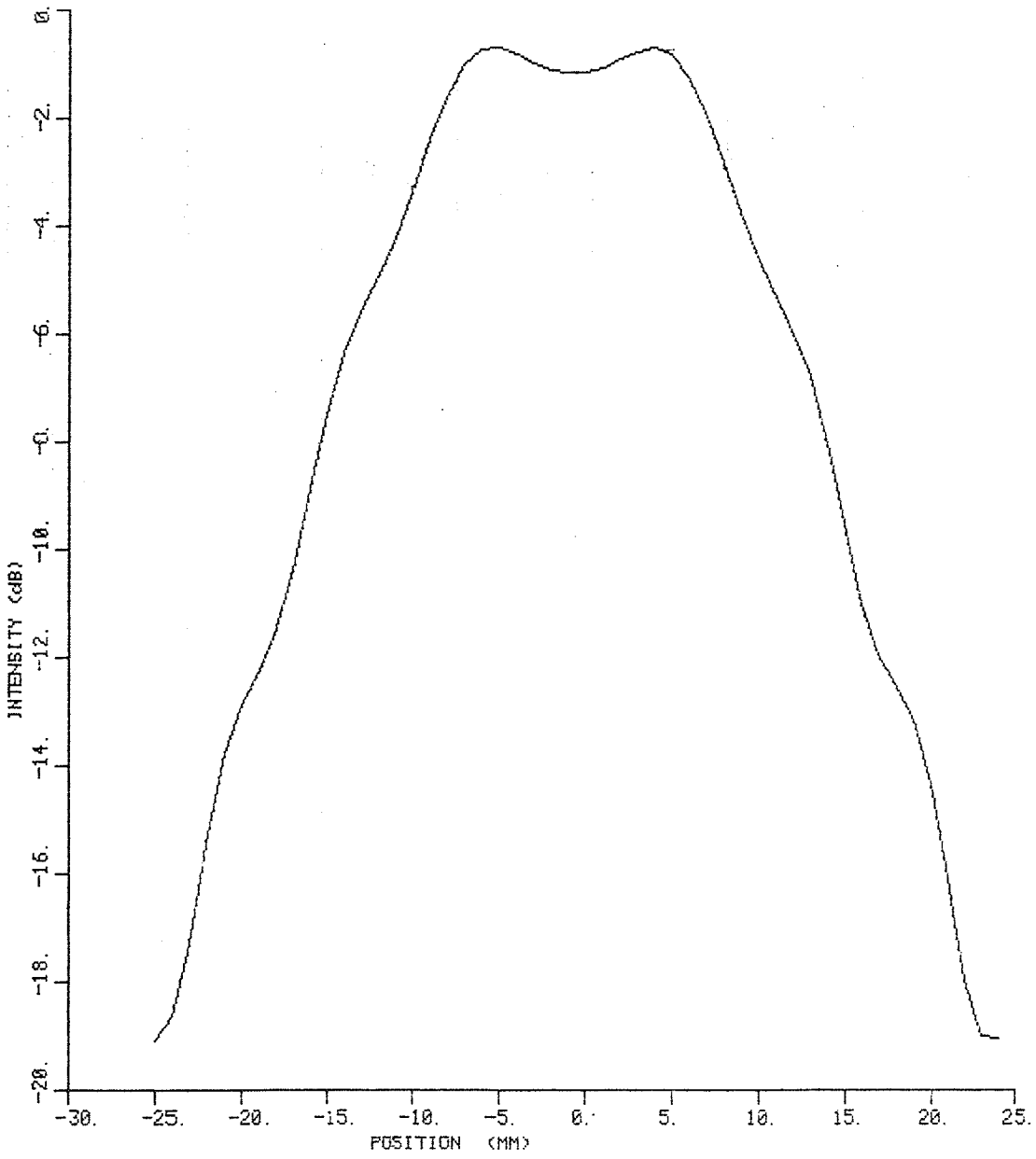

Figure C.7. Simulated transverse relative intensity at z = 7.0 cm from a single element with n = 10.

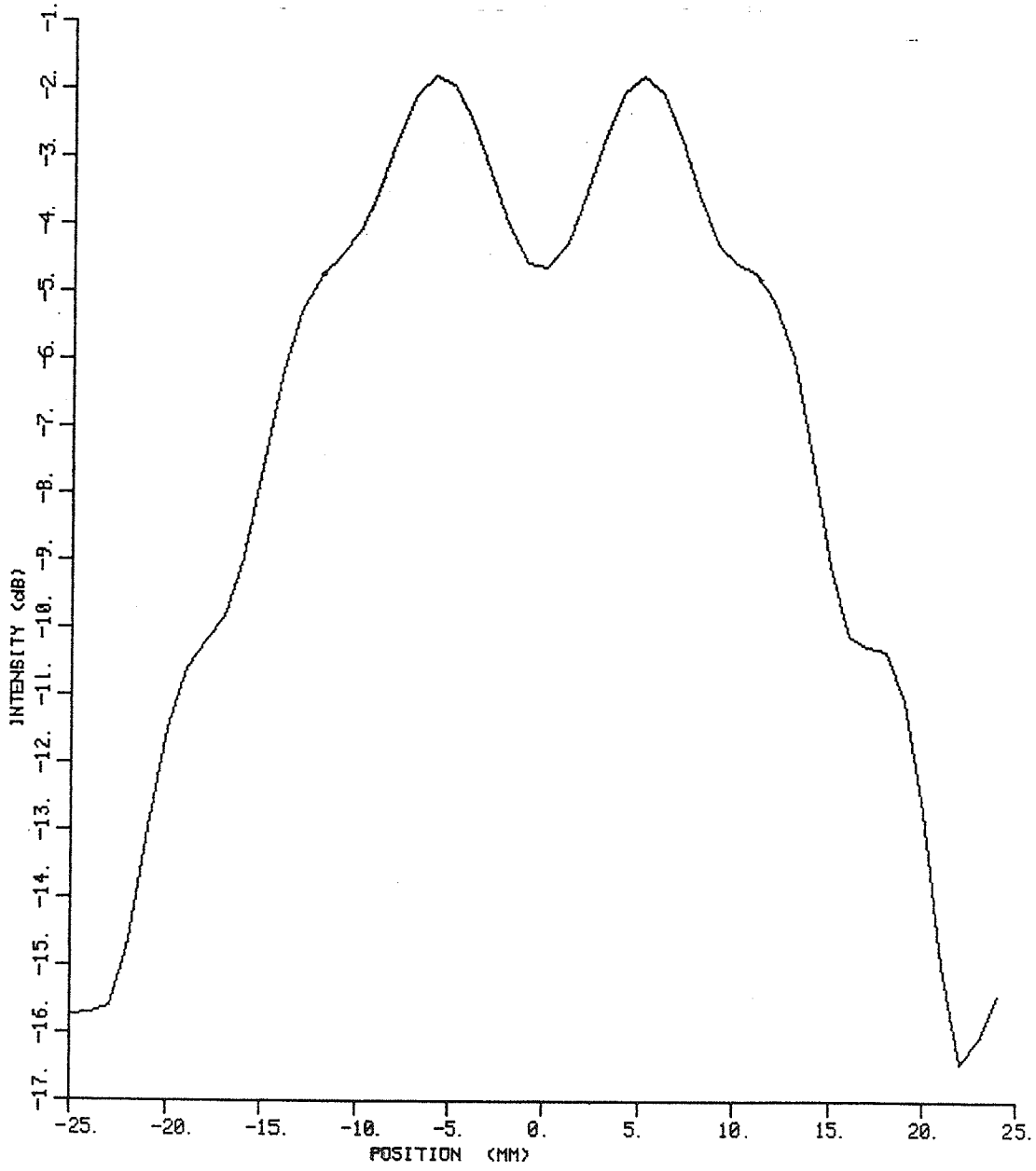

Figure C.8. Simulated transverse relative intensity at z = 13.0 cm from a single element with n = 10.

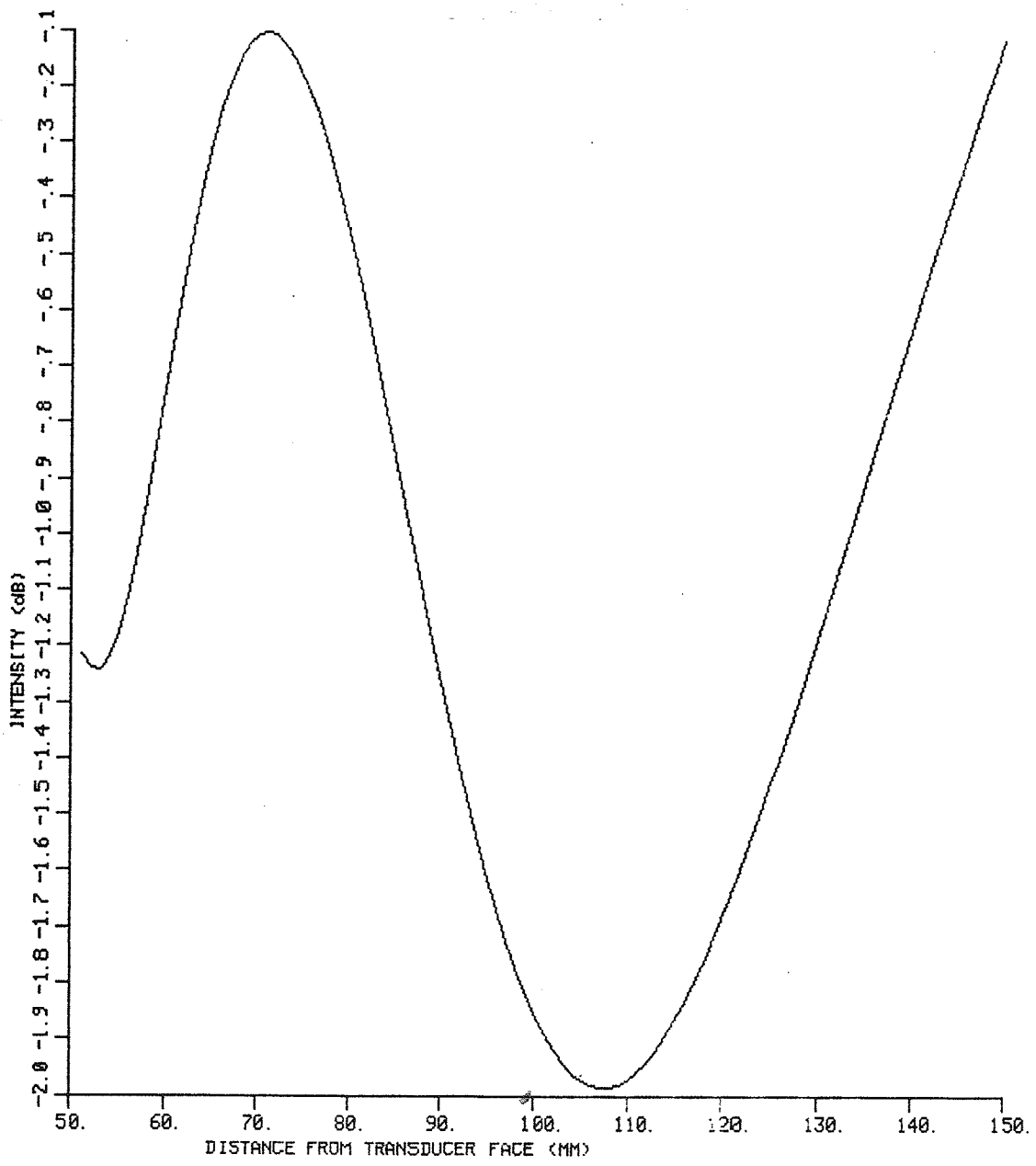

Figure C.9. Simulated axial relative intensity from a single element with n = 2.

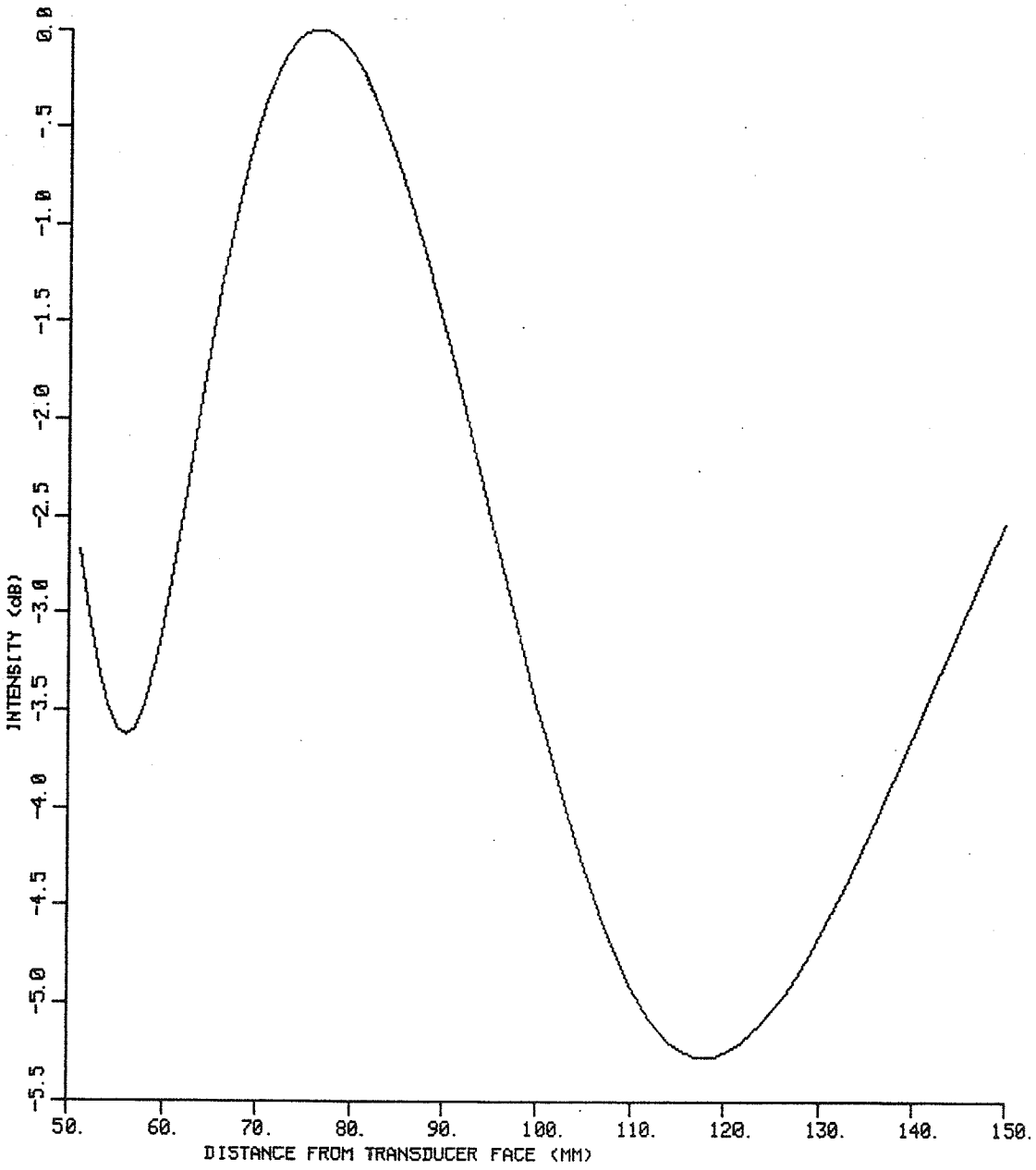

Figure C.10. Simulated axial relative intensity from a single element with n = 10.

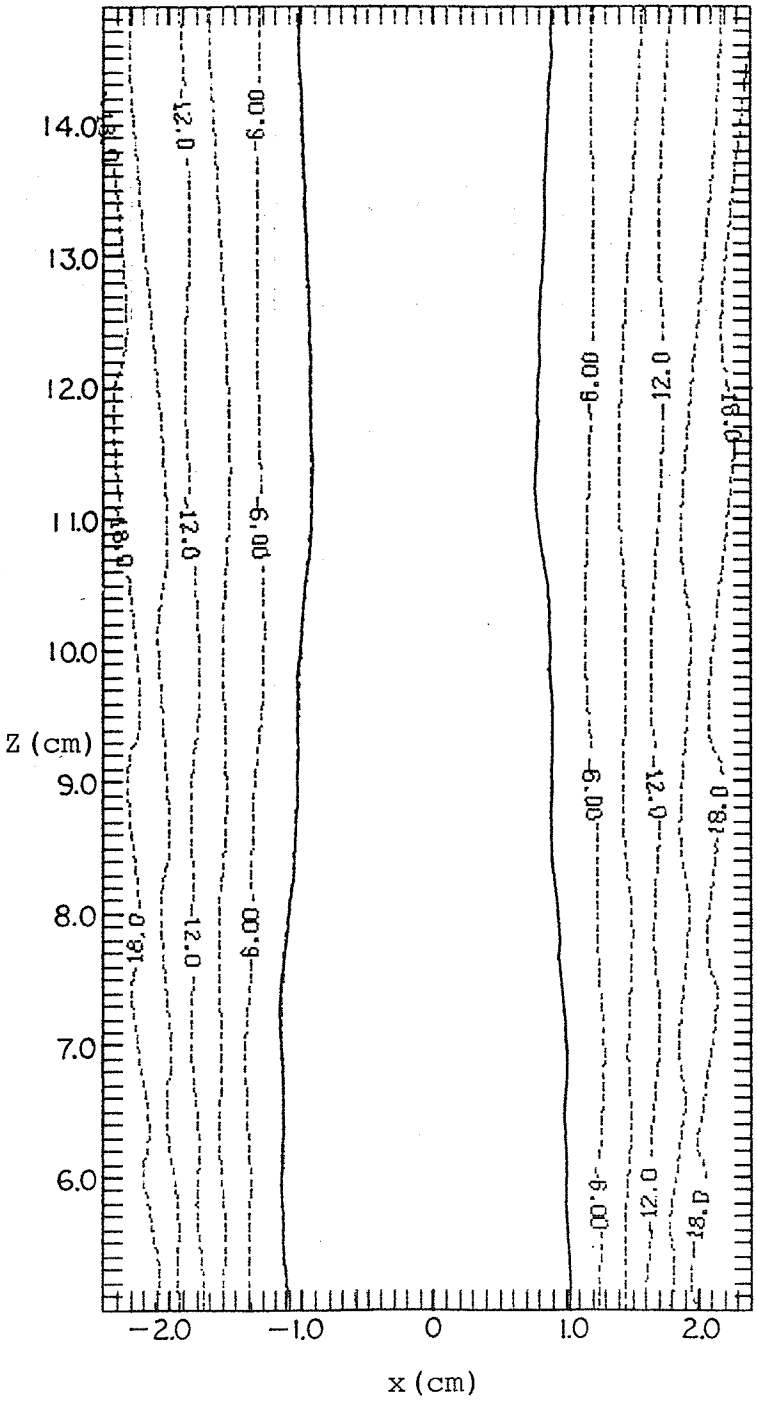

Figure C.11. Simulated 3 dB intensity contours from a single element with n = 2.

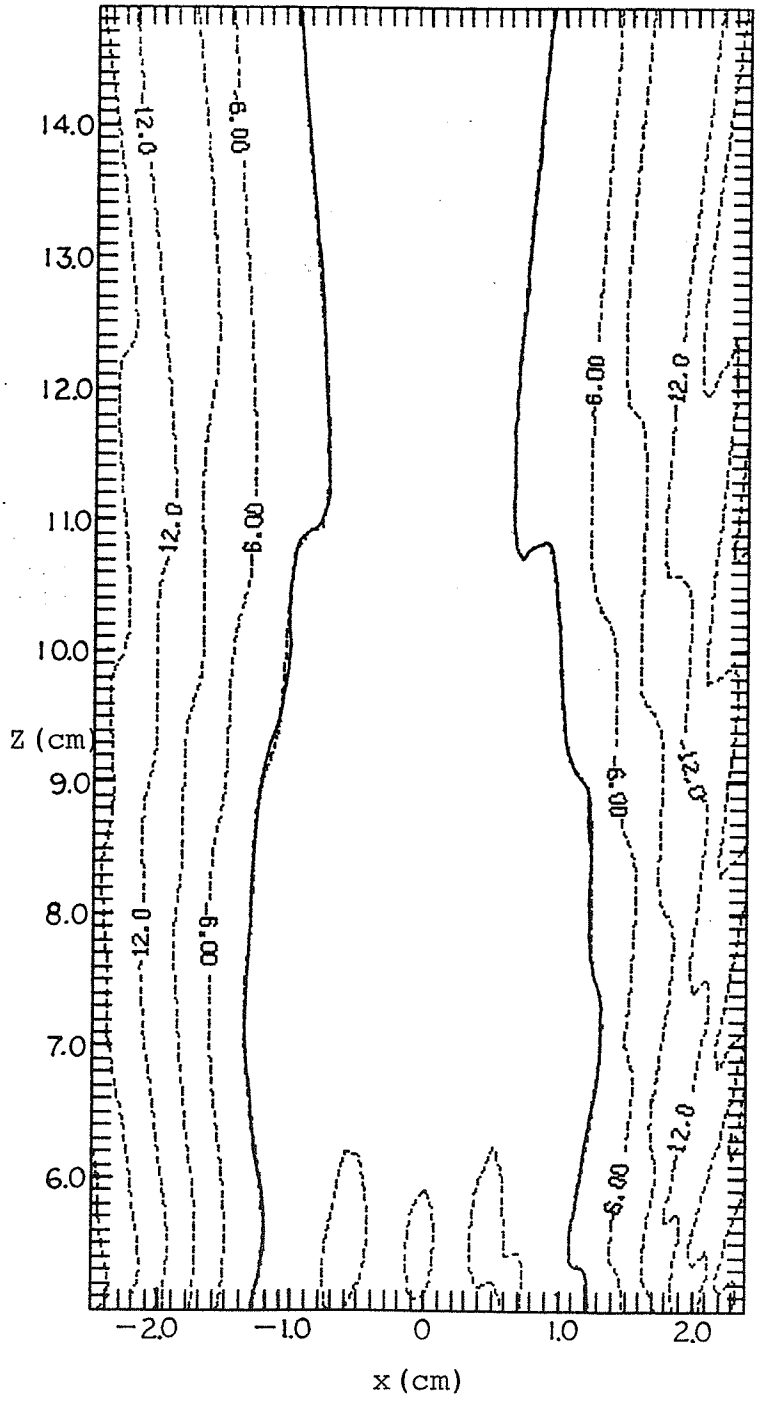

Figure C.12. Simulated 3 dB intensity contours from a single element with n = 10.

APPENDIX D

COMPUTER PROGRAMS

APPENDIX D

COMPUTER PROGRAMS

```
PROGRAM TO CALCULATE ARRAY OF POINTS FOR MAKING A CONTOUR PLOT
THIS PROGRAM IS FOR PLANAR NON-PHASED ARRAY
 WRITTEN 6/24/84 BY K. B. OCHELTREE
 LAST MODIFIED 3/19/85 BY HAROLD UNDERWOOD

DIMENSIONS ARE AC(NX,NZ),Z(NX,NZ)
    COMPLEX AC(200,200)
    DIMENSION Z(200,200),XA(16),YA(16),PH(16)

SET ARRAY PARAMETERS
FR IS FREQUENCY IN KHZ
AT IS ATTENUATION AT 1 MHZ IN NEPERS/CM
HT IS HEIGHT OF ELEMENT IN MM
WI IS WIDTH OF ELEMENT IN MM
NE IS THE NUMBER OF ACTIVE ELEMENTS
XA ARE THE X COORDINATES OF THE CENTERS OF ACTIVE ELEMENTS
YA ARE THE Y COORDINATES OF THE CENTERS OF ACTIVE ELEMENTS
PH ARE THE PHASES ON EACH OF THE ACTIVE ELEMENTS
    DATA FR,AT,HT,WI/1000.,.00022,36.12,36.12/
    DATA NE,XA(1),YA(1),PH(1)/1,0.,0.,0./

SET FIELD POINT LOCATION PARAMETERS
XS IS X STARTING LOCATION
ZS IS Z STARTING LOCATION
NX IS NUMBER OF X FIELD POINTS
NZ IS NUMBER OF Z FIELD POINTS
ST IS THE STEP SIZE BETWEEN POINTS
    DATA XS,ZS,NX,NZ,ST/-25.,1.,50,100,1./

    CALL FC(FR,AT,HT,WI,NE,XA,YA,PH,XS,ZS,NX,NZ,ST,AC)
       ZMAX=0.0
       DO 15 IX=1,NX
       DO 10 IZ=1,NZ
       Z(IX,IZ)=CABS(AC(IX,IZ))**2
       ZMAX=AMAX1(ZMAX,Z(IX,IZ))
10     CONTINUE
15     CONTINUE
    DO 20 IX=1,NX
    DO 20 IZ=1,NZ
    Z(IX,IZ)=10.*ALOG10(Z(IX,IZ)/ZMAX+1.E-20)
20  CONTINUE
     DO 30 IX=1,NX
       WRITE(8)(Z(IX,L),L=1,50)
       WRITE(8)(Z(IX,L),L=51,100)
30  CONTINUE


STORE OUTPUT IN FILE PLANE.DAT
    STOP
    END

SUBROUTINE TO CALCULATE FIELD PRODUCED BY ONE FOCAL POINT
    SUBROUTINE FC(FR,AT,HT,WI,NE,XA,YA,PH,XS,ZS,NX,NZ,ST,AC)
    DIMENSION  XA(16),YA(16),PH(16)
    COMPLEX AC(200,200),WT,EXPARG,TEMP
    DATA PI/3.1415926536/
    FAR=10.
    WAVE=1500./FR
    PIDW=PI/WAVE
    CAK=2.*PIDW
    ATT=AT*(FR/1000.)**1.1/10.
    DO 760 J=1,NZ
    DO 760 I=1,NX
```

```
760   AC(I,J)=CMPLX(0.,0.)
  CALCULATE FIELD
      DO 980 IE=1,NE
      XST=WI/2.+XS-XA(IE)
      YST=YA(IE)-HT/2.
      ZD=ZS
      SNW=XST
      DO 960 IZ=1,NZ
         WRITE(6,790)IZ
790      FORMAT('Z IS',I5)
        NH=1+INT(HT/SQRT(WAVE*ZD/FAR))
        YINC=HT/FLOAT(NH)
        CNSTY=PIDW*YINC
840     YD=YST+YINC/2.
        NW=1+INT(WI/SQRT(WAVE*ZD/FAR))
        XINC=WI/FLOAT(NW)
        CNSTX=PIDW*XINC
           XD=XST-XINC/2.
           WT=CMPLX(XINC*YINC,0.)*CMPLX(COSD(PH(IE)),SIND(PH(IE)))
           SNH=YD
           DO 920 L=1,NW
              SNX=XD
              DO 900 M=1,NH
                 DO 880 IX=1,NX
                    ARG=SQRT(XD**2+YD**2+ZD**2)
                    XARG=CNSTX*XD/ARG
                    SINCX=1.
                    IF(ABS(XARG) .GT. .0001)SINCX=SIN(XARG)/XARG
                    YARG=CNSTY*YD/ARG
                    SINCY=1.
                    IF(ABS(YARG) .GT. .0001)SINCY=SIN(YARG)/YARG
                    EXPARG=CEXP(CMPLX(-ARG*ATT,-ARG*CAK))
                    TEMP=EXPARG*WT*CMPLX(SINCX*SINCY/ARG,0.)
                    AC(IX,IZ)=AC(IX,IZ)+TEMP
                    XD=XD+ST
880              CONTINUE
                 XD=SNX
                 YD=YD+YINC
900           CONTINUE
              YD=SNH
              XD=XD-XINC
920        CONTINUE
        XD=SNW
        ZD=ZD+ST
960   CONTINUE
980   CONTINUE
      RETURN
      END
```

```
]LOAD
]LIST

5  REM  ============================================================
10  REM
15  REM   Program:  TRANSVERSE.PLOT
20  REM  Revision Date: 4/4/85
25  REM  Programmer: Tim Benson
30  REM  Revised by: Harold Underwood
110  REM    This program reads the descriptor file of a set of scanner
120  REM   data files, displays the data format, and then asks if the
130  REM   user wishes to plot the data.  If the data is to be plotted,
140  REM   the plotter is initialized, and then the data is plotted,
150  REM   the data having been stored on disk in 8K chunks in files
160  REM   with sequential filenames, e.g. filename.0, filename.1,
170  REM   filename.2, etc.
180  REM   ============================================================
190 D$ =  CHR$ (4)
200 BL$ =  CHR$ (7)
210 ET$ =  CHR$ (3)
220 CM = 0.00127
225 T1 = 0
227 LN10 =  LOG (10)
230  PRINT D$;"PR#3"
240  DIM A(9)
245  DIM G(3)
250  DIM B$(9)
260  DIM ZMAX(300)
270  FOR I = 1 TO 300:ZMAX(I) =  - 9999: NEXT I
280  HOME
290  INPUT "ENTER FILE NAME:  ";F$
300  PRINT D$;"OPEN ";F$
310  PRINT D$;"READ ";F$
320  INPUT GC$: INPUT DL: INPUT TS$
330  INPUT G(1): INPUT G(2): INPUT G(3)
430  FOR N = 1 TO 3
440  INPUT A(N)
450 A(N) = (A(N) - G(N)) * CM
460 B$(N) =  LEFT$ ( STR$ (A(N)),6)
470  NEXT N
471  FOR N = 4 TO 9
472  INPUT A(N)
473 A(N) = A(N) * CM
474 B$(N) =  LEFT$ ( STR$ (A(N)),6)
475  NEXT N
480  PRINT D$;"CLOSE ";F$
490  HOME
500  PRINT "FILE NAME          ";F$
510  IF GC$ = "Y" THEN  PRINT "COORDINATE SYSTEM: GEOMETRIC"
520  IF GC$ <  > "Y" THEN  PRINT "COORDINATE SYSTEM: TANK"
530  IF TS$ = "Y" THEN  PRINT "SCAN TYPE:         TRANSVERSE"
540  IF TS$ <  > "Y" THEN  PRINT "SCAN TYPE:         LONGITUDINAL"
550  PRINT
560  PRINT
570  PRINT "X-AXIS";: HTAB 15: PRINT "Y-AXIS";: HTAB 30: PRINT "Z-AXIS"
580  PRINT "------";: HTAB 15: PRINT "------";: HTAB 30: PRINT "------"
590  PRINT B$(1);: HTAB 15: PRINT B$(2);: HTAB 30: PRINT B$(3);: HTAB 40:
     PRINT "======) CENTER COORDINATES (CM)"
600  PRINT B$(4);: HTAB 15: PRINT B$(5);: HTAB 30: PRINT B$(6);: HTAB 40:
     PRINT "======) SCAN RANGES (CM)"
```

```
610  PRINT B$(7);: HTAB 15: PRINT B$(8);: HTAB 30: PRINT B$(9);: HTAB 40:
      PRINT "======> SCAN INCREMENTS (CM)"
620  IF TS$ <  > "Y" THEN  GOTO 810
625  REM
630  REM  Compute # of data points along x-axis.  If both the x scan
640  REM  range and x scan increment are zero, only one point was taken
650  REM   on this axis.  Otherwise, the number of points is twice the
660  REM  x scan range divided by the scan increment, plus one.
665  REM
670  IF A(4) + A(7) = 0 THEN XX = 1: GOTO 700
680 XX = (2 * A(4)) / A(7) + 1
690  REM  Compute # of data points along y-axis.  (See note for x-axis)
700  IF A(5) + A(8) = 0 THEN YY = 1: GOTO 750
710 YY = (2 * A(5)) / A(8) + 1
715  REM
720  REM  The total number of data points taken is the product of the
730  REM  number of points along the x-axis, and the number of scans
740  REM  (the number of y-axis scans)
745  REM
750 NM =  INT (XX * YY + 0.1)
760  GOTO 820
765  REM
770  REM  If this was a longitudinal scan, the number of data points
780  REM  taken is twice the z-axis range divided by the z-axis
790  REM  increment, plus one.
795  REM
800 ZZ = (2 * A(6) / A(9)) + 1
810 NM =  INT (ZZ + 0.1)
820  PRINT
830  PRINT "PROJECTED # OF X-AXIS DATA POINTS = ";XX
840  PRINT "PROJECTED # OF Y-AXIS DATA POINTS = ";YY
850  PRINT "TOTAL # OF PROJECTED DATA POINTS  = ";NM
860  PRINT "ACTUAL # OF DATA POINTS ON DISK   = ";DL / 2
870  PRINT
875  REM
880  REM  If the number of projected data points differs from the
890  REM  number of points stored on the diskette, the users is asked
900  REM  if he wants to alter the XX or YY variable.  If there is a
910  REM  discrepency, and it is not fixed, the resulting plot will
920  REM  be in error.
925  REM
930  IF DL / 2 = NM GOTO 990
940  PRINT BL$;"<<< DISCREPENCY >>>";BL$
950  INPUT "DO YOU WISH TO ALTER XX OR YY ? ";ANS$
960  IF  LEFT$ (ANS$,1) <  > "Y" THEN  GOTO 990
970  INPUT "ENTER # OF X DATA POINTS: ";XX
980  INPUT "ENTER # OF Y DATA POINTS: ";YY
990  INPUT "DO YOU WISH TO PLOT? (Y/N) ";ANS$
1000  IF  LEFT$ (ANS$,1) <  > "Y" THEN  STOP
1005  IF TS$ <  > "Y" THEN  PRINT BL$;"MUST USE LONGITUDINAL PLOT PROGRAM
     ": STOP
1010  GOSUB 13700
1020  PRINT D$;"PR#2"
1030 F1 = X3 / XX
1040 F2 = 1 - (X1 / F1)
1050  FOR Y = 0 TO 2 STEP (2 / (YY - 1))
1060 YX = X3 * Y / 13
1070 YZ = Z3 * Y / 5
1080 X = X1
1085 T1 = 1
```

```
1090  GOSUB 12700
1100  PRINT "PU", FN X(XP), FN Y(ZP),ET$
1110  FOR X = X1 TO (X2 + .01) STEP (X3 / (XX - 1))
1120  GOSUB 12700
1130  IF ZP > ZMAX((XP / F1) + F2 + .25) THEN  GOTO 1160
1140  PRINT "PU ", FN X(XP), FN Y(ZP),ET$
1150  GOTO 1180
1160 ZMAX((XP / F1) + F2) = ZP
1170  PRINT "PD", FN X(XP), FN Y(ZP),ET$
1180  NEXT X
1190  PRINT "PD", FN X(XP), FN Y(Z1 + YZ),ET$
1200  NEXT Y
1210  PRINT D$;"PR#3"
1215  PRINT "SAVE = ";"  ";SV
1220  STOP
12650  REM
12700  REM     ========================================================
12710  REM      This subroutine gets the next data point from memory.
12720  REM      ========================================================
12730  REM
12750  IF MB = 24576 THEN  GOSUB 30000
12800 A =  PEEK (MB)
12900 B =  PEEK (MB + 1)
12950  IF T1 <  > 0 THEN T1 = 0: GOTO 13010
13000 MB = MB + 2
13010 DVL = B * 16 + A
13020 DMN = 1300
13030  IF DVL < DMN THEN DVL = DMN
13035 DPK = 4096
13100 Z = 20 *  LOG (DVL / DPK) / LN10 + 10
13200 XP = X + YX
13300 ZP = Z + YZ
13400  IF  ABS (ZP) < .01 THEN ZP = 0
13450 SV = MB
13500  RETURN
13600  REM
13700  REM   ============================================================
13701  REM    This subroutine sets up the HP-7470A plotter, then
13702  REM    draws and labels the axes.
13703  REM    ============================================================
13705  REM
13710 X1 = A(1) - A(4)
13720 X2 = A(1) + A(4)
13722 Y1 = A(2) - A(5)
13724 Y2 = A(2) + A(5)
13725  INPUT "Omit Labeling? (Y/N) ";LL$
13729 Z2 = 10
13730 Z1 = 0
13731  INPUT "ENTER MAXIMUM Z-AXIS VALUE: ";ZB
13732 RN$ = "dB"
13760 FS = 0
13770 MB = 16384
13780  INPUT "ENTER # OF X TICKS ->";XT
13790 ZT = 11
13795  IF LL$ = "Y" GOTO 15600
13800  PRINT "ENTER GRAPH TITLE"
13900  INPUT T$
14000  PRINT D$;"PR#2"
14050  PRINT "IN;DF;SP 1";ET$
14100  PRINT "SC -1,1,-1,1";ET$
```

```
14200  PRINT "PU 0,.95",ET$
14300  PRINT "CP"; LEN (T$) /  - 2;",0";ET$
14400  PRINT "LB ";T$;ET$
14410  PRINT "PA,-1 ,-.2",ET$
14420  PRINT "LBRECEIVED";ET$
14430  PRINT "CP;LBINTENSITY";ET$
14440  PRINT "CP;LB(";RN$;")";ET$
14450  PRINT "PA0,-.95";ET$
14460  PRINT "CP-10,0";ET$
14470  PRINT "LBX-AXIS POSITION (cm)";ET$
14480  PRINT "PA.75,-.5";ET$
14490  PRINT "LBY-AXIS";ET$
14500  PRINT "CP;LBPOSITION";ET$
14510  PRINT "CP;LB(cm)";ET$
15600 X3 = X2 - X1
15700 Z3 = Z2 - Z1
15710 XS = 10 ^ (3 -  INT ( LOG (X2 - X1)))
15720 YS = 10 ^ (3 -  INT ( LOG (Z2 - Z1)))
15800 S1 = (X1 - (1 / 3) * X3) * XS
15900 S2 = (X2 + (1 / 3) * X3) * XS
16000 S3 = (Z1 - (1 / 4) * Z3) * YS
16100 S4 = (Z2 + (1 / 2) * Z3) * YS
16110  DEF  FN X(X9) = X9 * XS
16120  DEF  FN Y(Y9) = Y9 * YS
16200  PRINT D$;"PR#2"
16300  PRINT "SP 1",ET$
16400  PRINT "SC ",S1,S2,S3,S4,ET$
16450  PRINT "PU", FN X(X1), FN Y(Z2),ET$
16500  PRINT "PD", FN X(X1), FN Y(Z1),ET$
16600  PRINT "PD", FN X(X2), FN Y(Z1),ET$
16700 X4 = (2 / 13) * X3
16800 Z4 = (2 / 5) * Z3
16900  PRINT "PD", FN X(X2 + X4), FN Y(Z1 + Z4),ET$
17000  PRINT "PU", FN X(X1), FN Y(Z1),ET$
17005  PRINT "PD", FN X(X1 + X4), FN Y(Z1 + Z4),ET$
17006  IF LL$ = "Y" GOTO 18900
17010  REM
17020  REM
17030  REM  Label the x-axis
17040  REM
17050  REM
17100  FOR X = X1 TO X2 + .01 STEP X3 / (XT - 1)
17200  IF  ABS (X) < .01 THEN X = 0
17300  PRINT "PU", FN X(X), FN Y(Z1),ET$
17400  PRINT "XT",ET$
17500 X$ =  LEFT$ ( STR$ (X),4)
17600  IF  ABS (X) < .01 THEN X$ = "0"
17700 LE =  LEN (X$) /  - 2
17800  PRINT "CP",LE;",-1.5;LB";X$;ET$
17810  NEXT X
17820  REM
17821  REM
17822  REM    Label the y-axis
17823  REM
17824  REM
17830  PRINT "PU", FN X(X2), FN Y(Z1),ET$
17840  PRINT "YT",ET$
17845 Y$ =  LEFT$ ( STR$ (Y1),4)
17847  IF  ABS (Y1) < .01 THEN Y$ = "0"
17850  PRINT "CP 1.75,-.25;LB";Y$;ET$
```

```
17855  PRINT "PU", FN X(X2 + X4), FN Y(Z1 + Z4),ET$
17860  PRINT "YT",ET$
17865 Y$ =  LEFT$ ( STR$ (Y2),4)
17870  IF  ABS (Y2) < .01 THEN Y$ = "0"
17875  PRINT "CP 1,-.25;LB";Y$;ET$
17910  REM
17920  REM
17930  REM  Label the z-axis
17940  REM
17950  REM
18000  FOR Z =  - 10 TO 0 STEP Z3 / (ZT - 1)
18100  IF  ABS (Z) < .01 THEN Z = 0
18300  PRINT "PU", FN X(X1), FN Y(Z + 10),ET$
18400  PRINT "YT",ET$
18500 Z$ =  LEFT$ ( STR$ (Z),4)
18600  IF  ABS (Z) < .01 THEN Z$ = "0"
18700  PRINT "CP -4.5,-.25;LB";Z$;ET$
18800  NEXT Z
18900  PRINT D$;"PR#3"
18950  GOSUB 30000
19000  RETURN
30000  REM    ========================================================
30001  REM  This subroutine is called to load (BLOAD) the next 8K
30002  REM  file of scanner data into memory.
30003  REM  ========================================================
30200 D$ =  CHR$ (4)
30300  PRINT D$;"PR#3"
30310  VTAB 1: HTAB 1: PRINT " "
30320  VTAB 23: HTAB 30
30330  INVERSE
30400  PRINT "  LOADING DATA FILE ";F$;".";FS;"  ";
30450  NORMAL
30499 D$ =  CHR$ (13) + CHR$ (4)
30500  PRINT D$;"BLOAD ";F$;".";FS;",A$4000"
30510  VTAB 23: HTAB 30: PRINT "
30750 FS = FS + 1
30760 MB = 16384
30770  PRINT D$;"PR#2"
30800  RETURN
]
```

REFERENCES

Benson, T. P., "The Design of a Microwave Phased Array Hyperthermia System," M.S. Thesis, University of Illinois. Urbana-Champaign, Urbana, IL, 1985.

Freedman, A., "Sound Field of a Rectangular Piston," J. Acoust. Soc. Am. 32, 197-209, 1960.

Hahn, G. M. Hyperthermia and Cancer, (Plenum Press, New York. 1982).

Hahn, G. M., "Hyperthermia for the Engineer: A Short Biological Primer," IEEE Trans. Biomed. Eng., vol. 31, no. 1, pp. 3-8, 1984.

Kinsler, L. E., A. R. Frey, A. B. Coppens, J. V. Sanders, Fundamentals of Acoustics, (John Wiley and Sons, New York, 1982).

Lyons, B. E., R. H. Britt, J. W. Strobehn, "Localized Hyperthermia in the Treatment of Malignant Tumors Using an Interstitial Microwave Antenna Array," IEEE Trans. Biomed. Eng., vol. 31, no. 1, pp. 55-62.

Nyborg, W. E., Intermediate Biophysical Mechanics, (Cummings Publishing Company, Menlo Park, CA, 1975).

Ocheltree, K. B., "Theoretical Analysis of Ultrasonic Linear Phased Arrays for Hyperthermic Treatment," M.S. Thesis, University of Illinois. Urbana-Champaign, 1984.

Oleson, J. R., "A Review of Magnetic Induction Methods for Hyperthermia Treatment of Cancer," IEEE Trans. Biomed. Eng., vol. 31, no. 1, pp. 91-97. 1984.

Overgaard J.. "Influence of Extracellular pH on the Viability and Morphology of Tumor Cells Exposed to Hyperthermia," JNCI, vol 56, pp. 1243-1250, 1976.

Padgitt, D. G., "An Ultrasonic Transducer Field Scanner System," M. S. Thesis, University of Illinois, Urbana-Champaign. Urbana, IL, 1983.

Paglione, R.. "27 MHz Ridged Waveguide Applicators for Localized Hyperthermia Treatment of Deep-seated Malignant Tumors," Microwave Journal, vol. 24., no. 2. pp. 71-80, 1981.

Pounds, D. W., R. H. Britt, "Single Ultrasonic Crystal Techniques for Generating Uniform Temperature Distributions in Homogeneously Perfused Tissues," IEEE Trans. Sonics and Ultrasonics, vol. SV-31, no. 5, pp. 482-490, 1984.

Song, C. W., A. Lokshina, J. G. Rhee, M. Pattern, S. H. Levitt, "Implication of Blood Flow in Hyperthermic Treatment of Tumors," IEEE Trans. Biomed. Eng., vol.31, no. 1, pp. 9-16, 1984.

Stauffer, P. R., T. C. Cetas, A. M. Fletcher, D. W. DeYoung, M. W. DeWhirst, J. R. Oleson, R. B. Roemer, "Observations on the Use of Ferromagnetic Implants for Inducing Hyperthermia," IEEE Trans. Biomed. Eng.- vol. 31, no. 1, pp. 76-90, 1984.